CHARGE TRANSPORT THROUGH SINGLE MOLECULES IN TWO- AND THREE-TERMINAL MECHANICAL BREAK JUNCTIONS

CHARGE TRANSPORT THROUGH SINGLE MOLECULES IN TWO- AND THREE-TERMINAL MECHANICAL BREAK JUNCTIONS

Proefschrift

ter verkrijging van de graad van doctor aan de Technische Universiteit Delft, op gezag van de Rector Magnificus Prof. ir. K. C. A. M. Luyben, voorzitter van het College voor Promoties, in het openbaar te verdedigen op maandag 11 januari 2010 om 15:00 uur

door

Christian Alexander MARTIN

Diplom-Ingenieur Elektrotechnik, Technische Universität Hamburg-Harburg, Duitsland, geboren te Hamburg, Duitsland.

Dit proefschrift is goedgekeurd door de promotoren:

Prof. dr. ir. H. S. J. van der Zant en

Prof. dr. J. M. van Ruitenbeek

Samenstelling van de promotiecommissie:

Rector Magnificus voorzitter

Prof. dr. ir. H. S. J. van der Zant Technische Universiteit Delft, promotor

Prof. dr. J. M. van Ruitenbeek
Prof. dr. ir. T. M. Klapwijk
Prof. dr. E. J. H. Sudhölter
Prof. dr. D. M. de Leeuw
Universiteit Leiden, promotor
Technische Universiteit Delft
Technische Universiteit Delft
Rijksuniversiteit Groningen

Prof. dr. L. Venkataraman Columbia University, New York, USA

Dr. F. Evers Universität Karlsruhe, Duitsland

Prof. dr. ir. G. E. W. Bauer Technische Universiteit Delft (reservelid)









Keywords: molecular electronics, single-molecule junction, nanoscale transport

Printed by: Gildeprint Drukkerijen, Enschede, The Netherlands

Cover design: C. A. Martin

Copyright © 2010 by C. A. Martin

Casimir PhD Series, Delft-Leiden, 2010-01

ISBN 978-90-8593-066-2

An electronic version of this dissertation is available at

http://repository.tudelft.nl/.

The scientific enterprise as a whole does from time to time prove useful, open up new territory, display order, and test long-accepted belief. Nevertheless, the individual engaged on a normal research problem is almost never doing any of these things.

Thomas S. Kuhn, 'The Structure of Scientific Revolutions'

CONTENTS

I	Intr	troduction						
	1.1	Molecular electronics - a perspective						
	1.2	Attaching molecules to metal electrodes						
	1.3	Fabrication of nanometer-sized metal electrodes						
		1.3.1 Two-terminal measurements						
		1.3.2 Three-terminal measurements						
		1.3.3 Deposition methods for molecular electronics						
	1.4	Thesis outline						
	Refe	erences						
2	The	eoretical background						
		Electron transport in metallic conductors						
		2.1.1 The importance of length scales						
		2.1.2 Diffusive transport in macroscopic wires						
		2.1.3 Nanoscale contacts in the semi-classical approximation 2						
		2.1.4 Quantum ballistic transport						
		2.1.5 Scattering approach for point contacts						
		2.1.6 Vacuum tunneling						
	2.2	Transport across single molecules						
		2.2.1 Energy scales of single-molecule junctions						
		2.2.2 The role of the coupling to the leads						
		2.2.3 Coherent tunneling						
		2.2.4 Coulomb blockade and sequential tunneling						
		2.2.5 Spectroscopic features in molecular junctions						
	Refe	erences						
3	Des	sign and characterization of the MCBJ measurement system 4						
	3.1	Mechanically controllable break junctions						
		3.1.1 Mechanics of two-terminal MCBJs 4						
		3.1.2 Device design						
		3.1.3 Fabrication of lithographic MCBJs						
	3.2	The experimental setup - a cryogenic three-point bending apparatus 4						
		3.2.1 Design of the vacuum insert						
		3.2.2 Actuation mechanism						
		3.2.3 Measurement electronics and wiring 5.						
	3.3	Measurement techniques						
		3.3.1 Conductance traces						

viii Contents

		3.3.2 Conductance histograms	56
		3.3.3 Trace histograms	58
		3.3.4 Statistical <i>IV</i> measurements	60
		3.3.5 Three-terminal measurements	60
	3.4	Mechanical characterization	61
		3.4.1 Stability of the setup	61
		3.4.2 Backlash of the actuator	61
		3.4.3 Calibration of the displacement ratio of the MCBJs	63
	Refe	erences	64
4	Lith	hographic MCBJs for single-molecule measurements in vacuum	67
	4.1	Introduction	68
	4.2	Experimental details	69
	4.3	Optimization of measurement parameters	69
	4.4	Conductance histograms of model systems	71
	4.5	IV measurements on benzene derivatives	74
	4.6		78
		erences	78
5	Full	lerene-based anchoring groups for molecular electronics	83
•	5.1	Introduction	84
	5.2	Molecular design and synthesis (J. K. Sørensen and T. Bjørnholm, University	
		of Copenhagen)	84
	5.3	Experimental details	85
	5.4	Histogram measurements	87
	5.5	Conclusions	89
	Refe	erences	89
6	Gat	ted MCBJs with suspended source-drain electrodes	91
	6.1	Introduction	92
	6.2	Experimental details	92
	6.3	Gate-induced switching of quantum point contacts	93
	6.4	Modeling	97
	6.5		100
	Refe		101
7	Cha	arge transport in junctions of \mathbf{C}_{60}	103
			104
	7.2		105
	7.3	•	105
	7.4		106
	7.5		108
	7.6	<u> </u>	110
			110

CONTENTS ix

8		nsport in mechanically stable gated MCBJs	113		
	8.1	Introduction	114		
	8.2	Experimental details	115		
	8.3	Mechanical and electrical characterization of the devices	116		
		Bending-controlled Coulomb blockade			
	8.5	Conclusions	123		
	Refe	erences	124		
Re	ecipe	s	127		
Su	ımm	ary	131		
Sa	men	vatting	135		
Cı	ırric	ulum Vitae	139		
Li	List of Publications				
Ac	Acknowledgements				

1

Introduction

Computing machines are very large; they fill rooms. Why can't we make them very small, make them of little wires, little elements - and by little, I mean little. For instance, the wires should be 10 or 100 atoms in diameter, and the circuits should be a few thousand angstroms across.

Richard P. Feynman, 1959

1.1 MOLECULAR ELECTRONICS - A PERSPECTIVE

Had he continued his train of thought, Richard Feynman could have motivated molecular electronic devices right then and right there, during his famous lecture 'There's Plenty of Room at the Bottom' [1] at the 1959 meeting of the American Physical Society. At the time, though, even the route towards micrometer-sized circuits was less than clear. It was only 25 years later that Ari Aviram and Mark Ratner developed a vision for the ultimate miniaturization of electronic devices and proposed the first single-molecule diode (see Figure 1.1) [2].

Their idea was largely motivated by the ground-breaking progress in solid-state electronics that had followed Feynman's speech. At the time of Aviram's and Ratner's proposal, the invention of the integrated circuit by Jack Kilby [3] had paved the way for miniaturized semiconductor devices and the fabrication of a small and fast electronic computing machine - the microprocessor. Eventually, its development initiated the age of information technology and enabled the way we work and live today.

The success of information technology would not have been possible without the steady miniaturization of electronic devices, which has increased both their speed and their integration density. Since 1965, when feature sizes were still well beyond 10 μ m, the down-

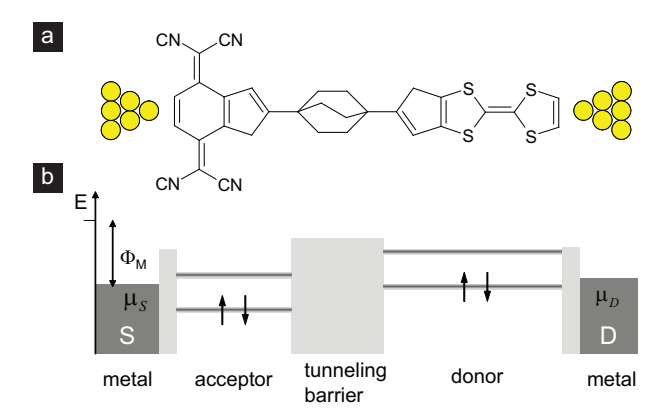


FIGURE 1.1: Illustration of the original single-molecule rectifier that was proposed by Aviram and Ratner [2]. (a) Schematic of the molecule between two metal electrodes and (b) the corresponding energy diagram.

scaling of integrated circuits has been guided by Moore's law [4]. In its current adapted form, Moore's law predicts a doubling of the transistor density in microprocessors in every 18 months and field effect transistors with channel lengths of about 11 nm in 2022.

It will be hard to attain these small sizes using current semiconductor fabrication technology [5]. Fundamental limitations in the control of doping processes and the breakdown voltages of dielectric insulators require alternative approaches to the miniaturization of integrated circuits [6]. Recently, molecular electronics have been put forward as a possible solution to some of these technological challenges.

In the example of Aviram's and Ratner's single-molecule diode two π -conjugated subunits separated by an aliphatic spacer mimic a p-n-junction in an inorganic semiconductor on a length of less than 4 nm. Similar to silicon technology, Aviram and Ratner suggested a 'doping' of the π -conjugated subunits by chemical substituents of different electron affinities. However, it took several years before experimentalists could probe the electrical characteristics of an object as small as a single molecule to put their idea to the test.

Since the first electrical measurements on benzenedithiol molecules in 1997 [7], research in molecular electronics has progressed rapidly. Today, numerous techniques based on nanolithography and scanning probe instruments allow for studies of the electrical properties of single molecules [8–15]. In one family of molecules, the amines, the tuning of the molecular conductance by the geometry of the π -conjugated system [16, 17] and by chemical substituents [18] has been demonstrated.

Nevertheless, the field of molecular electronics is far from maturity. The influence of the junction geometry on the electrical characteristics of single molecules remains a fascinating and crucial area of research. Early experiments have shown that the electrical characteristics of junctions of symmetric molecules are not necessarily symmetric in bias voltage [19]. Furthermore, the same molecule can exhibit various conductance values [20], and its interface with the electrodes, which is usually determined by chemical anchoring groups, can have a large influence on its electrical properties [21]. Moreover, transistor-

type devices from the same molecule have displayed fundamentally different transport characteristics [22, 23]. As silicon-based technology is approaching transistor channel lengths of 30 nm and oxide thicknesses of a few atomic layers [24], it is hence uncertain if single molecules will soon find their way into integrated circuits.

To resolve many of the open questions in molecular electronics, two experimental challenges need to be tackled. First, a well-defined and stable bond between the molecule and the metal electrodes needs to be established. Only if this requirement is met can the electronic properties of single-molecule devices be controlled. Secondly, the need for a versatile device architecture is paramount. Only the simultaneous control over the electrode spacing and the potential of the molecule will enable a full characterization of molecular junctions.

This Thesis pursues these goals in a number of experiments based on lithographically fabricated mechanically controllable break junctions (MCBJs). In these devices, the spacing between two nanometer-sized electrodes can be varied with subangstrom precision to form single-molecule junctions. In the first part of the Thesis, the suitability of different chemical end groups for stable anchoring at room temperature and in vacuum is investigated. The second part covers the integration of two-terminal MCBJs with a gate electrode. Two approaches to electrically and mechanically tunable devices are presented, which enable thorough studies of molecular junctions.

Even if molecular electronics research may not deliver single-molecule devices in the near future, it will still have an important impact on neighboring areas of research. Today, the study of single-molecule conductance already offers microscopic insights into the solvation shell in electrochemical environments [25]. Furthermore, monolayers of functional molecules have been exploited to fabricate tunneling diodes [26] and field-effect transistors [27]. In the field of molecular electronics itself, the vivid interplay between experiment and theory has led to a continuing refinement of quantum chemical calculations [28]. Eventually, only fundamental understanding and precise control will allow us to fully benefit from the unique properties of single molecules. This may not necessarily be their small size; the sensitivity of molecular devices to chemical stimuli may also offer new prospects - very much in line with Ari Aviram and Mark Ratner, whose proposal was inspired by electronic processes in biological systems.

1.2 ATTACHING MOLECULES TO METAL ELECTRODES

The formation of a stable and well-defined metal-molecule bond is one of the prerequisites for systematic studies of molecular transport. This bond is typically established by chemical anchoring groups (see Figure 1.2) that bind to the electrode surface.

For this Thesis, single-molecule junctions have been formed using lithographic MCBJs with gold electrodes. Due to its chemical inertness, gold is the most common electrode material in molecular electronics to date. In this section we review two important molecular families for the chemical functionalization of gold electrodes, thiols and amines. Moreover, we discuss the adsorption and self-assembly of C_{60} on gold surfaces, one of the prototypical species in molecular electronics.

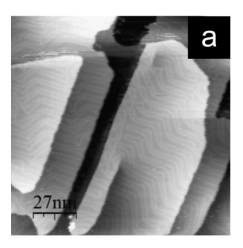
FIGURE 1.2: Schematic of a single-molecule junction and some chemical end groups that have been used to anchor molecules to gold electrodes. Besides the well-established thiols and amines (see text), selenols [29], pyridines [12], carboxylic acids [30], isocyanides [31], phosphines [32], methylsulfides [32], and thiocyanates [33] have been studied in single-molecule junctions.

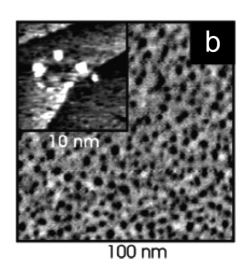
Thiols and amines - two examples of chemisorption

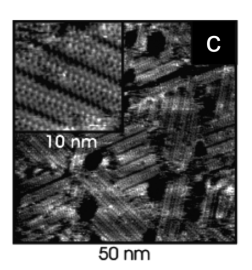
Since the early stages of molecular electronics, single molecules have been attached to gold electrodes using thiol (SH) anchoring groups [34]. While the details of the adsorption mechanism are still under debate, it is widely believed that the hydrogen of the thiol group is eliminated in contact with gold and a covalent Au-S bond is formed [35, 36]. This bond possesses a dissociation energy around 2.1 eV [35], which is large enough to ensure the thermal stability of thiol monolayers up to 100° C [37]. Furthermore, it is stronger than the Au-Au bond (with a dissociation energy around 0.8 eV [38]), which can lead to the removal of single gold atoms by desorbing thiols [35]. The versatility of the thiol anchoring guarantees a dense coverage of both flat and rough gold surfaces [39, 40]. On the Au(111) surface (see Figure 1.3a) thiols can bind to three sites, the so-called top, bridge, and hollow site. In these configurations, the sulfur atom of the thiol is bound to one, two, and three gold atoms, respectively. Rough nanometer-sized gold electrodes may even allow for more degrees of freedom [35].

Most molecular electronics experiments on thiols have employed solution deposition. Alkanedithiols - one of the model systems in molecular electronics [44] - are typically applied from millimolar solutions in ethanol. In the case of π -conjugated molecules that can stack due to molecule-molecule interactions, apolar solvents such as toluene may be beneficial [34]. It is important to note that many of the fundamental studies of self-assembly have focused on alkanethiols [35]. The structure of monolayers from alkanedithiols and dithiolated conjugated molecules may differ from established results [34, 45, 46]. Here, we nonetheless review some of the most important characteristics of alkanethiols.

As soon as a gold surface is brought into contact with a solution of alkanethiols, a sub-monolayer of the molecules is formed. At concentrations around 1 mmol/l the deter-







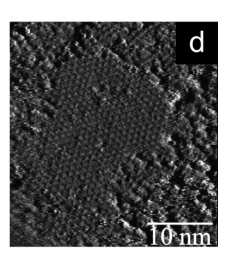


FIGURE 1.3: STM images illustrating the self-assembly of molecular monolayers on gold. (a) Clean Au(111) surface [41]. (b) Disordered high-coverage and (c) Striped low-coverage monolayer of nonanedithiol. (Reproduced with permission from Reference [42]. ©2008 by the American Chemical Society). (d) Disordered and locally crystalline monolayer of C_{60} fullerenes (Reproduced with permission from Reference [43]. ©2002 by The Royal Society of Chemistry).

mining timescale of chemisorption is the reaction rate constant, and a disordered submonolayer forms within minutes [40]. In this early phase of self-assembly, both striped domains with flat-lying molecules and domains of upright molecules may coexist (see parts b and c of Figure 1.3). As the self-assembly continues, the coverage increases and defects such as domain boundaries and vacancies are annealed. Furthermore, the interactions between the molecular backbones lead to a predominantly vertical alignment of the alkanethiols in dense monolayers.

The high reactivity of the thiol group not only guarantees a robust functionalization of gold electrodes; it can also lead to complications during the self-assembly process. The cross-linking of dithiols in the presence of trace amounts of oxygen may cause multilayer formation [34, 45] and, in electrical measurements, the probing of oligomers. This oxidation can be prevented by working in an inert atmosphere. Furthermore, the in-situ activation of thioacetates with a basic deprotection agent can reduce the risk of multilayer formation significantly [34].

The use of amines for single-molecule measurements in solution has been pioneered very recently [31]. Amines have only scarcely been used in the functionalization of metal surfaces, and their bond to gold is weaker than that of thiols [47–49]. Simulations indicate that the ability to extract single gold atoms from gold surfaces is not present in amines [50]. Furthermore, it has been suggested that the amine-gold bond is of a donor-acceptor type, with the lone pair of the nitrogen atom preferentially binding to surface adatoms. The calculated dissociation energy of the bond is around 1 eV [51].

In contrast to thiol chemistry, the self-assembly of amines is highly dependent on the solution environment. Polar solvents such as ethanol and polar contaminants can stabilize the amino group and hinder the self-assembly on gold [52]. Furthermore, amine monolayers do not form at elevated temperatures [53]. Nevertheless, single-molecule junctions of amines can be formed routinely in solution and at room temperature, most likely due to an enhanced reactivity of amines on rough surfaces [48, 54].

Adsorption of fullerenes

Molecular electronics experiments have also been carried out on species that do not undergo a chemical reaction with the electrodes. The best-studied example is given by the fullerene C_{60} [55], which can bind to metal surfaces through a fractional charge transfer from the substrate [56, 57]. On Au(111) the excess charge on the fullerene amounts to about 0.1 electrons, which leads to a strong bond with an energy of about 2.4 eV [58]. Stable adlayers of fullerenes have been formed in various solvents [43, 59, 60] (see Figure 1.3d for an example).

1.3 FABRICATION OF NANOMETER-SIZED METAL ELECTRODES

The formation of a single-molecule junction requires the fabrication of electrodes with gaps on the order of a nanometer. In the mid-1980s, the invention of the scanning probe microscope [61] made the length scale of atoms accessible and enabled the first electrical measurements on single molecules [62]. Furthermore, electron-beam lithography allowed researchers to fabricate nanometer-sized structures [63] that could be used as contacts in planar single-molecule devices.

These two instruments still form the basis of many of today's experiments in molecular electronics. In this section, the most important techniques for contacting single molecules are presented. It starts with a review of two-terminal architectures. The discussion then continues with gated devices, which allow for an independent control of the potential of the molecule. The section is concluded with an overview of different molecule deposition methods that complete the formation of single-molecule junctions.

1.3.1 TWO-TERMINAL MEASUREMENTS

Two-terminal measurements of the low-bias conductance and the current-voltage characteristics of single molecules are mostly carried out in scanning tunneling microscopes or mechanically controllable break junctions.

The scanning tunneling microscope (STM) was used in the first studies of molecular electronics [64-67] and is still widely applied today. While it enables both the imaging and the electrical characterization of single molecules on metal surfaces, its working principle leads to limitations in the possible junction configurations. The STM is based on a tunneling contact between an atomically sharp probe and a conductive sample (see Figure 1.4b). Therefore, the junction formed by the metal substrate, the molecule, and the STM tip is highly asymmetric. The image data in an STM is provided by a feedback loop that maintains a constant tunneling current during the scanning of the sample surface. The apparent height of a molecule in an STM image hence includes contributions from both its height and its electronic structure, and it cannot be readily related to a two-terminal conductance [68]. To acquire the current-voltage characteristics of a single molecule, the feedback loop of the STM needs to be interrupted before the bias voltage is ramped [62]. The resulting data is susceptible to drift and, again, only representative of asymmetric junctions. Recently, the study of more symmetric molecular junctions was enabled by introducing a thin insulating layer between the molecules and the conductive substrates [69]. Despite this improvement, the use of scanning-mode STMs remains restricted to junc-

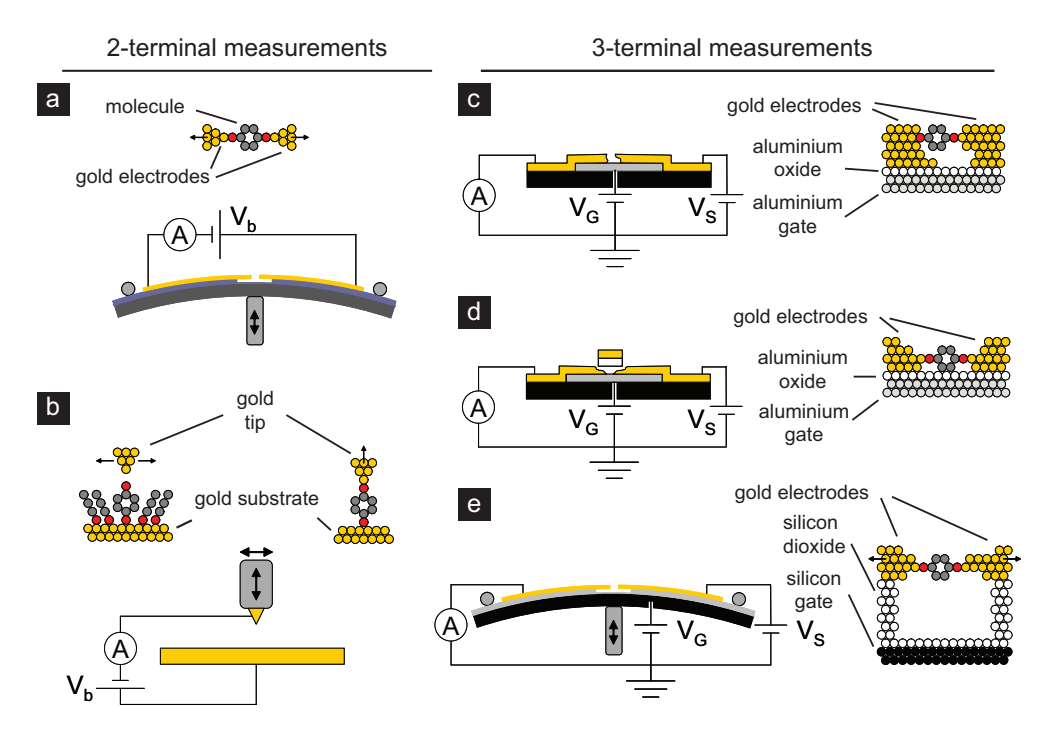


FIGURE 1.4: Schematics of the most common experimental architectures for molecular electronics. Twoterminal transport is typically studied in (a) mechanically controllable break junctions and (b) scanning probe microscopes. Three-terminal measurements are carried out using (c) wires broken by electromigration, (d) shadow-evaporated nanoscale gaps, and (e) gated mechanical break junctions.

tions with at least one tunneling contact. Prototypical single-molecule devices, however, require stable and well-defined anchoring to both electrodes. Such a configuration can be achieved in modified STMs that use the break junction method. In this approach, which has been pioneered by Xu and Tao [12], a metallic contact between the tip and the substrate is repeatedly broken and established in the presence of the molecules of interest. The break junction principle builds on the assumption that molecules binding to the metal surfaces will, with some finite probability, form a conducting bridge between both electrodes after cleaving the last metal-to-metal contact. During the breaking of the contact the current is monitored at a fixed bias voltage. Stable conductance values during the stretching of the junctions may then be attributed to single-molecule contacts. To date, most STM break junction measurements have been carried out in solution. Although this appears to be a very suitable environment for studying single-molecule properties, it also imposes an important limit on the experiments: the temperature range is restricted to a few tens of degrees. Furthermore, the stability of modified STMs is limited and renders the acquisition of current-voltage characteristics difficult.

Mechanically controllable break junctions (MCBJs) do not suffer from these restrictions. They can easily be operated down to cryogenic temperatures in a vacuum environment

and their electrode gap is exceptionally stable. This stability is mainly due to the working principle of MCBJs, in which the bending of a flexible substrate is translated into the stretching of two suspended metal electrodes on the device surface [70] (see Figure 1.4a). The ratio of these displacements can be as low as 10^{-5} for lithographically fabricated devices, giving rise to subangstrom control of the electrode separation [71]. In MCBJ experiments at room temperature, the low-bias conductance of single-molecule junctions can be studied both in solution [72] and in vacuum [73, 74]. The current-voltage characteristics of molecular junctions are typically studied in vacuum [7, 75–78], where the temperature can be varied between 300 K and less than 1 K. Apart from an exceptional electrode stability, MCBJ experiments at low temperatures bear an additional advantage: If the junctions are broken in a cryogenic vacuum, atomically clean electrode surfaces can be guaranteed.

1.3.2 THREE-TERMINAL MEASUREMENTS

Three-terminal measurements on molecular junctions are typically carried out in vacuum and at cryogenic temperatures, where quantum mechanical features in the transport characteristics can be resolved.

The majority of three-terminal experiments to date have been based on the electromigration method, in which a microfabricated wire is broken to create a nanometer-sized gap [8]. Electromigration - the displacement of metal atoms under the influence of electrical currents and fields - is a well-known mechanism of deterioration in microelectronic devices. Typically, it occurs at grain boundaries in metal interconnects, where it leads to the formation of voids and, eventually, the failure of the entire integrated circuit.

In molecular electronics, thin gold wires on top of highly doped Si substrates [79] or oxidized aluminum gates [80] are broken by electromigration to fabricate prototypical three-terminal devices (see Figure 1.4c). The method is hampered by the limited control over the electromigration process, which prevents a precise adjustment of the gap size and leads to low yields of molecular junctions around a few percent [81]. Moreover, it has been shown that electromigration can lead to extensive heating [82] and the formation of gold clusters in the source-drain gap [83], the spectroscopic signature of which can be similar to molecular junctions [81]. A combination of an active feedback scheme with thermally activated self-breaking can reduce the probability of cluster formation significantly [84], but the gap sizes obtained from this method still display a considerable spread.

The control over the nanoscale gap can be enhanced significantly by the in-situ fabrication of electrodes in an ultra-high vacuum (UHV) environment [85]. By means of repeated shadow evaporation and careful annealing at cryogenic temperatures, thin gold electrodes with a well-defined spacing can be fabricated directly on an aluminum gate (see Figure 1.4d). Three-terminal measurements in between the deposition steps help exclude the presence of metal clusters before the evaporation of molecules on the gap [14]. The formation of a single-molecule junction can then be identified through transport measurements. Due to the ultra-high vacuum, which is enhanced further at cryogenic temperatures, the in-situ fabrication of the electrodes offers excellent contamination control. However, the junction spacing cannot be varied during the single-molecule measurements, and the evaporation is limited to molecules with sufficiently high vapor pressures.

Three-terminal architectures with a variable source-drain gap - the most versatile devices for molecular electronics research - are scarce. In an early study, a STM has been combined with a microfabricated side gate to study the properties of organic clusters [86]. However, the mechanical stability of the junction formed by the tip and the substrate in such a setup is limited.

The combination of a mechanically controllable break junction with a gate electrode offers the best prospects for stable molecular junctions with full electrical and mechanical tunability. In the first gated MCBJs [87], the metal electrodes were microfabricated on ultra-thin silicon that served both as the flexible substrate as well as the common back gate (see Figure 1.4e). Due to the brittleness of the silicon the variation of the source-drain distance in these devices was limited to a few angstroms, and electromigration had to be used to create the initial electrode gap. To exploit the full potential of the MCBJ principle and circumvent the remaining drawbacks of the electromigration process, sufficiently flexible gated devices need to be developed. The second part of this Thesis is entirely dedicated to this goal.

1.3.3 Deposition methods for molecular electronics

The various experimental techniques for forming nanoscale electrodes are complemented by typical approaches to depositing a single molecule in the gap.

Transport measurements in ultra-high vacuum (UHV) can benefit from the controlled evaporation of molecular monolayers on clean metal surfaces. This method guarantees the best contamination control, but it is restricted to systems of limited molecular weight and sufficient thermal stability such as fullerenes [88–90] and small dithiols [14].

Vacuum-based experiments in MCBJs and electromigrated devices typically rely on other deposition schemes. At cryogenic temperatures, small molecules such as hydrogen or water may be condensed from the vapor phase [11, 91]. The application of larger molecules usually requires a solution phase before cooldown. Common approaches for molecule deposition range from the drop-casting of dilute solutions on open junctions [7, 19, 78] to the controlled formation of a (sub-)monolayer with subsequent rinsing [42, 92, 93]. The latter method may avoid complications due to the crystallization and oligomerization of molecules on the open junction. Furthermore, it is likely to reduce the influence of impurities from the solvent considerably. The rinsing step ensures that only strongly bound molecules remain adsorbed on the electrodes, as compared to the non-selective deposition in drop-casting experiments. In all cases, establishing and maintaining a single-molecule junction throughout cooldown remains a critical step of the experiment.

Break junction experiments at room temperature are mostly carried out in a millimolar solution of the molecule of interest [12, 31, 42, 94]. This approach is relatively robust and has been applied using various chemical anchoring groups and solvents. However, parasitic currents can obscure the signature of the molecular junction in polar solvents unless the electrodes are sufficiently insulated. Furthermore, contamination control is essential; impurities in the solvent may lead to artifacts in the electronic measurements.

1.4 THESIS OUTLINE

To lay the theoretical foundations of this Thesis, Chapter 2 reviews the basic concepts of charge transport in nanoscale conductors. It starts with a discussion of the conductance of metallic constrictions of decreasing diameters. The chapter then describes transport across single molecules in the regimes of Coulomb blockade and coherent tunneling. It is concluded with a glimpse at the experimental signatures of vibrational excitations and the Kondo effect.

Chapter 3 presents the two-terminal MCBJs and the cryogenic measurement setups that have been developed for this Thesis. Their design and their mechanical properties are discussed. Furthermore, the chapter introduces the measurement methods and analyses that are applied in the remainder of the Thesis.

In Chapter 4, the electrical characteristics of molecular model systems with amino and thiol anchoring groups are studied. A molecule deposition protocol is established that is based on the controlled self-assembly of the molecules on the as-fabricated MCBJs. Lowbias conductance measurements of thiol and amino-anchored hexane molecules confirm the suitability of the method but indicate that measurements in vacuum are generally limited by the surface density of molecules near the contact.

Chapter 5 presents conductance measurements on benzene molecules with a fullerene-based anchoring group. The conductance of the fullerene-anchored molecule is better defined than that of the corresponding dithiol, and its signature is stronger than that of benzenediamine. A new data analysis method confirms the stability of the fullerene anchoring and yields information on the lifetime of the molecular junctions.

Chapter 6 introduces novel gated MCBJs with suspended source-drain electrodes. The architecture represents a significant improvement compared to established devices on silicon, in that it does not require an electromigration step to create an initial gap. The electromechanical characteristics of the gated MCBJs are analyzed in detail, and their response to large gate voltages is exploited to form single-atom relays.

Chapter 7 presents low-temperature measurements on C_{60} in the gated mechanical break junction devices that were introduced in Chapter 6. Single-molecule junctions of the fullerenes can display a zero-bias peak in the differential conductance that is reminiscent of Kondo physics. The tuning of such a resonance by the gate voltage as well as the distance of the electrodes is demonstrated and analyzed with reference to the theory of the Kondo effect.

Chapter 8 concludes this Thesis with the presentation of an architecture for mechanically stable gated MCBJs. The direct deposition of the source-drain electrodes on the gate allows for efficient gating and precise mechanical control over the electrode gap. The functionality of the devices is demonstrated by tuning the Coulomb blockade characteristics of a nanoscale cluster.

REFERENCES

[1] R. P. Feynman, *There's Plenty of Room at the Bottom*, Engineering and Science pp. 32–36 (Feb 1960).

REFERENCES 11

[2] A. Aviram and M. A. Ratner, Molecular rectifiers, Chem. Phys. Lett. 29, 277 (1974).

- [3] J. Kilby, U.S. Patent 3,138,743, Texas Instruments (1958).
- [4] G. E. Moore, Cramming more components onto integrated circuits, Electronics **38**, 4 (1965).
- [5] P. S. Peercy, *The drive to miniaturization*, Nature **406**, 1023 (2000).
- [6] International Roadmap Committee, Tech. Rep., Semiconductor Industry Association (2007).
- [7] M. A. Reed, C. Zhou, C. J. Muller, T. P. Burgin, and J. M. Tour, *Conductance of a Molecular Junction*, Science **278**, 252 (1997).
- [8] H. Park, A. K. L. Lim, A. P. Alivisatos, J. Park, and P. L. McEuen, *Fabrication of metallic electrodes with nanometer separation by electromigration*, Appl. Phys. Lett. **75**, 301 (1999).
- [9] Z. J. Donhauser, B. A. Mantooth, K. F. Kelly, L. A. Bumm, J. D. Monnell, J. J. Stapleton, J. Price, D. W., A. M. Rawlett, D. L. Allara, J. M. Tour, et al., *Conductance Switching in Single Molecules Through Conformational Changes*, Science 292, 2303 (2001).
- [10] X. D. Cui, A. Primak, X. Zarate, J. Tomfohr, O. F. Sankey, A. L. Moore, T. A. Moore, D. Gust, G. Harris, and S. M. Lindsay, *Reproducible Measurement of Single-Molecule Conductivity*, Science 294, 571 (2001).
- [11] R. H. M. Smit, Y. Noat, C. Untiedt, N. D. Lang, M. C. van Hemert, and J. M. van Ruitenbeek, *Measurement of the conductance of a hydrogen molecule*, Nature **419**, 906 (2002).
- [12] B. Xu and N. J. Tao, Measurement of Single-Molecule Resistance by Repeated Formation of Molecular Junctions, Science **301**, 1221 (2003).
- [13] W. Haiss, H. van Zalinge, S. J. Higgins, D. Bethell, H. Hobenreich, D. J. Schiffrin, and R. J. Nichols, *Redox State Dependence of Single Molecule Conductivity*, J. Am. Chem. Soc. **125**, 15294 (2003).
- [14] S. Kubatkin, A. Danilov, M. Hjort, J. Cornil, J.-L. Brédas, N. Stuhr-Hansen, P. Hedegård, and T. Bjørnholm, *Single-electron transistor of a single organic molecule with access to several redox states*, Nature **425**, 698 (2003).
- [15] T. Dadosh, Y. Gordin, R. Krahne, I. Khivrich, D. Mahalu, V. Frydman, J. Sperling, A. Yacoby, and I. Bar-Joseph, *Measurement of the conductance of single conjugated molecules*, Nature 436, 677 (2005).
- [16] L. Venkataraman, J. E. Klare, C. Nuckolls, M. S. Hybertsen, and M. L. Steigerwald, *Dependence of single-molecule junction conductance on molecular conformation*, Nature 442, 904 (2006).

[17] J. R. Quinn, F. W. Foss, L. Venkataraman, M. S. Hybertsen, and R. Breslow, Single-Molecule Junction Conductance through Diaminoacenes, J. Am. Chem. Soc. 129, 6714 (2007).

- [18] L. Venkataraman, Y. S. Park, A. C. Whalley, C. Nuckolls, M. S. Hybertsen, and M. L. Steigerwald, *Electronics and Chemistry: Varying Single-Molecule Junction Conductance Using Chemical Substituents*, Nano Lett. 7, 502 (2007).
- [19] J. Reichert, R. Ochs, D. Beckmann, H. B. Weber, M. Mayor, and H. v. Löhneysen, *Driving Current through Single Organic Molecules*, Phys. Rev. Lett. **88**, 176804 (2002).
- [20] X. Li, J. He, J. Hihath, B. Xu, S. M. Lindsay, and N. Tao, *Conductance of Single Alkanedithiols: Conduction Mechanism and Effect of Molecule-Electrode Contacts*, J. Am. Chem. Soc. **128**, 2135 (2006).
- [21] J. Ulrich, D. Esrail, W. Pontius, L. Venkataraman, D. Millar, and L. H. Doerrer, *Variability of Conductance in Molecular Junctions*, J. Phys. Chem. B **110**, 2462 (2006).
- [22] E. A. Osorio, T. Bjørnholm, J.-M. Lehn, M. Ruben, and H. S. J. van der Zant, Single-molecule transport in three-terminal devices, J. Phys.: Condens. Matter 20, 374121 (2008).
- [23] A. Danilov, S. Kubatkin, S. Kafanov, P. Hedegård, N. Stuhr-Hansen, K. Moth-Poulsen, and T. Bjørnholm, Electronic Transport in Single Molecule Junctions: Control of the Molecule-Electrode Coupling through Intramolecular Tunneling Barriers, Nano Lett. 8, 1 (2008).
- [24] S. Natarajan, M. Armstrong, M. Bost, R. Brain, M. Brazier, C.-H. Chang, V. Chikarmane, M. Childs, H. Deshpande, K. Dev, et al., in *Electron Devices Meeting*, 2008. *IEDM 2008. IEEE International* (2008), pp. 1–3.
- [25] E. Leary, H. Höbenreich, S. J. Higgins, H. van Zalinge, W. Haiss, R. J. Nichols, C. M. Finch, I. Grace, C. J. Lambert, R. McGrath, et al., *Single-Molecule Solvation-Shell Sensing*, Phys. Rev. Lett. **102**, 086801 (2009).
- [26] H. B. Akkerman, P. W. M. Blom, D. M. de Leeuw, and B. de Boer, *Towards molecular electronics with large-area molecular junctions*, Nature **441**, 69 (2006).
- [27] E. C. P. Smits, S. G. J. Mathijssen, P. A. van Hal, S. Setayesh, T. C. T. Geuns, K. A. H. A. Mutsaers, E. Cantatore, H. J. Wondergem, O. Werzer, R. Resel, et al., *Bottom-up organic integrated circuits*, Nature **455**, 956 (2008).
- [28] S. Lindsay and M. Ratner, *Molecular Transport Junctions: Clearing Mists*, Adv. Mater. **19**, 23 (2007).
- [29] L. Patrone, S. Palacin, J. Charlier, F. Armand, J. P. Bourgoin, H. Tang, and S. Gauthier, Evidence of the Key Role of Metal-Molecule Bonding in Metal-Molecule-Metal Transport Experiments, Phys. Rev. Lett. 91, 096802 (2003).

REFERENCES 13

[30] F. Chen, X. Li, J. Hihath, Z. Huang, and N. Tao, Effect of Anchoring Groups on Single-Molecule Conductance: Comparative Study of Thiol-, Amine-, and Carboxylic-Acid-Terminated Molecules, J. Am. Chem. Soc. 128, 15874 (2006).

- [31] L. Venkataraman, J. E. Klare, I. W. Tam, C. Nuckolls, M. S. Hybertsen, and M. L. Steigerwald, *Single-Molecule Circuits with Well-Defined Molecular Conductance*, Nano Lett. **6**, 458 (2006).
- [32] Y. S. Park, A. C. Whalley, M. Kamenetska, M. L. Steigerwald, M. S. Hybertsen, C. Nuckolls, and L. Venkataraman, Contact Chemistry and Single-Molecule Conductance: A Comparison of Phosphines, Methyl Sulfides, and Amines, J. Am. Chem. Soc. 129, 15768 (2007).
- [33] R. Yamada, H. Kumazawa, T. Noutoshi, S. Tanaka, and H. Tada, *Electrical Conductance of Oligothiophene Molecular Wires*, Nano Lett. **8**, 1237 (2008).
- [34] J. M. Tour, L. Jones, D. L. Pearson, J. J. S. Lamba, T. P. Burgin, G. M. Whitesides, D. L. Allara, A. N. Parikh, and S. Atre, Self-Assembled Monolayers and Multilayers of Conjugated Thiols, α,ω-Dithiols, and Thioacetyl-Containing Adsorbates. Understanding Attachments between Potential Molecular Wires and Gold Surfaces, J. Am. Chem. Soc. 117, 9529 (1995).
- [35] J. C. Love, L. A. Estroff, J. K. Kriebel, R. G. Nuzzo, and G. M. Whitesides, Self-Assembled Monolayers of Thiolates on Metals as a Form of Nanotechnology, Chem. Rev. 105, 1103 (2005).
- [36] L. Kankate, A. Turchanin, and A. Gölzhäuser, *On the Release of Hydrogen from the S–H groups in the Formation of Self-Assembled Monolayers of Thiols*, Langmuir **25**, 10435 (2009).
- [37] E. Delamarche, B. Michel, H. Kang, and C. Gerber, *Thermal Stability of Self-Assembled Monolayers*, Langmuir **10**, 4103 (1994).
- [38] Z. Huang, F. Chen, P. A. Bennett, and N. Tao, *Single Molecule Junctions Formed via Au-Thiol Contact: Stability and Breakdown Mechanism*, J. Am. Chem. Soc. **129**, 13225 (2007).
- [39] D. Losic, J. G. Shapter, and J. J. Gooding, *Influence of Surface Topography on Alkanethiol SAMs Assembled from Solution and by Microcontact Printing*, Langmuir **17**, 3307 (2001).
- [40] M. Kawasaki, T. Sato, T. Tanaka, and K. Takao, *Rapid Self-Assembly of Alkanethiol Monolayers on Sputter-Grown Au*(111), Langmuir **16**, 1719 (2000).
- [41] A. Kahn (2009), Princeton University, Surface/Interface Science Laboratory, URL http://www.princeton.edu/~kahnlab/images/Au.html.

[42] C. Li, I. Pobelov, T. Wandlowski, A. Bagrets, A. Arnold, and F. Evers, *Charge Transport in Single Au/alkanedithiol/Au Junctions: Coordination Geometries and Conformational Degrees of Freedom*, J. Am. Chem. Soc. **130**, 318 (2008).

- [43] S. Uemura, P. Samory, M. Kunitake, C. Hirayamaa, and J. P. Rabe, *Crystalline C*₆₀ *monolayers at the solid–organic solution interface*, J. Mater. Chem. **12**, 3366 (2002).
- [44] H. B. Akkerman and B. de Boer, *Electrical conduction through single molecules and self-assembled monolayers*, J. Phys.: Condens. Matter **20**, 013001 (2008).
- [45] W. Azzam, B. I. Wehner, R. A. Fischer, A. Terfort, and C. Woll, *Bonding and Orientation in Self-Assembled Monolayers of Oligophenyldithiols on Au Substrates*, Langmuir **18**, 7766 (2002).
- [46] A. Niklewski, W. Azzam, T. Strunskus, R. A. Fischer, and C. Woll, *Fabrication of Self-Assembled Monolayers Exhibiting a Thiol-Terminated Surface*, Langmuir **20**, 8620 (2004).
- [47] C. Xu, L. Sun, L. J. Kepley, R. M. Crooks, and A. J. Ricco, *Molecular interactions between organized, surface-confined monolayers and vapor-phase probe molecules.* 6. *In-situ FT-IR external reflectance spectroscopy of monolayer adsorption and reaction chemistry*, Anal. Chem. **65**, 2102 (1993).
- [48] L. O. Brown and J. E. Hutchison, *Controlled Growth of Gold Nanoparticles during Lig*and Exchange, J. Am. Chem. Soc. **121**, 882 (1999).
- [49] A. Kumar, S. Mandal, P. Selvakannan, R. Pasricha, A. B. Mandale, and M. Sastry, *Investigation into the Interaction between Surface-Bound Alkylamines and Gold Nanoparticles*, Langmuir **19**, 6277 (2003).
- [50] Z. Li and D. S. Kosov, *Nature of well-defined conductance of amine-anchored molecular junctions: Density functional calculations*, Phys. Rev. B **76**, 035415 (2007).
- [51] M. S. Hybertsen, L. Venkataraman, J. E. Klare, A. C. Whalley, M. L. Steigerwald, and C. Nuckolls, *Amine-linked single-molecule circuits: systematic trends across molecular families*, J. Phys.: Condens. Matter **20**, 374115 (2008).
- [52] W. C. Bigelow, D. L. Pickett, and W. A. Zisman, *Oleophobic monolayers*. *I. Films adsorbed from solution in non-polar liquids*, J. Colloid Science **1**, 513 (1946).
- [53] W. C. Bigelow, E. Glass, and W. A. Zisman, *Oleophobic monolayers. II. Temperature effects and energy of adsorption*, J. Colloid Science **2**, 563 (1947).
- [54] D. V. Leff, L. Brandt, and J. R. Heath, Synthesis and Characterization of Hydrophobic, Organically-Soluble Gold Nanocrystals Functionalized with Primary Amines, Langmuir 12, 4723 (1996).
- [55] H. W. Kroto, J. R. Heath, S. C. O'Brien, R. F. Curl, and R. E. Smalley, *C*₆₀: *Buckminster-fullerene*, Nature **318**, 162 (1985).

REFERENCES 15

[56] B. W. Hoogenboom, R. Hesper, L. H. Tjeng, and G. A. Sawatzky, *Charge transfer and doping-dependent hybridization of C*₆₀ *on noble metals*, Phys. Rev. B **57**, 11939 (1998).

- [57] C.-T. Tzeng, W.-S. Lo, J.-Y. Yuh, R.-Y. Chu, and K.-D. Tsuei, *Photoemission, near-edge* x-ray-absorption spectroscopy, and low-energy electron-diffraction study of C_{60} on Au(111) surfaces, Phys. Rev. B **61**, 2263 (2000).
- [58] E. I. Altman and R. J. Colton, *Nucleation, growth, and structure of fullerene films on Au(111)*, Surf. Sci. **279**, 49 (1992).
- [59] S. Yoshimoto, R. Narita, E. Tsutsumi, M. Matsumoto, K. Itaya, O. Ito, K. Fujiwara, Y. Murata, and K. Komatsu, Adlayers of Fullerene Monomer and [2 + 2]-Type Dimer on Au(111) in Aqueous Solution Studied by in Situ Scanning Tunneling Microscopy, Langmuir 18, 8518 (2002).
- [60] A. Kuzume, E. Herrero, J. M. Feliu, R. J. Nichols, and D. J. Schiffrin, *Fullerene mono-layers adsorbed on high index gold single crystal surfaces*, Phys. Chem. Chem. Phys. **6**, 619 (2004).
- [61] G. Binnig, H. Rohrer, C. Gerber, and E. Weibel, *Tunneling through a controllable vac-uum gap*, Appl. Phys. Lett. **40**, 178 (1982).
- [62] A. Aviram, C. Joachim, and M. Pomerantz, Evidence of switching and rectification by a single molecule effected with a scanning tunneling microscope, Chem. Phys. Lett. **146**, 490 (1988).
- [63] A. N. Broers, *Resolution limits for electron-beam lithography*, IBM J. Res. Dev. **32**, 502 (1988).
- [64] A. Aviram, *Molecules for memory, logic, and amplification*, J. Am. Chem. Soc. **110**, 5687 (1988).
- [65] S. M. Lindsay, Y. Li, J. Pan, T. Thundat, L. A. Nagahara, P. Oden, J. A. DeRose, U. Knipping, and J. W. White, *Studies of the electrical properties of large molecular adsorbates*, Proceedings of the International Conference on Scanning Tunneling Microscopy/Spectroscopy 9, 1096 (1991).
- [66] M. Pomerantz, A. Aviram, R. A. McCorkle, L. Li, and A. G. Schrott, *Rectification of STM Current to Graphite Covered with Phthalocyanine Molecules*, Science **255**, 1115 (1992).
- [67] U. Dürig, O. Züger, B. Michel, L. Häussling, and H. Ringsdorf, Electronic and mechanical characterization of self-assembled alkanethiol monolayers by scanning tunneling microscopy combined with interaction-force-gradient sensing, Phys. Rev. B 48, 1711 (1993).
- [68] D. S. Seferos, A. S. Blum, J. G. Kushmerick, and G. C. Bazan, Single-Molecule Charge-Transport Measurements that Reveal Technique-Dependent Perturbations, J. Am. Chem. Soc. 128, 11260 (2006).

[69] J. Repp, G. Meyer, S. M. Stojković, A. Gourdon, and C. Joachim, *Molecules on Insulating Films: Scanning-Tunneling Microscopy Imaging of Individual Molecular Orbitals*, Phys. Rev. Lett. **94**, 026803 (2005).

- [70] C. J. Muller, J. M. van Ruitenbeek, and L. J. de Jongh, *Experimental observation of the transition from weak link to tunnel junction*, Physica C **191**, 485 (1992).
- [71] J. M. van Ruitenbeek, A. Alvarez, I. Piñeyro, C. Grahmann, P. Joyez, M. H. Devoret, D. Esteve, and C. Urbina, *Adjustable nanofabricated atomic size contacts*, Rev. Sci. Instrum. 67, 108 (1996).
- [72] L. Grüter, M. T. González, R. Huber, M. Calame, and C. Schönenberger, *Electrical Conductance of Atomic Contacts in Liquid Environments*, Small 1, 1067 (2005).
- [73] M. Tsutsui, Y. Teramae, S. Kurokawa, and A. Sakai, *High-conductance states of single benzenedithiol molecules*, Appl. Phys. Lett. **89**, 163111 (2006).
- [74] M. Kiguchi and K. Murakoshi, *Conductance of Single C*₆₀ *Molecule Bridging Metal Electrodes*, J. Phys. Chem. C **112**, 8140 (2008).
- [75] C. Kergueris, J.-P. Bourgoin, S. Palacin, D. Esteve, C. Urbina, M. Magoga, and C. Joachim, *Electron transport through a metal-molecule-metal junction*, Phys. Rev. B 59, 12505 (1999).
- [76] J. Reichert, H. B. Weber, M. Mayor, and H. v. Löhneysen, *Low-temperature conductance measurements on single molecules*, Appl. Phys. Lett. **82**, 4137 (2003).
- [77] T. Böhler, A. Edtbauer, and E. Scheer, *Conductance of individual C*₆₀ *molecules measured with controllable gold electrodes*, Phys. Rev. B **76**, 125432 (2007).
- [78] E. Lörtscher, H. B. Weber, and H. Riel, *Statistical Approach to Investigating Transport through Single Molecules*, Phys. Rev. Lett. **98**, 176807 (2007).
- [79] H. Park, J. Park, A. K. Lim, E. H. Anderson, P. A. Alivisatos, and P. L. McEuen, *Nanome-chanical oscillations in a single-C*₆₀ *transistor*, Nature **407**, 57 (2000).
- [80] W. Liang, M. P. Shores, M. Bockrath, J. R. Long, and H. Park, *Kondo resonance in a single-molecule transistor*, Nature **417**, 725 (2002).
- [81] H. S. J. van der Zant, Y.-V. Kervennic, M. Poot, K. O'Neill, Z. de Groot, J. M. Thijssen, H. B. Heersche, N. Stuhr-Hansen, T. Bjørnholm, D. Vanmaekelbergh, et al., *Molecular three-terminal devices: fabrication and measurements*, Faraday Discuss. 131, 347 (2006).
- [82] M. L. Trouwborst, S. J. van der Molen, and B. J. van Wees, *The role of Joule heating in the formation of nanogaps by electromigration*, J. Appl. Phys. **99**, 114316 (2006).
- [83] T. Taychatanapat, K. I. Bolotin, F. Kuemmeth, and D. C. Ralph, *Imaging Electromigration during the Formation of Break Junctions*, Nano Lett. **7**, 652 (2007).

References 17

[84] K. O'Neill, E. A. Osorio, and H. S. J. van der Zant, *Self-breaking in planar few-atom Au constrictions for nanometer-spaced electrodes*, Appl. Phys. Lett. **90**, 133109 (2007).

- [85] S. E. Kubatkin, A. V. Danilov, H. Olin, and T. Claeson, *Tunneling Through a Single Quench-condensed Cluster*, J. Low Temp. Phys. 118, 307 (2000).
- [86] E. S. Soldatov, V. V. Khanin, A. S. Trifonov, D. E. Presnov, S. A. Yakovenko, G. B. Khomutov, C. P. Gubin, and V. V. Kolesov, Single-electron transistor based on a single cluster molecule at room temperature, JETP Letters 64, 556 (1996).
- [87] A. R. Champagne, A. N. Pasupathy, and D. C. Ralph, *Mechanically Adjustable and Electrically Gated Single-Molecule Transistors*, Nano Lett. **5**, 305 (2005).
- [88] T. R. Ohno, Y. Chen, S. E. Harvey, G. H. Kroll, J. H. Weaver, R. E. Haufler, and R. E. Smalley, *C*₆₀ bonding and energy-level alignment on metal and semiconductor surfaces, Phys. Rev. B **44**, 13747 (1991).
- [89] T. Böhler, J. Grebing, A. Mayer-Gindner, H. v. Löhneysen, and E. Scheer, *Mechanically controllable break-junctions for use as electrodes for molecular electronics*, Nanotechnology **15**, S465 (2004).
- [90] A. V. Danilov, S. E. Kubatkin, S. G. Kafanov, and T. Bjørnholm, Strong electronic coupling between single C_{60} molecules and gold electrodes prepared by quench condensation at 4 K. A single molecule three terminal device study, Faraday Discuss. **131**, 337 (2006).
- [91] O. Tal, M. Krieger, B. Leerink, and J. M. van Ruitenbeek, Electron-Vibration Interaction in Single-Molecule Junctions: From Contact to Tunneling Regimes, Phys. Rev. Lett. 100, 196804 (2008).
- [92] M. Fujihira, M. Suzuki, S. Fujii, and A. Nishikawa, *Currents through single molecular junction of Au/hexanedithiolate/Au measured by repeated formation of break junction in STM under UHV: Effects of conformational change in an alkylene chain from gauche to trans and binding sites of thiolates on gold, Phys. Chem. Chem. Phys. 8*, 3876 (2006).
- [93] W. Haiss, R. J. Nichols, H. van Zalinge, S. J. Higgins, D. Bethell, and D. J. Schiffrin, *Measurement of single molecule conductivity using the spontaneous formation of molecular wires*, Phys. Chem. Chem. Phys. **6**, 4330 (2004).
- [94] L. Grüter, F. Cheng, T. T. Heikkilä, M. T. González, F. Diederich, C. Schönenberger, and M. Calame, *Resonant tunnelling through a C*₆₀ *molecular junction in a liquid environment*, Nanotechnology **16**, 2143 (2005).

THEORETICAL BACKGROUND

This chapter reviews the physics of conductors along a top-down route. After presenting the characteristic length scales of electron transport, the tour starts with a macroscopic wire in the diffusive transport regime. The discussion then focuses on classical and quantum ballistic transport. A section on electron tunneling across a vacuum gap between two electrodes concludes the first part of the chapter. To model transport across a single-molecule junction an electronic level is introduced in the electrode gap. After presenting the regimes of sequential and coherent electron tunneling the chapter is concluded with a discussion of selected spectroscopic features in low-temperature measurements, both in two- and three-terminal configurations.

2.1 ELECTRON TRANSPORT IN METALLIC CONDUCTORS

The first part of this background chapter covers the conductive properties of metallic wires. Conceptually, it follows a break junction experiment; as the diameter of a wire is reduced, different transport regimes are entered (see Figure 2.1 for a schematic). Before discussing these regimes in detail, we review the microscopic principles of electron transport.

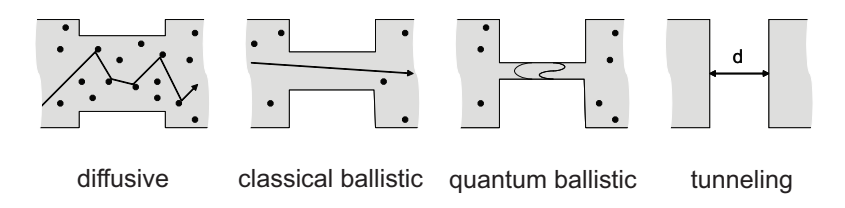


FIGURE 2.1: Schematic of the different transport regimes of a conductor. The width of the central constriction - the smallest dimension of the conductor - determines the transport mechanism.

2.1.1 THE IMPORTANCE OF LENGTH SCALES

On the microscopic scale, any conductor may be described by four characteristic length scales: the elastic scattering length l_e , the inelastic scattering length l_i , the phase coherence length l_{ϕ} , and the Fermi wavelength λ_F . Their relations to the macroscopic conductor dimensions determine the physics of charge transport. In the particular case of a break junction experiment, the radius R of the central constriction, which is much smaller than the wire length L, governs transport through the wire.

The elastic scattering length l_e in a conductor corresponds to the mean free path along which an electron can travel before undergoing a change in momentum. In metals, elastic scattering is typically caused by lattice defects such as vacancies, interstitials, dislocations, and grain boundaries. Elastic scattering dominates the electrical properties of macroscopic metal wires at low temperatures, where transport is in the diffusive regime (see Section 2.1.2). In metal point contacts with a small radius R the number of defects and the probability of elastic scattering can be reduced significantly, leading to so-called classical ballistic transport (see Section 2.1.3). A molecular junction in between two atomic-scale electrodes, in turn, typically represents a distortion to the electronic structure of the metal and can act as a strong elastic scattering center (see Section 2.2.3).

The inelastic scattering length l_i indicates the mean distance an electron can travel before exchanging energy with other electrons or lattice vibrations. In bulk metals the probability of scattering on lattice vibrations, so-called phonons, is related to the phonon density of states. At room temperature, the number of occupied phonon states is large and conduction electrons are spread over a range of energies around the Fermi energy E_F . Since the phonon density of states increases with energy, the probability for inelastic scattering is high, and it dominates room-temperature transport in macroscopic wires. At low temperatures, only the low-energy tail of the phonon density of states is occupied, and inelastic

scattering is reduced significantly. In molecular junctions, inelastic scattering on vibrational modes of the molecule, so-called vibrons, can lead to a spectroscopic fingerprint in low-temperature transport (see Section 2.2.5).

Scattering events that include electrons, phonons, or magnetic impurities may cause a loss of the phase information of the wavefunction of the electron. The characteristic distance between two such events is given by the phase-coherence length l_{ϕ} . When $l_{e} < l_{\phi}$, the wave nature of the electrons leads to quantum interference and transport phenomena such as universal conductance fluctuations [1]. In gold at 1 K, the coherence length can be as large as 1 μ m [2], leading to signatures of quantum interference in the current-voltage characteristics of point contacts [3].

The Fermi wavelength λ_F is the final important length scale of a conductor. It is the wavelength of electrons at the Fermi-energy E_F , which, in first order, carry the current at low bias voltages. The Fermi wavelength can be derived from the Fermi energy according to

$$E_F = \frac{\hbar^2 k_F^2}{2m_e} = \frac{h^2}{2m_e \lambda_F^2},\tag{2.1}$$

where $\hbar=h/2\pi$ is the reduced Planck's constant, k_F is the Fermi wavevector, and m_e is the mass of an electron in the conductor. In gold with $E_F=5.4$ eV, the Fermi wavelength is about 5.3 Å. Since this value is on the order of the atomic spacing in bulk gold, it is not surprising that the electrical properties of atomic-scale conductors are determined by quantum mechanics. Transport in the regime where $R\approx \lambda_F$ and $R<< l_e, l_\phi$ is termed quantum ballistic (see Section 2.1.4).

2.1.2 DIFFUSIVE TRANSPORT IN MACROSCOPIC WIRES

For a macroscopic wire with $L,R>>l_e$, the microscopic path of the conduction electrons is determined by multiple elastic scattering events. In this so-called diffusive transport regime, an applied voltage induces a net macroscopic motion of the electrons and a measurable current through the wire. A classical description of diffusive transport has been put forward by Drude, who formulated kinetic equations for the propagation of electrons in metals [4]. The current density in a diffusive conductor is given by the mean propagation speed $\langle v \rangle_{\vec{E}}$ of the electrons in the direction of the applied electric field, the electron density n_e , and the unit charge e>0:

$$J_{\vec{E}} = -e \langle v \rangle_{\vec{E}} \, n_e. \tag{2.2}$$

The electrical conductance G of a diffusive macroscopic wire follows Ohm's law

$$G = \frac{\pi R^2}{\rho L},\tag{2.3}$$

where ρ is the resistivity of the metal. Since the conductance of an ohmic wire scales as R^2 , Equation 2.3 suggests that $G \to 0$ for atomic and molecular conductors. However, the probability of elastic scattering decreases rapidly with decreasing conductor dimensions, and nanoscale transport is no longer diffusive.

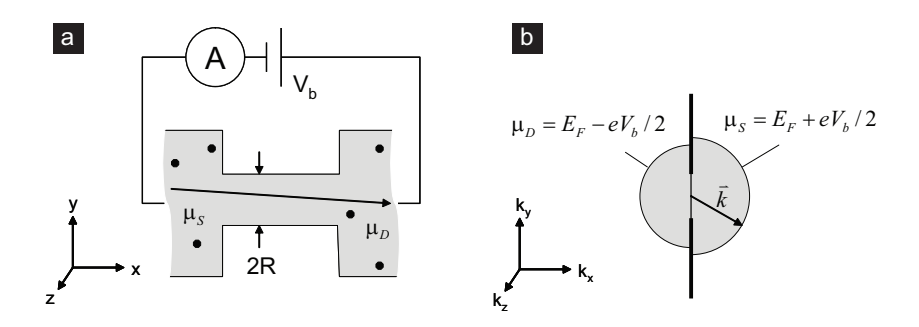


FIGURE 2.2: Transport in the classical ballistic regime. (a) Schematic of a constriction through which electrons may pass without elastic scattering. (b) Simplified \vec{k} -space representation of the propagating states in the constriction.

2.1.3 Nanoscale contacts in the semi-classical approximation

If the constriction of the wire is small enough such that $\lambda_F << R << l_e$, electrons can pass without encountering any elastic scattering center (see Figure 2.2a). This is the regime of classical ballistic transport.

The ballistic conductance through a constriction with a circular cross section πR^2 can be modeled based on a number of approximations. For the theoretical treatment, it is useful to view the regions adjacent to the constriction as electron reservoirs. This implies that their density of states (DOS) is bulk-like and not affected by electron transfer processes. The electron distribution in the reservoirs is then only determined by the temperature T and the chemical potentials μ_{α} , where $\alpha = S, D$ denotes the source and drain, respectively. It follows the Fermi-Dirac-distribution,

$$f(E,\mu_{\alpha}) = \frac{1}{1 + \exp\left(\frac{E - \mu_{\alpha}}{k_{B}T}\right)},\tag{2.4}$$

where E is the energy and k_B is the Boltzmann constant. In equilibrium and in the limit of zero temperature, the distribution reduces to a step function, the value of which changes to 1 at $E = \mu_{\alpha} = E_F$.

A bias voltage V_b between the source and the drain induces a difference in the chemical potentials of

$$\mu_S - \mu_D = eV_h. \tag{2.5}$$

An analytical expression of the resulting current can be derived from a representation of the density of states at the location of the constriction in \vec{k} -space (see Figure 2.2b). For a free electron gas in equilibrium, all occupied states are enclosed by a sphere of radius k_F . In the case of a symmetric voltage drop across the constriction, the chemical potentials in the reservoirs are shifted to $\mu_S = E_F + eV_b/2$ and $\mu_D = E_F - eV_b/2$, respectively. This leads to a difference in the occupation of the density of states that can be accounted for by two half-spheres. These enclose all electrons coming from the source and the drain,

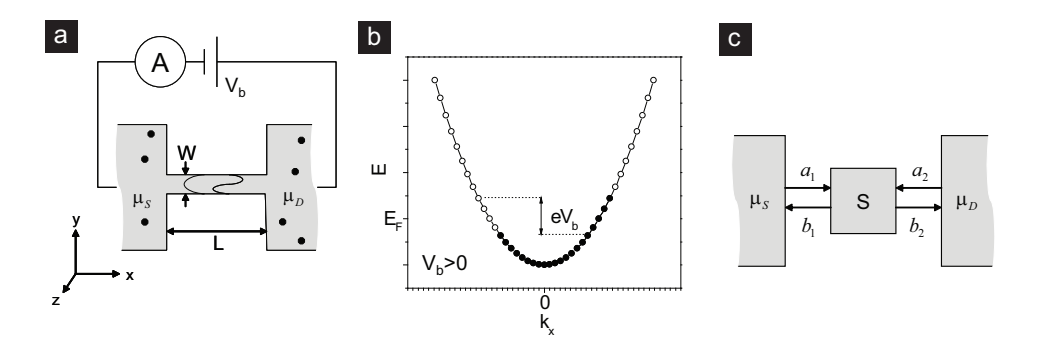


FIGURE 2.3: (a) Schematic of a constriction in the quantum ballistic regime. The small width leads to the formation of well-defined transverse modes, so-called conductance channels. (b) Dispersion curve for propagating states in the channel. The application of a bias voltage leads to a difference in the chemical potentials of the reservoirs and electron transport along the constriction. Filled circles correspond to occupied left and right-traveling states. (c) Representation of a generalized constriction in the scattering formalism.

respectively. The imbalance in the populations of right and left-traveling states leads to a net flow of electrons to the right, i.e., in the direction of the smallest chemical potential. The representation in Figure 2.2b allows us to rewrite the current density per unit area as a volume integral:

$$J_{x} = -g_{s}e \oint D_{3D}(\vec{k})\nu_{x}(\vec{k})d^{3}\vec{k}, \qquad (2.6)$$

where $D_{3D} = (\pi)^{-3}$ is the density of states in 3-dimensional k-space, $v_x = v \cos \phi$ is the electron velocity in x-direction, and g_s accounts for spin degeneracy. After integration over the area of the constriction with radius R the conductance becomes

$$G = \frac{2e^2}{h} \left(\frac{k_F R}{2}\right)^2. \tag{2.7}$$

This expression is known as the Sharvin conductance [2]. Despite its semi-classical derivation, it is valid for metal point contacts with diameters down to a few nanometers. However, once the size of the contact becomes comparable to the Fermi wavelength λ_F , the wave character of the electrons needs to be taken into account.

2.1.4 QUANTUM BALLISTIC TRANSPORT

As the diameter of the constriction approaches the Fermi wavelength λ_F and $R << l_e, l_\phi$, transport enters the quantum ballistic regime. A schematic of a wire with a constriction in this range is presented in Figure 2.3a. It is useful to investigate the conductive properties of the isolated constriction first; the role of the interfaces with the reservoirs will be discussed in Section 2.1.5.

In a simple, straight wire, the dispersion relation for non-interacting electrons can be writ-

ten as

$$E = \frac{\hbar^2}{2m_e} \left[\left(n_x \frac{\pi}{L_x} \right)^2 + \left(n_y \frac{\pi}{L_y} \right)^2 + \left(n_z \frac{\pi}{L_z} \right)^2 \right], \tag{2.8}$$

where the n_q are the quantum numbers and the L_q are the conductor dimensions. If transport along the length L of the constriction is assumed to be bulk-like, $L_x \to \infty$ such that the wavevector $k_x = n_x \pi/L_x$ is quasi-continuous. The width of the constriction, which is on the order of the Fermi wavelength λ_F , causes a confinement of the electronic states in y and z. Equation 2.8 can then be modified to obtain

$$E = E_{Tn} + \frac{\hbar^2 k_x^2}{2m_e},\tag{2.9}$$

where the E_{Tn} account for the discrete energy spectrum due to the lateral confinement. Analogous to optical waveguides, the propagating states in the constriction may be viewed as transmission modes. Due to the small radius R the energy difference between successive E_{Tn} is usually large, so that we can restrict our discussion to a single mode, or a so-called conductance channel. Figure 2.3b presents the dispersion relation for electrons traveling in one channel. Similar to the discussion in the previous section, the states may be separated according to their propagation direction. In equilibrium, both left- and right-traveling states will be filled up to the Fermi energy. Upon the application of a bias voltage V_b , the chemical potentials of the reservoirs shift. The resulting current can be obtained from an integration over the density of states as

$$I = \frac{g_s e}{2} \int_{-\infty}^{\infty} v(E) D_{1D}(E) \left(f\left(E, \mu_S\right) - f\left(E, \mu_D\right) \right) dE, \tag{2.10}$$

where the factor 1/2 limits the integral to right-moving electrons. The density of states is given by $D_{1D}(E) = D_{1D}(k_x) (dE/dk_x)^{-1} = (\pi\hbar)^{-1} \sqrt{m_e/2E}$. With T = 0 K, $g_s = 2$, and $v(E) = \sqrt{2E/m_e}$, one obtains

$$I = \frac{2e}{h} \int_{E_F - eV_b/2}^{E_F + eV_b/2} dE = \frac{2e^2}{h} V_b.$$
 (2.11)

Hence, the conductance of the single channel is given by

$$G = \frac{2e^2}{h} \equiv G_0 \approx 77.5 \mu S,$$
 (2.12)

the quantum of conductance. It has appeared earlier in this chapter, namely as the prefactor in the Sharvin conductance of a classical-ballistic contact (see Equation 2.7). For an ideal quantum ballistic wire with a single transmission mode the conductance is exactly one G_0 and completely independent of the wire dimensions and the Fermi energy. Quantized conductance is a fundamental property of nanoscale conductors and has been observed in high-mobility semiconductors [5], metallic point contacts [6], and carbon nanotubes [7].

2.1.5 SCATTERING APPROACH FOR POINT CONTACTS

The previous derivation was based on a single, fully transparent conductance channel. In realistic nanoscale conductors, however, several channels may be present and elastic scattering events from the neck of the constriction back into the reservoirs need to be considered. Transport can then be described by a scattering formalism that has been developed by Landauer [8] and Büttiker [9]. In this framework, the nanoscale system is treated as a scatterer that couples incoming and outgoing states phase-coherently via a scattering matrix \hat{s} as

$$\begin{pmatrix} b_1 \\ b_2 \end{pmatrix} = \begin{pmatrix} \hat{s}_{11} & \hat{s}_{12} \\ \hat{s}_{21} & \hat{s}_{22} \end{pmatrix} \begin{pmatrix} a_1 \\ a_2 \end{pmatrix}$$
 (2.13)

where a_{α} and b_{α} represent incoming and outgoing states, respectively (see Figure 2.3c). Current conservation requires the scattering matrix to be unitary with $\hat{s}^{\dagger}\hat{s} = \hat{1}$. It may also be written as

$$\hat{s} = \begin{pmatrix} \hat{r} & \hat{t}' \\ \hat{t} & \hat{r}' \end{pmatrix} \tag{2.14}$$

where the submatrices \hat{t} , \hat{t}' , \hat{r} , and \hat{r}' describe the transmission and the reflection of electrons on both sides of the constriction. For time reversal symmetry (B=0), \hat{s} is symmetric and $\hat{t}'=\hat{t}^T$. The eigenvalues of $\hat{t}^{\dagger}\hat{t}$ correspond to the transmission probabilities T_n in all n eigenchannels of the system and yield the total conductance,

$$G = G_0 Tr \left[\hat{t}^{\dagger} \hat{t} \right] = G_0 \sum_n T_n. \tag{2.15}$$

2.1.6 VACUUM TUNNELING

In this section we discuss the last stage of a break junction experiment - a vacuum gap between two metal electrodes at a distance d (see Figure 2.4a). In the scattering approach, the potential barrier of the vacuum may be viewed as a strong scatterer with a very low transmission probability for incident electrons.

To derive an expression for the transmission at small bias voltages, the tunneling contact may be modeled as a rectangular barrier of width d and height Φ_m in the energy diagram of the junction (see Figure 2.4b). Here, Φ_m corresponds to the work function of the metal. For simplicity, all energies are expressed relative to the chemical potential of the two reservoirs, μ_{α} , and the barrier is given by

$$V(x) = \begin{cases} \Phi_{\rm m} & 0 < x < d \\ 0 & x < 0 \lor x > d \end{cases}$$
 (2.16)

The wavefunctions $\psi(x)$ that describe the states of the system satisfy the time-independent Schrödinger equation

$$E\psi(x) = \left(-\frac{\hbar^2}{2m_e} \frac{d^2}{dx^2} + V(x)\right) \psi(x). \tag{2.17}$$

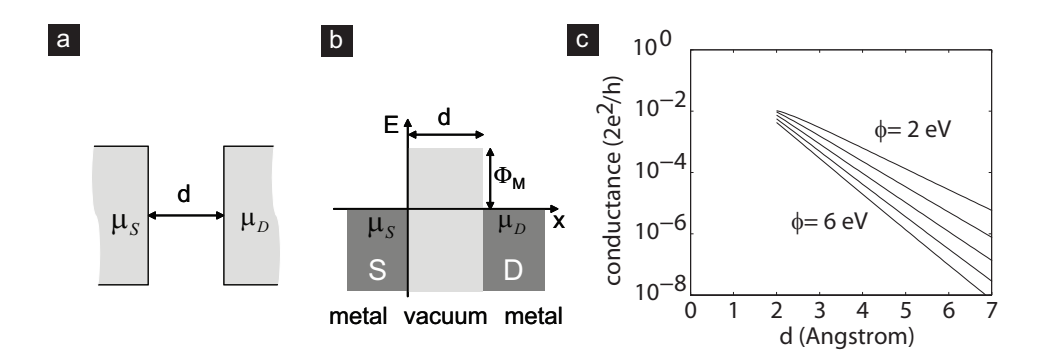


FIGURE 2.4: (a) Schematic of a tunnel junction. (b) Sketch of the simplified rectangular barrier that can be used to calculate the transmission in tunneling. (c) Plot of the low-bias conductance as a function of electrode distance and work function according to the Simmons model (see text). The calculation was carried out for $V_b=10~{\rm mV}$ and an electrode area of πd_{Au-Au}^2 , where $d_{Au-Au}=2.6~{\rm \AA}$.

Incoming electrons on the left of the potential barrier scatter into the states

$$\psi(x) = \begin{cases} A_{+} \exp(ikx) + A_{-} \exp(-ikx) & x < 0 \\ B_{+} \exp(k'x) + B_{-} \exp(-k'x) & 0 < x < d \\ C_{+} \exp(ikx) & x > d \end{cases}$$
 (2.18)

with the wavevectors

$$k = \sqrt{\frac{2m_e E}{\hbar^2}}, \quad k' = \sqrt{\frac{2m_e (\Phi_m - E)}{\hbar^2}}.$$
 (2.19)

The solution relevant for tunneling transport is the transmitted wavefunction at the right side of the barrier. After satisfying the boundary conditions of continuous ψ and $d\psi/dx$, one finds that the transmission coefficient is given by

$$T(E) = \left| \frac{C_+}{A_+} \right|^2 \propto \exp\left(\frac{-2d}{\hbar} \sqrt{2m_e \left(\Phi_m - E \right)} \right). \tag{2.20}$$

The distance dependence of the transmission in Equation 2.20 provides an important estimate for the tunneling conductance of a point contact. For small bias voltages with $|eV_b| << \Phi_m$,

$$G(d) \propto \exp\left(-\frac{\sqrt{8m_e\Phi_m}}{\hbar}d\right)$$
 (2.21)

It is important to note that the shape and the height of the barrier can be substantially modified in atomic-scale contacts. The geometry of the electrodes [10], adsorbed gas molecules [11], and small electrode distances [12] may all influence the shape and the

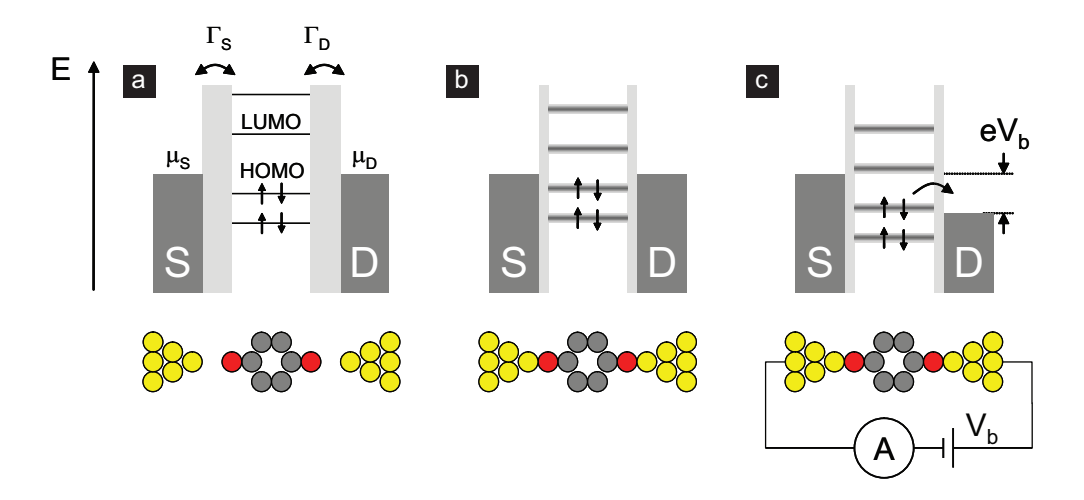


FIGURE 2.5: Energy diagrams of a molecular junction. The equilibrium situation is depicted in (a) for weak electronic coupling, and (b) for stronger electronic coupling. (c) The energy diagram at an applied bias of V_b .

height of the tunneling barrier. Furthermore, Equation 2.21 is only valid at small bias voltages.

An analytical formula for the tunneling current across an arbitrary barrier at finite bias voltages has been derived by Simmons [13]. For a rectangular barrier and $|eV_b| < \Phi_m$ it yields a current density of

$$J = \frac{e}{4\pi^2 \hbar d^2} \begin{bmatrix} \left(\Phi_m - \frac{eV_b}{2} \right) \exp\left(-\frac{2d}{\hbar} \sqrt{2m_e \left(\Phi_m - \frac{eV_b}{2} \right)} \right) \\ -\left(\Phi_m + \frac{eV_b}{2} \right) \exp\left(-\frac{2d}{\hbar} \sqrt{2m_e \left(\Phi_m + \frac{eV_b}{2} \right)} \right) \end{bmatrix}. \tag{2.22}$$

Note that for small bias voltages V_b , the characteristic exponential dependence of the conductance on the electrode distance as in Equation 2.21 is recovered.

In break junctions with atomically sharp electrodes the area of the tunneling contact is usually ill-defined, and a straightforward modeling with Equation 2.22 is not possible. However, it still yields a good estimate of the tunneling conductance as demonstrated in Figure 2.4c. The graph presents the low-bias conductance according to Equation 2.22 for an area corresponding to the diameter of a single gold atom. In the limit of $d \to 0$, i.e., for a closed quantum point contact, the approximate result $G \to G_0$ is obtained.

2.2 Transport across single molecules

In a first approximation, a molecule that is contacted by two metal electrodes may be modeled as a set of energy levels between two electron reservoirs (see Figure 2.5). Charge transport across such a junction is governed by quantum mechanics, since its dimensions are

typically on the order of the Fermi wavelength λ_F . The microscopic details of the transport are determined by four characteristic energy scales. After a discussion of these energy scales, the most important molecular transport regimes will be presented. The following discussion is largely based on References [14–16], which give a broad introduction to molecular transport.

2.2.1 ENERGY SCALES OF SINGLE-MOLECULE JUNCTIONS

The first energy scale of a molecular junction is a direct consequence of the nanometer size of the system. The spatial confinement of the electronic states on the molecule leads to the formation of discrete energy levels with a characteristic spacing Δ that may be estimated from the particle-in-a-box model (see Equation 2.8):

$$\Delta \approx \frac{\hbar^2}{2m_e} \left(\frac{\pi}{L_a}\right)^2. \tag{2.23}$$

For a cube with side lengths of 1 nm the model yields a level spacing of about 0.4 eV. In contrast to a simple quantum box, a molecule possesses a potential landscape that influences its electron distribution. The interactions of the nuclei and the charges of the electrons lead to the formation of molecular orbitals with varying energy spacing, which are represented by the electronic levels in Figure 2.5a.

Two orbitals are of special importance for molecular charge transport, the highest occupied molecular orbital (HOMO) and the lowest unoccupied molecular orbital (LUMO). The HOMO and the LUMO of the isolated molecule can be probed by analyses of the ionization energy and the electron affinity, respectively, and their gap can be estimated from UV/vis absorption spectroscopy. However, the energies of the electronic levels in molecular junctions may differ from the orbital energies of the isolated molecule. Charge transfer can shift the energies of the HOMO or the LUMO [17], and image charges on the electrodes may lead to a reduction of the level spacing by as much as one order of magnitude [18]. Hence, the level spacing and alignment in a single-molecule junction are an intrinsic property of the entire structure rather than the molecule alone.

The HOMO and the LUMO in a single-molecule junction are, by definition, located below and above the Fermi energy of the electrodes, respectively. If one of these orbitals is sufficiently broadened (see Section 2.2.2), it can mediate charge transport at low bias voltages. The character of the orbital that is involved in transport determines the conductive properties of the molecule. In conjugated molecules, which are often referred to as molecular wires [19], a highly delocalized π -orbital is formed by overlapping p-orbitals of the atoms in the backbone. It allows for efficient charge transfer along the molecule and high intramolecular conductances. In the molecular structure, π -conjugation is represented by alternating single and double bonds (see Figure 1.1). Chains of single bonds correspond to localized σ -bonds, which form the basis of more insulating aliphatic molecular species. The work associated with adding an electron to an object as small as a single molecule represents the second energy scale of a molecular junction. This so-called charging energy is given by

$$E_C = \frac{e^2}{2C}, (2.24)$$

where C is the total capacitance of the molecule to its environment. In a two-terminal geometry, $C = C_S + C_D$, the sum of the capacitances between the molecule and the source and the drain electrodes. An upper limit of the charging energy can be calculated from the self-capacitance of a metallic sphere with radius r, which is given by $C = 4\pi\epsilon_0 r$. For a diameter of 1 nm, similar to the dimensions of a molecule, a self-capacitance of about $5 \cdot 10^{-20}$ F and a charging energy of about 1.4 eV can be derived. The charging energy scales as 1/r and hence decreases with increasing device dimensions.

It is important to note that transport measurements on single-molecule junctions typically probe a convolution of the charging energy and the level spacing. The capacitances to the electrodes can depend on the molecular level, which leads to a level-dependent charging energy. In single-molecule spectroscopy, one therefore often refers to the addition energy $E_{add} \equiv 2E_C + \Delta$ (see Section 2.2.4 for details).

The third important energy scale is given by the electronic coupling of the molecule to the electrodes. Electron transfer between the levels of the molecule and the electrodes occurs via tunneling. In Figure 2.5a, this is indicated by two rectangular barriers. The coupling energies may be related to two tunneling time constants τ_{α} via

$$\Gamma_{\alpha} = \frac{\hbar}{\tau_{\alpha}},\tag{2.25}$$

where $\alpha = S, D$ refer to the couplings to the source and the drain electrode, respectively. The total coupling $\Gamma = \Gamma_S + \Gamma_D$. The central role of the electronic coupling for the appropriate description of transport across molecular junctions will be discussed in more detail in the following section.

The temperature of the reservoirs determines the final energy scale, the thermal energy

$$E_{th} = k_B T. (2.26)$$

At 300 K, $E_{th} \approx 25$ meV. A comparison with the typical charging energies and level spacings derived above shows that $E_{th} < \Delta$, E_C and suggests that quantization effects in molecular junctions may be observed at room temperature. If small-energy features in single molecule transport need to be resolved, however, it is favorable to work at liquid helium temperatures, where $E_{th} < 1$ meV. Moreover, low-temperature experiments ensure a high junction stability.

2.2.2 THE ROLE OF THE COUPLING TO THE LEADS

In most molecular junctions, chemical anchors such as thiol [20, 21] or amino [22] groups establish the bonds between the metal electrodes and the molecular core. They are of crucial importance for the electrical characteristics of the junction, since they determine both the electronic coupling Γ and the alignment of the molecular levels. In case of large coupling, transport occurs via coherent tunneling, whereas low coupling favors sequential tunneling. In the following, we will qualitatively discuss the influence of the coupling on the molecular levels before presenting these two important transport regimes.

Figure 2.5a presents a schematic of a molecular junction with small electronic coupling $(\Gamma \ll E_C, \Delta)$. Here, the density of states on the molecule is given by a series of discrete

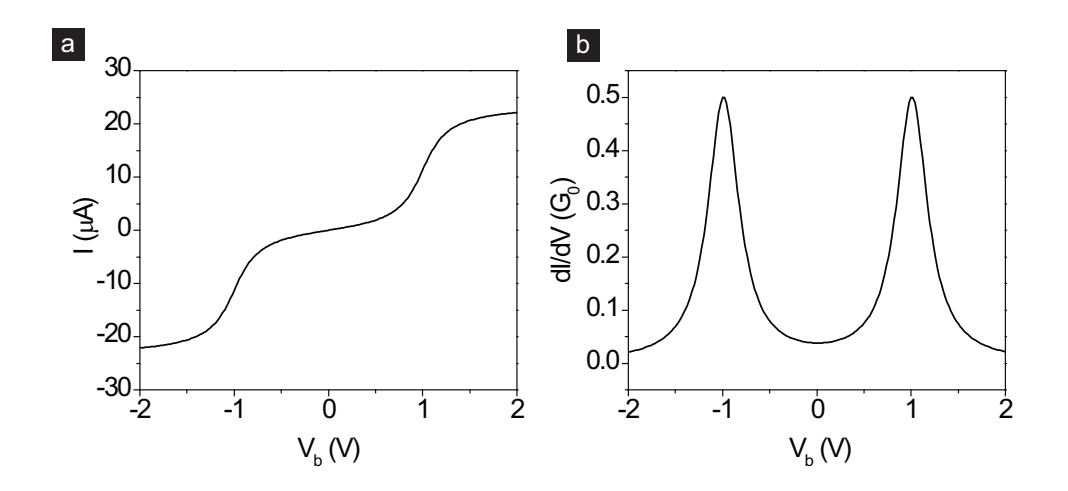


FIGURE 2.6: The transport characteristics across a broadened electronic level in the coherent tunneling regime according to Equation 2.29. In the calculation, $\epsilon = 0.5$ eV, $\Gamma/2 = \Gamma_S = \Gamma_D = 0.1$ eV, and T = 4.2 K. Charging effects have been neglected. (a) The current-voltage characteristics display a characteristic step pattern. (b) The differential conductance plot shows two peaks, which are separated by a conductance gap of $4\epsilon/\epsilon$.

levels. The small coupling leads to large electron residence times and a restriction of the total charge on the molecule to integer multiples of -e. If there is not enough energy in the system to compensate for the addition energy E_{add} the junction is in the so-called Coulomb blockade regime. Only as the bias voltage (and hence the energy) is increased, the next charge state becomes accessible and transport across the molecule may occur via sequential tunneling. It can be modeled within a rate equation approach, which will be presented in more detail in Section 2.2.4.

In the regime of intermediate coupling, where $\Gamma \approx E_C$, Δ , higher-order processes such as elastic cotunnneling and the Kondo effect become appreciable (see Section 2.2.5).

For large electronic coupling and $\Gamma > E_C, \Delta$, electrons may frequently tunnel on and off the molecule. The continuous electron exchange with the reservoirs leads to a fractional charging of the molecule and a shift of the energy level involved in transport. Furthermore, the hybridization with the states on the reservoirs causes a level broadening. This is schematically represented in Figure 2.5b. A prominent example of very large coupling is given by the hydrogen molecule, which exhibits a conductance of 1 G_0 when contacted by platinum leads [23]. A strong hybridization with electronic states on the platinum electrodes leads to the alignment of a broad molecular level with the chemical potential and a fully transparent conductance channel. Transport in the regime of large coupling occurs via coherent elastic or inelastic tunneling (see Section 2.2.3).

2.2.3 COHERENT TUNNELING

Transport across a strongly coupled single molecule can generally be described in the framework of the scattering formalism introduced in Section 2.1.5. The current then fol-

lows from

$$I = g_s \frac{e}{h} \int_{-\infty}^{\infty} T(E) \left(f(E, \mu_S) - f(E, \mu_D) \right) dE, \tag{2.27}$$

where T(E) is the energy-dependent transmission of the molecular junction. In first-principles calculations of molecular transport the transmission function may be derived from a combination of density-functional theory with a non-equilibrium Green's function formalism (NEGF) [24].

To come to an analytical approximation of the transmission function it is instructive to consider the tunneling rates between two reservoirs and a broadened molecular level with an equivalent density of states $D_{\varepsilon}(E)$ [15]. A schematic of this situation is presented in Figure 2.5c. Upon the application of a bias voltage V_b , the chemical potential of the drain electrode shifts by $-eV_b$ with respect to the source. For symmetric couplings, the position of the molecular level will move by half this value. The current from the reservoirs to the molecule can then be deduced from the tunneling rates as

$$I_{\alpha}(E,\mu_{\alpha}) = -g_{s}e\frac{dN}{dt}\left(E,\mu_{\alpha}\right) = -g_{s}\frac{e\Gamma_{\alpha}}{\hbar}\left(f(E,\mu_{\alpha}) - N\right),\tag{2.28}$$

where *N* is the number of electrons on the molecule. In the steady state where $I = I_D = -I_S$, the overall current across the junction is given by

$$I = g_{S} \frac{e}{\hbar} \int_{-\infty}^{\infty} D_{\varepsilon}(E) \frac{\Gamma_{S} \Gamma_{D}}{\Gamma_{S} + \Gamma_{D}} \left(f\left(E, \mu_{S}\right) - f\left(E, \mu_{D}\right) \right) dE. \tag{2.29}$$

A comparison of Equations 2.27 and 2.29 shows that the energy-dependent transmission can be related to the density of states via

$$T(E) = 2\pi \frac{\Gamma_S \Gamma_D}{\Gamma_S + \Gamma_D} D_{\epsilon}(E). \tag{2.30}$$

The density of states of a single broadened level can be described by a Lorentzian line-shape

$$D_{\epsilon}(E) = \frac{1}{2\pi} \frac{\Gamma}{(E - \epsilon)^2 + (\Gamma/2)^2},\tag{2.31}$$

where ϵ is the position of the level with respect to the chemical potential of the reservoirs in equilibrium. If the level is broadened by the electronic couplings to the leads, $\Gamma = \Gamma_S + \Gamma_D$. Note that in the limit of $\Gamma \to 0$ the Lorentzian lineshape converges to a Dirac delta, i.e., a discrete level.

From Equation 2.29 it is clear that there will only be a current if the density of states $D_{\epsilon}(E)$ is non-zero in the energy window where $f(E, \mu_S) \neq f(E, \mu_D)$. In a molecular junction in equilibrium, the Fermi energy of the electrodes is located within the HOMO-LUMO gap

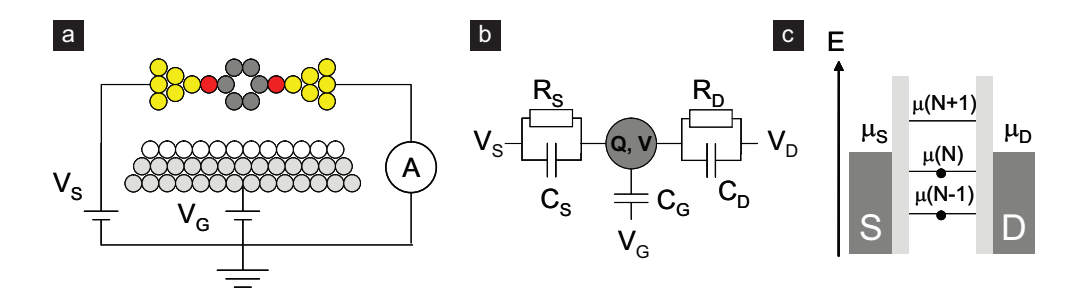


FIGURE 2.7: Schematics of a molecular junction with three terminals. (a) Cartoon representation of the device architecture. (b) Equivalent circuit in the constant interaction model. (c) Energy diagram of the junction. The chemical potential $\mu(N)$ corresponds to the $N-1 \to N$ transition.

of the molecule. At low bias voltages and in the weak to intermediate coupling regime the first accessible molecular level is typically located far from the chemical potential of the leads, so that I_{SD} is small. Transport in this regime is usually referred to as off-resonant. Only as the first molecular level enters the energy window between μ_S and μ_D does resonant tunneling transport become possible, and the current increases rapidly.

Figure 2.6 presents plots of the current and the differential conductance dI/dV across a Lorentzian-broadened single level. For symmetric couplings $\Gamma_S = \Gamma_D$, the differential conductance shows two peaks of equal height at $V_b = \pm 2\varepsilon/e$, corresponding to resonant transport. The characteristic conductance gap between the peaks marks the regime of offresonant transport. Asymmetry in the Γ_α can lead to a difference in both the peak height and position.

It is important to note that charging effects may change the shape of the IV characteristics considerably [14]. In the above derivation, we have assumed that $E_C=0$. Fractional charging, however, leads to a potential on the molecule that shifts $D_{\varepsilon}(E)$ in Equation 2.29. This level shift needs to be included in a self-consistent calculation of the transfer rates in Equation 2.28, which is beyond the scope of this section. Details of the approach can be found in Reference [14]. Qualitatively speaking, charging effects lead to a pinning of the molecular level at either of the chemical potentials of the leads when the bias voltage is increased. This causes a highly broadened peak in the dI/dV spectrum.

2.2.4 COULOMB BLOCKADE AND SEQUENTIAL TUNNELING

If the couplings to the source and the drain electrodes are small $(\Gamma, k_BT << E_C)$, the total charge on the molecule is restricted to integer multiples of -e. This requirement has important implications for charge transport across the device. At low bias voltages, there is generally not enough energy to change the charge state of the molecule and the current is suppressed; the junction is in Coulomb blockade. The only exception to this rule is the case of charge state degeneracy, which will be discussed later. At sufficiently large bias voltages, where $|eV_b| > 2E_C + \Delta$, the blockade can be lifted and electrons may tunnel on and off the molecule sequentially.

To date, there have been a number of studies of gated single-molecule junctions in the

Coulomb blockade regime [25]. Figure 2.7a presents a schematic of a single-molecule junction in a three-terminal configuration. In Coulomb blockade, its transport characteristics can be analyzed by drawing on the physics of single electron transistors (SETs) [26, 27] and semiconductor quantum dots [28]. In these systems, a chargeable island is separated from two electrodes by tunneling barriers of low transparency. The potential on the island can be shifted by applying a voltage to a third, adjacent gate electrode. Figure 2.7b presents the equivalent circuit of a gateable quantum dot.

Transport through such a quantum dot can be described within the constant interaction model, where it is assumed that the capacitances to the electrodes are independent of the charge state. Furthermore, in the orthodox theory of single-electron devices, the electrodes are treated as electron reservoirs, the time scales of the tunneling through either of the barriers are assumed to be much shorter than any other time scale of the system, and coherent transport processes are ignored [26]. Effectively, this results in the requirement that the tunneling resistances R_S , $R_D >> 1/G_0$.

The total induced charge on a molecular quantum dot is determined by its potential V, the potentials V_{α} on the three electrodes, and the capacitances C_{α} :

$$Q = C_S(V - V_S) + C_D(V - V_D) + C_G(V - V_G).$$
(2.32)

The potential on the molecule then becomes

$$V = \frac{Q}{C} + V_S \frac{C_S}{C} + V_D \frac{C_D}{C} + V_G \frac{C_G}{C},$$
 (2.33)

where $C = C_S + C_D + C_G$ is the total capacitance of the device. In the Coulomb blockade regime, the charge on the molecule is limited to integer multiples of the electron charge, that is, Q = -Ne. The total energy of the system can then be written as the sum of the electrostatic work of adding N electrons to the molecule and the single-particle energies E_n of all occupied molecular levels:

$$U(N) = \int_{0}^{-Ne} V dq + \sum_{n=1}^{N} E_n$$
 (2.34)

$$= \frac{(Ne)^2}{2C} - Ne\left(\frac{V_SC_S + V_DC_D + V_GC_G}{C}\right) + \sum_{n=1}^{N} E_n$$
 (2.35)

In a single-particle picture, the chemical potential of the N^{th} electron on the molecule can be determined from a difference in total energies,

$$\mu(N) = U(N) - U(N-1) \tag{2.36}$$

$$= \frac{(2N-1)e^2}{2C} - e\left(\frac{V_SC_S + V_DC_D + V_GC_G}{C}\right) + E_N. \tag{2.37}$$

In modeling the Coulomb blockade regime, the chemical potentials of consecutively added electrons yield the level structure of the island (see Figure 2.7c). Only when a level is

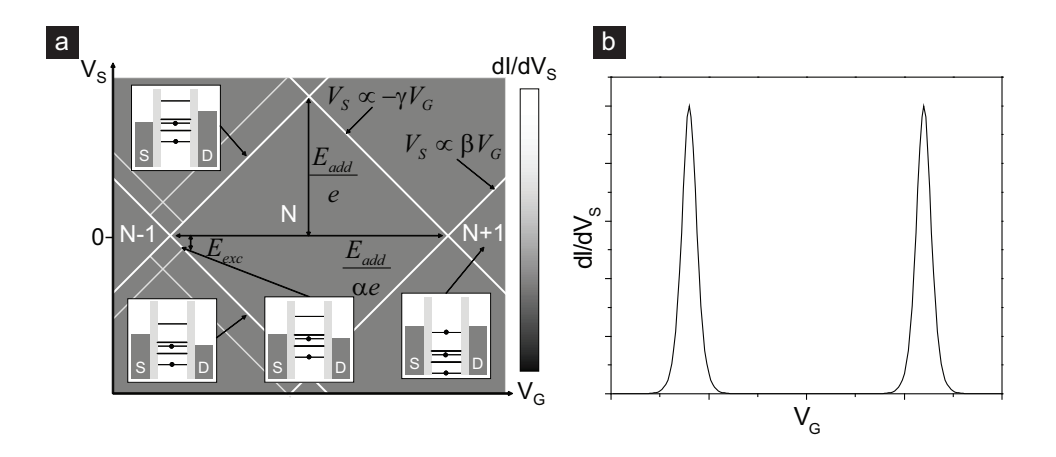


FIGURE 2.8: Schematics of a three-terminal measurement of a molecular junction in the Coulomb blockade regime. (a) Two-dimensional plot of the differential conductance in a so-called stability diagram. The plot presents the signatures of single-electron charging and of two excitations of the island (see text). The insets present the energy landscape of the junction for selected combinations of gate and bias voltage. (b) Low-bias differential conductance as a function of gate voltage. The peaks correspond to transitions between consecutive charge states.

located within the energy window formed by the chemical potentials of the source and drain electrodes can electrons tunnel on and off the molecule sequentially and can a current be measured. At zero bias, the gate voltage can be used to align the level with the chemical potentials of the leads, such that $\mu((N+1), V_G) = \mu_S = \mu_D$, and lift the blockade; at this so-called degeneracy point, $U((N+1), V_G) = U(N, V_G)$. The difference between the gate voltages of two successive degeneracy points is given by

$$\Delta V_G = \frac{C}{eC_G} \left(\frac{e^2}{C} + E_{N+1} - E_N \right) = \frac{1}{e\alpha} E_{add}. \tag{2.38}$$

Here, we have defined $E_{add} \equiv 2E_C + E_{N+1} - E_N$ as the addition energy of the $(N+1)^{\text{th}}$ electron and $\alpha \equiv C_G/C$ as the gate coupling. Notably, the addition energy contains contributions from both the charging energy and the level spacing of the molecule. This composition differs from transport through nanometer-sized metal islands, where the electronic level spacing is typically negligible [29].

As can be seen from Equation 2.37, the chemical potential on the molecule may also be shifted by the source and the drain voltages. In order to come to a theoretical description of a three-terminal measurement, it is useful to refer to the schematic representation in Figure 2.7c and follow the level $\mu(N)$ as the voltages V_D , V_S , and V_G are varied. As explained earlier, the Coulomb blockade is lifted once the level enters the bias window given by the source and the drain electrodes. The two conditions for the onset of sequential tunneling can then be derived from the alignment of the level of the molecule with the chemical potential of either the source or the drain electrode. In our model, all voltages

are referenced to the drain, i.e., $V_D = 0$, and we find that for

$$\mu(N) = \mu_S$$
 : $V_S = \frac{C_G}{C_G + C_D} V_G - \frac{(2N-1)e}{2(C_G + C_D)} - \frac{E_N C}{e(C_G + C_D)}$, and (2.39)

$$\mu(N) = \mu_D$$
 : $V_S = -\frac{C_G}{C_S}V_G + \frac{(2N-1)e}{2C_S} + \frac{E_NC}{eC_S}$. (2.40)

Figure 2.8a presents a schematic of the differential conductance characteristics of a three-terminal junction in the Coulomb blockade regime. The diamond-shaped areas centered about $V_s=0$ correspond to well-defined charge states of the molecule. The borders of these so-called charging diamonds mark the transition to sequential tunneling transport. The slopes of the diamond edges are a direct result of Equations 2.39 and 2.40; on the diamond edge with a positive slope of $\beta \equiv C_G/(C_G+C_D)$ the level $\mu(N)$ is aligned with the chemical potential of the source. Conversely, the diamond edge with negative slope $-\gamma \equiv -C_G/C_S$ marks the alignment with the drain. The ratios of the capacitances in a weakly coupled molecular junction can be obtained directly from a three-terminal measurement. They are given by

$$\frac{1}{\alpha} = \frac{1}{\beta} + \frac{1}{\gamma}.\tag{2.41}$$

An expression for the junction current in the regime of single-electron tunneling can be derived from a set of rate equations for the occupation probability of the molecular state. When the molecule is in the $(N-1)^{\text{th}}$ charge state, the transition to the N^{th} charge state requires the tunneling of a single electron from the reservoirs to the molecule. Conversely, the tunneling of an electron to one of the reservoirs causes the transition $N \to N-1$. The electron is transferred with a finite probability that depends on both the tunnel coupling and the availability of states in the reservoirs. The master equations for the N^{th} state are,

$$\frac{dP_0}{dt} = -P_0 \left(\frac{1}{\tau_S} f_S + \frac{1}{\tau_D} f_D \right) + P_1 \left(\frac{1}{\tau_S} \left(1 - f_S \right) + \frac{1}{\tau_D} \left(1 - f_D \right) \right) \tag{2.42}$$

$$\frac{dP_1}{dt} = P_0 \left(\frac{1}{\tau_S} f_S + \frac{1}{\tau_D} f_D \right) - P_1 \left(\frac{1}{\tau_S} \left(1 - f_S \right) + \frac{1}{\tau_D} \left(1 - f_D \right) \right), \tag{2.43}$$

where P_1 denotes the probability of the molecule being in the N^{th} state, and P_0 is the probability of being in the $(N-1)^{\text{th}}$ state. The steady state current across one level can be obtained from these two equations as

$$I = \frac{e}{\hbar} \frac{\Gamma_S \Gamma_D}{\Gamma_S + \Gamma_D}.$$
 (2.44)

Figure 2.8b presents a schematic of the low-bias conductance in the Coulomb blockade regime as a function of gate bias. The two peaks in the plot correspond to the alignment of an electronic level with the Fermi energy of the electrodes. In an experiment, they give an indication of the presence of a nanoscale island in the electrode gap [25].

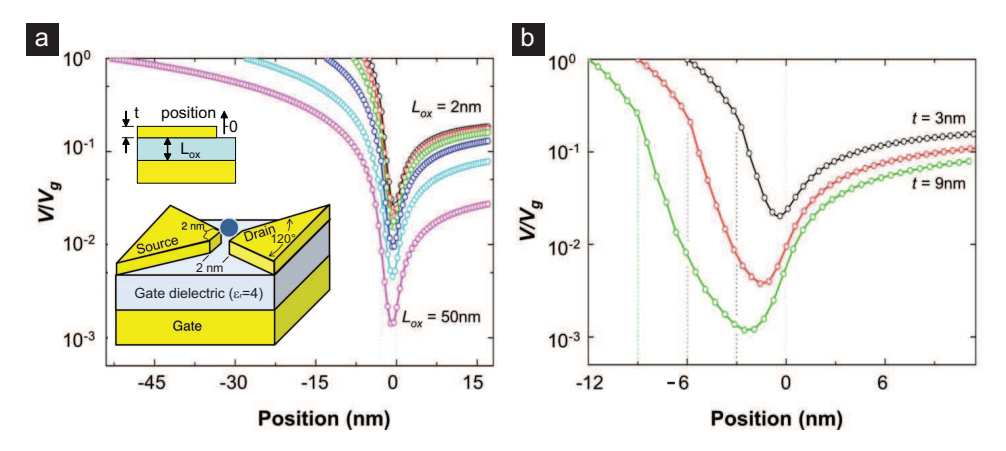


FIGURE 2.9: Calculations of the gate coupling for grounded tapered electrodes (Reproduced with permission from Reference [30]. ©2009 by the American Physical Society). (a) Dependence of the effective potential on the vertical position in the junction for different gate dielectric thicknesses (2, 3, 5, 10, 25, and 50 nm) and an electrode thickness of 3 nm. The inset shows a schematic of the device architecture used in the calculations. (b) Plot of the effective gate potential for three different electrode thicknesses (3, 6, and 9 nm) and a gate dielectric thickness of 3 nm. The dotted vertical lines mark the respective positions of the dielectric surface.

The importance of the gate coupling

The gate coupling α plays a crucial role in three-terminal measurements on molecular junctions. If it is too small, it may be impossible to access more than one charge state and extract the addition energy (see Equation 2.38). Hence, before designing a device architecture for three-terminal measurements, it is useful to investigate the influence of different geometrical parameters on the gate coupling.

In a three-terminal junction, the gate voltage induces an electric field at the position of the molecule, which results in a level shift of $\Delta \mu(V_G) = -(C_G/C)eV_G = -\alpha eV_G$. Experimentally, the gate coupling α can be deduced from the width and height of a charging diamond in the stability diagram (see Figure 2.8a) or from the two slopes of the diamond edges. Theoretically, the coupling is calculated from the electrostatics of the device using Poisson's equation [30, 31]. Such calculations not only show that the electric field decays as a function of the distance from the gate; moreover, it is screened in the vicinity of the source and the drain electrode. In a recent study, Datta et al. have simulated the electrostatic field in numerous device architectures for three-terminal measurements [30]. They found that the geometry of the electrodes and the insulator have a large influence on the gate coupling, whereas it hardly depends on the dielectric constant. Figure 2.9 presents two results from Reference [30] for tapered electrodes with a separation of 2 nm, comparable to the structure of a single-molecule junction. The gate coupling is at a minimum near the top of the electrodes and increases in the vicinity of the gate dielectric. When decreasing the thickness of the gate dielectric, L_{ox} , from 50 nm to 2 nm, the gate coupling at the bottom of the electrode tips increases from 10^{-2} to about 10^{-1} . This range is in good agreement with experimental studies, which yielded values of up to $\alpha = 7 \cdot 10^{-3}$ for a vacuum gap of 40 nm thickness [32] and $\alpha=0.2$ for a native aluminum oxide dielectric ($L_{ox}=5$ nm) [33]. Figure 2.9b presents the dependence of the gate coupling on the thickness of the source and the drain electrode. With increasing thickness, a large reduction in coupling can be observed. In experiments, the position of the molecule in the junction and the atomic geometry of the electrode tips may further influence the gate coupling. In order to maximize the gate effect in a three-terminal device, it is therefore beneficial to employ tapered and thin source-drain electrodes in close vicinity to the gate.

2.2.5 SPECTROSCOPIC FEATURES IN MOLECULAR JUNCTIONS

Vibrational excitations

The spatial conformation of an organic molecule is not fixed but exhibits degrees of freedom in both bond lengths and bond angles. At low energies, these allow for vibrations of the nuclei in so-called normal modes, which provide a fingerprint of the chemical structure. Such a vibrational mode, or vibron, can be described within the framework of a harmonic oscillator with a total energy of

$$E_{exc} = \hbar \omega_{exc} \left(n + \frac{1}{2} \right), \tag{2.45}$$

where n is the quantum number of the mode and ω_{exc} is its characteristic frequency. In bulk analyses of organic molecules, vibrational modes may be probed by Raman or infrared spectroscopy. The choice of the spectroscopic method depends on the nature of the vibration; infrared-active vibrations change the dipole moment of the molecule, whereas Raman-active vibrations change its polarizability.

Due to the intimate links between the electronic and atomic structure of a molecule, vibrational modes can also couple to charge transport processes. The strength of this interaction is given by the electron-vibron coupling λ . Computationally, the strength of the interaction can be obtained from a comparison of the wavefunctions in the ground state and the vibrationally excited state of the molecule. The degree of overlap yields the Franck-Condon factors, from which the electron-vibron coupling can be derived [34].

In a single-molecule junction, the electron-vibron coupling opens up an additional pathway for transport. In the coherent tunneling regime, this leads to a change in the transmission and a step in the differential conductance dI/dV at $V_b = \hbar \omega_{exc}$. The direction of the step depends on the transmission in the ground state [35, 36]; for a single conductance channel with $\tau > 0.5$, the transfer of energy from an electron to the vibrational mode leads to backscattering and a step down in dI/dV. For $\tau < 0.5$, the scattering of the conduction electrons with the vibrational mode increases the transmission and leads to a step up in dI/dV. This effect has been exploited in inelastic electron tunneling spectroscopy (IETS) to probe the vibrational modes of single molecules [37, 38].

In the regime of single-electron tunneling, the charge on the molecule may only change by one electron at a time. Here, the molecular vibration generally increases the probability of accessing a neighboring charge states and forms an additional resonance at

$$\mu^*(N) = \mu(N) + \hbar \omega_{exc}. \tag{2.46}$$

The spectroscopic signature of a vibrational mode is presented in Figure 2.8a. The additional pathway results in lines in the regions of single-electron tunneling that run parallel to the diamond edges. The energy $\hbar\omega_{exc}$ of the vibrational mode can be read off directly from the intersection of the excitation line with the diamond edge. Depending on the electron-phonon coupling and the relaxation time of the vibrational mode, higher harmonics may also be observed.

The Kondo resonance

In the regime of intermediate coupling, higher-order tunneling processes become appreciable [25]. In molecules with an unpaired spin ($S = \pm 1/2$), an antiferromagnetic coupling with the electrons in the leads can lead to the so-called Kondo effect, which is indicated by an enhancement of the conductance around zero bias [39–41].

A theory of the effect was first put forward by Kondo [42], after whom it is named. It was originally observed in bulk metals, where the inclusion of ferromagnetic impurities leads to a conductance minimum at low temperatures [43]. In a simple picture, the antiferromagnetic interaction of an unpaired spin with the surrounding electron bath leads to dynamic screening processes. In bulk metals, the cloud of screening electrons may act as a scattering center for conduction electrons. In quantum dots, however, the increased density of states around E_F causes an enhancement of the zero-bias conductance [44].

The energy scale for the formation of the screening cloud is given by the Kondo temperature T_K . For an impurity level at an energy $\epsilon >> \Gamma$ from the Fermi energy of the leads, the Kondo temperature is given by

$$k_B T_K = \frac{\sqrt{2\Gamma E_C}}{2} \exp\left[\frac{\pi\epsilon \left(\epsilon + 2E_C\right)}{2\Gamma E_C}\right].$$
 (2.47)

Due to its dependence on the charging energy and the coupling, the Kondo temperature varies between different nanoscale systems. In molecules it is typically on the order of tens of Kelvins.

In the differential conductance of the system, the Kondo effect leads to a Lorentzian peak at zero bias. Its full width at half maximum (FWHM) is proportional to the Kondo temperature, as $FWHM \approx 2k_BT_K/e$. The height of the zero-bias peak in the differential conductance is given by

$$G_{max}(T) = G_0 \frac{4\Gamma_S \Gamma_D}{(\Gamma_S + \Gamma_D)^2} \left(1 + 2^{\frac{1}{s} - 1} \frac{T^2}{T_K^2} \right)^{-s} + G_{el}, \tag{2.48}$$

where $s \approx 0.22$ for S = 1/2. Here, G_{el} accounts for a constant background due to elastic tunneling.

REFERENCES

[1] S. Datta, *Electronic Transport in Mesoscopic Systems* (Cambridge University Press, 1995).

REFERENCES 39

[2] N. Agraït, A. L. Yeyati, and J. M. van Ruitenbeek, *Quantum properties of atomic-sized conductors*, Phys. Rept. **377**, 81 (2003).

- [3] C. Untiedt, G. Rubio Bollinger, S. Vieira, and N. Agraït, *Quantum interference in atomic-sized point contacts*, Phys. Rev. B **62**, 9962 (2000).
- [4] P. Drude, Zur Elektronentheorie der Metalle, Annalen der Physik 306, 566 (1900).
- [5] B. J. van Wees, H. van Houten, C. W. J. Beenakker, J. G. Williamson, L. P. Kouwenhoven, D. van der Marel, and C. T. Foxon, *Quantized conductance of point contacts in a two-dimensional electron gas*, Phys. Rev. Lett. **60**, 848 (1988).
- [6] E. Scheer, N. Agraït, J. C. Cuevas, A. L. Yeyati, B. Ludoph, A. Martín-Rodero, G. R. Bollinger, J. M. van Ruitenbeek, and C. Urbina, *The signature of chemical valence in the electrical conduction through a single-atom contact*, Nature **394**, 154 (1998).
- [7] S. Frank, P. Poncharal, Z. L. Wang, and W. A. de Heer, *Carbon Nanotube Quantum Resistors*, Science **280**, 1744 (1998).
- [8] R. Landauer, Spatial Variation of Currents and Fields Due to Localized Scatterers in Metallic Conduction, IBM J. Res. Dev. 1, 223 (1957).
- [9] M. Büttiker, Scattering theory of current and intensity noise correlations in conductors and wave guides, Phys. Rev. B **46**, 12485 (1992).
- [10] R. J. P. Keijsers, J. Voets, O. I. Shklyarevskii, and H. van Kempen, *Electrode geometry in-fluencing the tunnel resistance in a mechanically controllable break junction*, Physica B 218, 283 (1996).
- [11] O. Y. Kolesnychenko, O. I. Shklyarevskii, and H. van Kempen, Giant Influence of Adsorbed Helium on Field Emission Resonance Measurements, Phys. Rev. Lett. 83, 2242 (1999).
- [12] K. Hansen and M. Brandbyge, *Current-voltage relation for thin tunnel barriers: Parabolic barrier model*, J. Appl. Phys. **95**, 3582 (2004).
- [13] J. G. Simmons, Generalized Formula for the Electric Tunnel Effect between Similar Electrodes Separated by a Thin Insulating Film, J. Appl. Phys. **34**, 1793 (1963).
- [14] M. Paulsson, F. Zahid, and S. Datta, *Resistance of a Molecule* (CRC Press, 2003), chap. 12.
- [15] S. Datta, Electrical resistance: an atomistic view, Nanotechnology 15, S433 (2004).
- [16] J. M. Thijssen and H. S. J. van der Zant, *Charge transport and single-electron effects in nanoscale systems*, phys. stat. sol. b **245**, 1455 (2008).
- [17] R. Stadler and K. W. Jacobsen, Fermi level alignment in molecular nanojunctions and its relation to charge transfer, Phys. Rev. B **74**, 161405 (2006).

- [18] K. Kaasbjerg and K. Flensberg, *Strong Polarization-Induced Reduction of Addition Energies in Single-Molecule Nanojunctions*, Nano Lett. **8**, 3809 (2008).
- [19] D. K. James and J. M. Tour, *Molecular Wires*, Top. Curr. Chem. 257, 33 (2005).
- [20] J. C. Love, L. A. Estroff, J. K. Kriebel, R. G. Nuzzo, and G. M. Whitesides, *Self-Assembled Monolayers of Thiolates on Metals as a Form of Nanotechnology*, Chem. Rev. **105**, 1103 (2005).
- [21] H. B. Akkerman and B. de Boer, *Electrical conduction through single molecules and self-assembled monolayers*, J. Phys.: Condens. Matter **20**, 013001 (2008).
- [22] M. S. Hybertsen, L. Venkataraman, J. E. Klare, A. C. Whalley, M. L. Steigerwald, and C. Nuckolls, *Amine-linked single-molecule circuits: systematic trends across molecular families*, J. Phys.: Condens. Matter 20, 374115 (2008).
- [23] R. H. M. Smit, Y. Noat, C. Untiedt, N. D. Lang, M. C. van Hemert, and J. M. van Ruitenbeek, *Measurement of the conductance of a hydrogen molecule*, Nature **419**, 906 (2002).
- [24] M. Brandbyge, J.-L. Mozos, P. Ordejón, J. Taylor, and K. Stokbro, *Density-functional method for nonequilibrium electron transport*, Phys. Rev. B 65, 165401 (2002).
- [25] E. A. Osorio, T. Bjørnholm, J.-M. Lehn, M. Ruben, and H. S. J. van der Zant, Single-molecule transport in three-terminal devices, J. Phys.: Condens. Matter 20, 374121 (2008).
- [26] K. K. Likharev, Single-Electron Devices and Their Applications, Proc. IEEE 87, 606 (1999).
- [27] T. A. Fulton and G. J. Dolan, *Observation of single-electron charging effects in small tunnel junctions*, Phys. Rev. Lett. **59**, 109 (1987).
- [28] U. Meirav, M. A. Kastner, and S. J. Wind, *Single-electron charging and periodic conductance resonances in GaAs nanostructures*, Phys. Rev. Lett. **65**, 771 (1990).
- [29] F. Kuemmeth, K. I. Bolotin, S.-F. Shi, and D. C. Ralph, Measurement of Discrete Energy-Level Spectra in Individual Chemically Synthesized Gold Nanoparticles, Nano Lett. 8, 4506 (2008).
- [30] S. S. Datta, D. R. Strachan, and A. T. C. Johnson, Gate coupling to nanoscale electronics, Phys. Rev. B 79, 205404 (2009).
- [31] H. S. J. van der Zant, Y.-V. Kervennic, M. Poot, K. O'Neill, Z. de Groot, J. M. Thijssen, H. B. Heersche, N. Stuhr-Hansen, T. Bjørnholm, D. Vanmaekelbergh, et al., *Molecular three-terminal devices: fabrication and measurements*, Faraday Discuss. **131**, 347 (2006).

REFERENCES 41

[32] A. R. Champagne, A. N. Pasupathy, and D. C. Ralph, *Mechanically Adjustable and Electrically Gated Single-Molecule Transistors*, Nano Lett. **5**, 305 (2005).

- [33] S. Kubatkin, A. Danilov, M. Hjort, J. Cornil, J.-L. Brédas, N. Stuhr-Hansen, P. Hedegård, and T. Bjørnholm, *Single-electron transistor of a single organic molecule with access to several redox states*, Nature **425**, 698 (2003).
- [34] S. Braig and K. Flensberg, *Vibrational sidebands and dissipative tunneling in molecular transistors*, Phys. Rev. B **68**, 205324 (2003).
- [35] M. Paulsson, T. Frederiksen, and M. Brandbyge, *Modeling inelastic phonon scattering in atomic- and molecular-wire junctions*, Phys. Rev. B **72**, 201101 (2005).
- [36] O. Tal, M. Krieger, B. Leerink, and J. M. van Ruitenbeek, Electron-Vibration Interaction in Single-Molecule Junctions: From Contact to Tunneling Regimes, Phys. Rev. Lett. 100, 196804 (2008).
- [37] J. Lambe and R. C. Jaklevic, *Molecular Vibration Spectra by Inelastic Electron Tunneling*, Phys. Rev. **165**, 821 (1968).
- [38] B. C. Stipe, M. A. Rezaei, and W. Ho, *Single-Molecule Vibrational Spectroscopy and Microscopy*, Science **280**, 1732 (1998).
- [39] W. Liang, M. P. Shores, M. Bockrath, J. R. Long, and H. Park, *Kondo resonance in a single-molecule transistor*, Nature **417**, 725 (2002).
- [40] J. Park, A. N. Pasupathy, J. I. Goldsmith, C. Chang, Y. Yaish, J. R. Petta, M. Rinkoski, J. P. Sethna, H. D. Abruna, P. L. McEuen, et al., *Coulomb blockade and the Kondo effect in single-atom transistors*, Nature **417**, 722 (2002).
- [41] J. J. Parks, A. R. Champagne, G. R. Hutchison, S. Flores-Torres, H. D. Abruña, and D. C. Ralph, *Tuning the Kondo Effect with a Mechanically Controllable Break Junction*, Phys. Rev. Lett. 99, 026601 (2007).
- [42] J. Kondo, *Resistance Minimum in Dilute Magnetic Alloys*, Prog. Theor. Phys. **32**, 37 (1964).
- [43] W. J. de Haas, J. de Boer, and G. J. van den Berg, *The electrical resistance of gold, copper and lead at low temperatures*, Physica 1, 1115 (1934).
- [44] L. Kouwenhoven and L. Glazman, *Revival of the Kondo effect*, Physics World pp. 33–38 (Jan 2001).

DESIGN AND CHARACTERIZATION OF THE MCBJ MEASUREMENT SYSTEM

This chapter presents the mechanically controllable break junction devices and the two cryogenic measurement setups that have been developed for this Thesis. The MCBJ devices and the setup mechanics have been optimized for both subangstrom control of the electrode distance and fast statistical measurements on single-molecule junctions. The devices possess a mechanical attenuation on the order of $5 \cdot 10^{-5}$ and are microfabricated in a batch process. The first measurement setup is based on a differential screw drive and can operate at actuation speeds of 2 μ m/s. In the second-generation measurement setup, a tuning of the MCBJ bending by up to 600 μ m/s is enabled by an amplified piezoceramic actuator. We present an overview of the characteristics of the measurement system and the implemented experimental techniques for studying single-molecule junctions.

This chapter will be part of a forthcoming publication.

3.1 MECHANICALLY CONTROLLABLE BREAK JUNCTIONS

3.1.1 MECHANICS OF TWO-TERMINAL MCBJS

In a mechanically controllable break junction the bending of a flexible substrate controls the distance between two partially suspended metal electrodes [1]. A schematic representation of a break junction device with its geometrical parameters is given in Figure 3.1.

The development of the MCBJ was based on an experiment by Moreland and Halsma, who exploited the difference in the bending radii of two sandwiched glass plates to control the tunneling current between two parallel plate electrodes [2]. Present mechanical break junction experiments employ a three-point bending setup, in which the rectangular MCBJ substrate is bent between two countersupports.

In the regime of linear elastic deformation, the bending profile of the substrate can be calculated from the Euler-Bernoulli equation,

$$\frac{\partial^2}{\partial x^2} \left(E I_{yy} \frac{\partial^2 z}{\partial x^2} \right) = 0, \tag{3.1}$$

where E is the Young's modulus and I_{yy} is the moment of inertia of the substrate's cross section. For a substrate with uniform E and I_{yy} , Equation 3.1 can be simplified to obtain

$$\frac{\partial^2 z}{\partial x^2} = -\frac{M_y(x)}{EI_{yy}},\tag{3.2}$$

where $M_y(x)$ is the position-dependent bending moment. The moment of inertia follows from the substrate width W_S and thickness H_S as $I_{yy} = W_S H_S^3/12$. For the MCBJ depicted in Figure 3.1, $M_y(x)$ can be calculated from the bending force $F_z = -F_B$, which is exerted at the center of the flexible substrate, as

$$M_{y}(x) = \frac{F_{B}}{2}x - H[x - L_{S}/2]\left(x - \frac{L_{S}}{2}\right)F_{B}.$$
(3.3)

Here, H[n] is the Heaviside step function, and x = 0 marks the position of the left countersupport. Integration of Equation 3.2 with the boundary conditions $z(0) = z(L_S) = 0$ then yields the deflection of the beam center,

$$w = -z(\frac{L_S}{2}) = \frac{F_B L_S^3}{4EW_S H_S^3}. (3.4)$$

While the neutral axis of the beam can be considered strain free, the bending moment results in expansive and compressive stress on the top and bottom surface of the beam, respectively. At $x = L_S/2$ this leads to the surface stress

$$\sigma_x = \frac{3F_B L_S}{2W_S H_S^2}. (3.5)$$

Due to the suspended length U of the electrodes, this stress is translated into a displacement of $d = U\sigma_x/E$. For uniform bending, the change in electrode distance can be

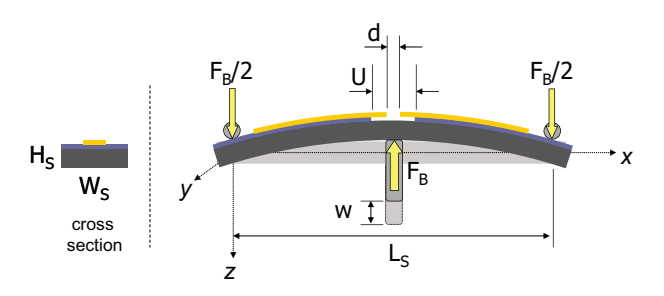


FIGURE 3.1: Schematic of a mechanically controllable break junction in a three-point bending setup.

related to the substrate deflection via the displacement ratio:

$$r = \frac{d}{w} = \frac{\sigma_x U}{Ew} = \frac{6H_S U}{L_S^2} \tag{3.6}$$

For break junctions based on notched metal wires the experimental displacement ratio is typically on the order of 10^{-3} to $10^{-2}[1,3]$. The success of the break junction architecture is due to this intrinsic mechanical attenuation. It guarantees precise control and high drift stability of the electrode spacing, which are important prerequisites for studying metal point contacts and single-molecule junctions. This stability can be enhanced further by using lithographic MCBJs [3], in which the suspended length is reduced by two orders of magnitude. Here, typical displacement ratios range from 10^{-6} to 10^{-4} [4–6]. Compared to Equation 3.6, the displacement ratio in lithographically fabricated MCBJs often displays an effective enhancement by a factor of $\xi = 2.8..4.3$ [5]. It has been attributed to the elastic properties of the polyimide layer on which the relatively rigid micrometer-sized metal electrodes are deposited (see Section 3.1.3). For MCBJs in a liquid cell setup, correction factors as large as 10 have been reported, a fact that might be due to the pressing of the substrate against the solvent reservoir [7].

3.1.2 DEVICE DESIGN

Before choosing a MCBJ geometry it is useful to explore the role of the device dimensions in the experimental performance. The design of any MCBJ device has to optimize three figures of merit: the static deflection that is necessary to initially break the suspended electrode bridge and create a metal point contact, the dynamic deflection required to cycle the contact between the fully opened and the fused state, and the maximum force required for bending. In a nutshell, the lithographic MCBJs for this Thesis have been designed to minimize both the bending force and the deflection required for breaking the source-drain electrode pair. This combination facilitates the design of the experimental setup through an extended choice of actuator mechanisms (see Section 3.2.2).

To start with, it is useful to compare the role of both the geometrical and the physical properties of a MCBJ device in its displacement ratio. Equation 3.6 defines the parameters that determine the mechanical attenuation and, therefore, the required dynamic and static ranges of bending; these are purely geometrical. In lithographic MCBJs, the length of

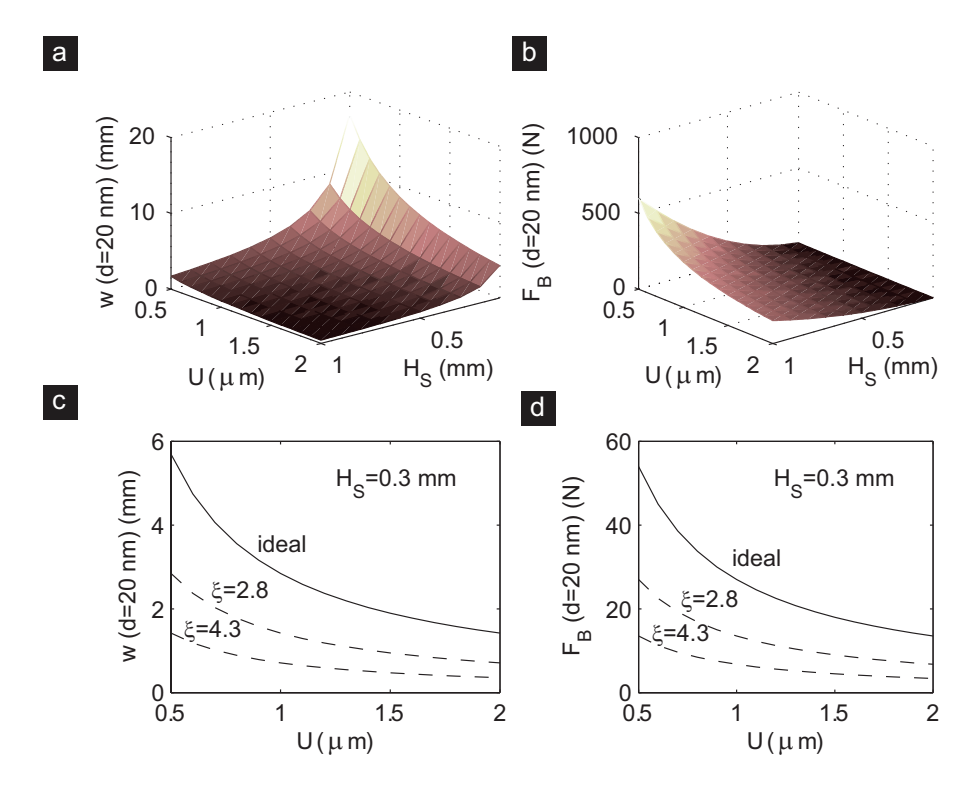


FIGURE 3.2: Results of the mechanical modeling for the MCBJ design in this Thesis (phosphor bronze substrates with $L_S=16$ mm, $W_S=6$ mm, E=120 GPa). The calculations were carried out for an electrode stretching of 20 nm, sufficient to form a gap to host a single molecule. (a) and (b) present the corresponding deflection and bending force as a function of substrate thickness H_S and electrode suspension length U. (c) and (d) present cuts through the surface plots for a substrate thickness of 0.3 mm. The dashed lines frame the range of values that can be expected from an enhanced displacement ratio according to Ref. [5].

the substrate, i.e., the distance of the countersupports in the three-point bending mechanism, represents an effective handle for controlling the displacement ratio. To reduce the static and dynamic deflection range in the experiments and to minimize the spatial requirements of the bending mechanism, the MCBJ substrates were designed to have minimum length while still leaving the junction area accessible for possible solution deposition processes ($L_S=16~\mathrm{mm}$, $W_S=6~\mathrm{mm}$). Within these boundary conditions, the remaining parameters were chosen to minimize both the required deflection range and the bending force.

The dependence of the bending force on the MCBJ design parameters can be obtained from Equations 3.4 and 3.6:

$$F_B = \frac{2W_S H_S^2 E}{3L_S U} d. {(3.7)}$$

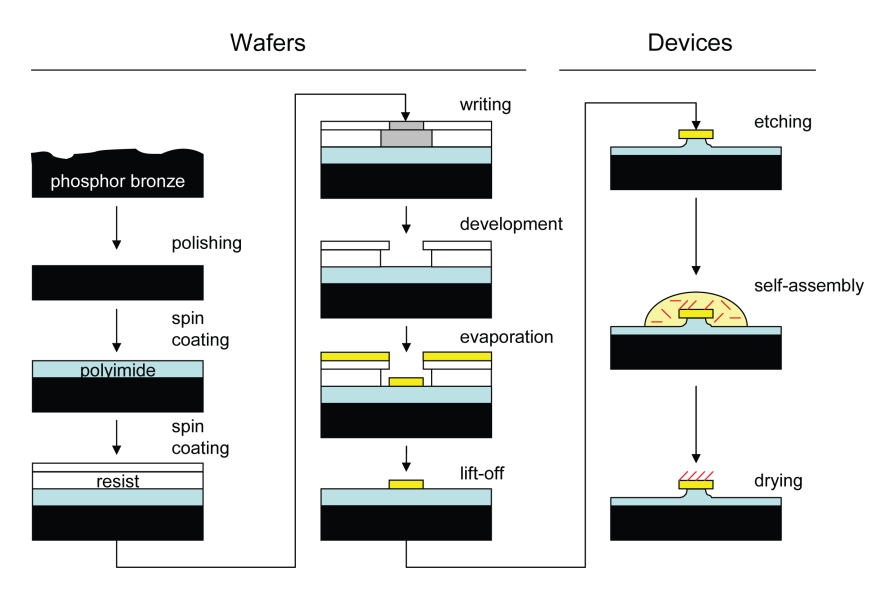


FIGURE 3.3: Schematic of the fabrication process of 2-terminal mechanical controllable break junctions. The fabrication is divided in processing steps on the scale of wafers (two columns on the left) and individual devices (right column).

Independent of all geometrical parameters, the bending force of the MBCJ can be tuned via the Young's modulus of the substrate. Typical materials exhibit moduli ranging from 190 GPa (Si) and 120 GPa (phosphor bronze) to 2.5 GPa (polyimide). In our design, phosphor bronze was chosen due to its well-established elasticity at cryogenic temperatures and due to its suitability for electron-beam lithography (see Section 3.1.3).

To find suitable values for the substrate thickness and the suspended length of the electrode bridge, we considered the necessary deflection for an electrode stretching of d = 20 nm, supposedly sufficient to create a gap to host a molecule.

The calculated theoretical dependence of the deflection and the bending force of a phosphor bronze-based MCBJ on the suspended length U and the substrate thickness H_S is presented in parts a and b of Figure 3.2. There is a trade-off in optimizing the two figures of merit; with increasing substrate thickness the required deflection decreases, but the bending force increases. In order to keep the required actuator force well below 100 N, which is a typical value for cryogenic lead-screw actuators [8], a substrate thickness of $H_S=0.3$ mm was chosen. Parts c and d of Figure 3.2 present the dependence of the substrate deflection and bending force for this thickness on the remaining parameter, the suspended length of the electrodes. Similar to other lithographic MCBJs, it was designed to be around U=2 μ m.

The theoretical displacement ratio for this configuration follows immediately from Equation 3.6, which yields $r = 1.4 \cdot 10^{-5}$. Using a conservative estimate of 2.8 for the enhancement of the displacement ratio by the elasticity of the polyimide [5], we can derive a deflection of $w \approx 0.5$ mm for a junction stretching of d = 20 nm. The required dynamic

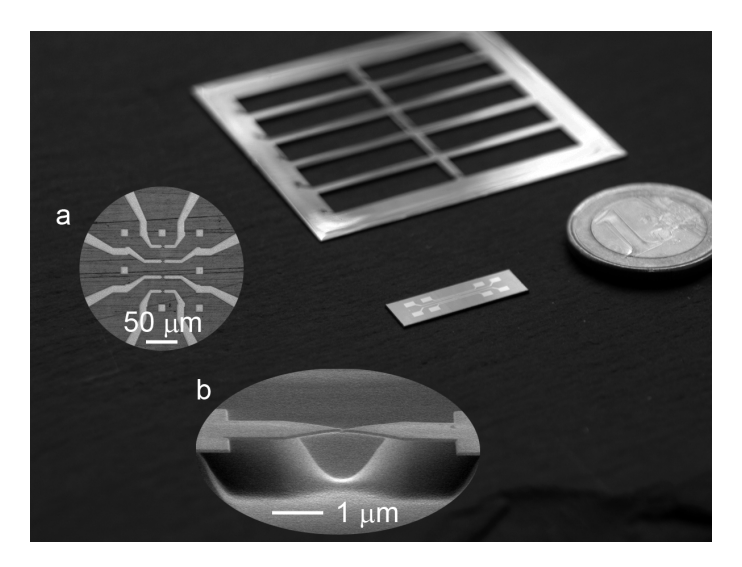


FIGURE 3.4: Photograph of a single MCBJ device (front) and a cut-up wafer (back). Inset (a) shows a micrograph of the device center. It hosts four parallel junctions that can be probed individually. Inset (b) presents a scanning electron micrograph of an underetched break junction.

deflection range for the periodic breaking and fusing of the contact over the typical length of a molecule ($\Delta d=2$ nm) is on the order of 50 μ m. The expected maximum bending force is around 8 N.

3.1.3 FABRICATION OF LITHOGRAPHIC MCBJS

The fabrication of two-terminal lithographic MCBJs for this Thesis builds on a process that has been developed by van Ruitenbeek et al. [3]. Figure 3.3 presents a schematic of the fabrication procedure. Phosphor bronze wafers (thickness 0.3 mm) are polished and cleaned by ultrasonication in acetone and isopropanol. After the application of an adhesion promoter (VM651, HD Microsystems) the wafers are spin-coated with a commercial polyimide precursor solution (PI2610, HD Microsystems). The films are then cured in a vacuum oven at up to 300°C. At such high temperatures the precursor is expected to cross-link completely and to expel remaining solvent. The thickness of the resulting polyimide layer is around 3 μ m, sufficient for the electrical isolation of the break junction devices from the metallic substrate. For the subsequent electron-beam lithography step the wafers are spin-coated with a double layer of resist (320 nm methylmethacrylatemethacrylic acid (MMA(17.5)MAA) copolymer, followed by 110 nm polymethylmethacrylate (PMMA) with a molecular weight of 950k; both from Microchem Corporation). The lower layer in the resist stack is more sensitive toward electron radiation than the upper one. This leads to an undercut in the developed patterns and facilitates lift-off processes. We then define 10 devices on a wafer with 4 break junctions in each device using a Leica electron-beam pattern generator. In each junction two contact wires narrow down into a thin bridge, which is approximately 100 nm wide and 200 nm long. After exposure we develop the patterns in a mixture of methyl-isobutyl-ketone and isopropanol (volume ratio 1:3). Electron-beam evaporation is then used to deposit a very thin sticking layer (1 nm of Cr) and the electrode layer (80 nm of Au). After lift-off in hot acetone and a rinsing step in isopropanol we protect the fully processed wafers with a 500 nm thick layer of PMMA 350k and remove the individual break junction devices from the wafer using laser-cutting (not shown in Figure 3.3).

The final step of the fabrication process, the underetching of the electrodes, is carried out on the individual devices immediately before each experiment. We remove the protection layer of the individual devices by immersion in hot acetone, followed by immersion in isopropanol. The devices are then etched in a reactive ion etcher using a mixture of CF₄ and O₂ gas (flow rate ratio around 1:4, pressure 0.2-0.3 mbar, RF power 20-80 W). This results in a highly reactive high-density oxygen plasma and yields a nearly isotropic etch profile with a suspended electrode length of about 2 μ m (see Figure 3.4b). Devices that are intended for molecule measurements are dipped into fresh ethanol immediately after etching. This is expected to reduce possible gold oxide on the surface [9]. Gold oxide can be encapsulated under molecular monolayers and reduce the reproducibility of self-assembly processes [9, 10].

3.2 THE EXPERIMENTAL SETUP - A CRYOGENIC THREE-POINT BENDING APPARATUS

The design of the MCBJ measurement setup aims at vacuum-based experiments at both room temperature and cryogenic temperatures by using an insert that fits into commercial helium-4 storage dewars. It has been developed in close collaboration with Ruud van Egmond (Leiden University). Two versions of the MCBJ insert were designed and built. The second-generation insert comprises an improved actuation mechanism, which will be discussed in more detail in Section 3.2.2. In both realizations of the MCBJ insert a lower boundary for the measurement temperature is given by the temperature of liquid helium at ambient pressure, i.e., about 4.2 K.

3.2.1 DESIGN OF THE VACUUM INSERT

Figure 3.5a presents an overview of the vacuum insert. For maximum flexibility, the design comprises a modular head to host all vacuum feedthroughs, a central tube section that mates with a pot to form a vacuum sample space at the bottom, and a modular bending mechanism. The overall length of the insert is around 1200 mm; its diameter is 48 mm. The head of the insert is the interface to the MCBJ device. It is equipped with two vacuum flanges and a ferrofluidic rotary feedthrough (Rigaku RMS-BS-6) for the mechanical control of the MCBJ. Six small plate mounts allow for interchangeable electrical or optical connections. All modular parts are connected by screws and sealed using rubber O-rings. The design of the tube section of the insert and the bending actuators follows the principles of cryogenic engineering. At low temperatures, mismatches in thermal expansion coefficients may hamper the actuation mechanism. Furthermore, heat influx from room temperature parts of the insert can lead to the evaporation of helium and heating of the

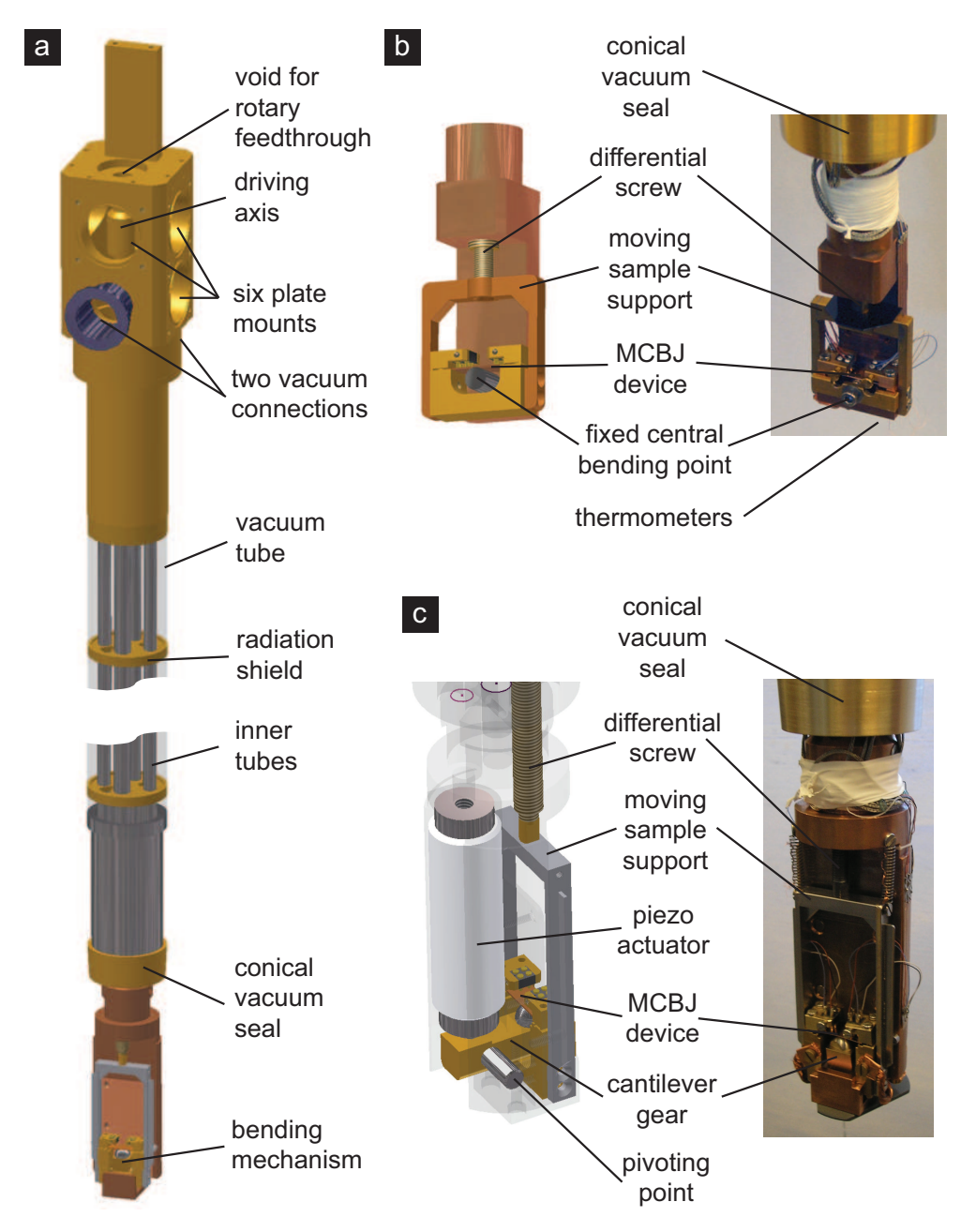


FIGURE 3.5: Details of the vacuum insert used in the MCBJ experiments. (a) Complete drawing of the insert. The sample space at the bottom can be closed off with a pot that mates with the conical seal. (b) Detail of the first-generation three-point bending mechanism, which is based on a differential screw drive. (c) Detail of the second-generation bending mechanism, which combines an amplified piezo actuator with a differential screw similar to b.

	$\bar{\lambda}_{77K4K}$	$\bar{\lambda}_{300K4K}$	$\bar{\lambda}_{4K1K}$
Stainless steel	4.5	10.3	0.2
Brass	26	67	1.7
Copper	80	160	5
Polyimide (Kapton)	0.07	0.15	0.01

Table 3.1: Mean thermal conductivities of the most important materials used in the design of the MCBJ setups. All values are given in W/Km [11, 12].

sample above 4.2 K. The evaporation is especially critical in experiments in storage dewars, which contain only a limited amount of cryogenic liquid. In order to increase the available measurement time, heat conduction through the solid parts of the setup has to be minimized. Therefore, we paid close attention to the choice of materials and the geometry of the tube section of the insert.

In a simple approximation, the heat flow between two points of different temperatures T_1 and T_2 in a bulk material is given by its cross section A, length l and thermal conductivity $\lambda(T)$:

$$\dot{Q} = \frac{A}{l} \int_{T_1}^{T_2} \lambda(T) dT \approx \frac{A}{l} \lambda_{T_2..T_1} (T_2 - T_1)$$
(3.8)

The right hand side of Equation 3.8 may be used as an approximation in the case of thermal anchoring at points of stationary temperature, e.g. at room temperature, in liquid helium, or in liquid nitrogen. An overview of the thermal conductivities of the materials that are used in the MCBJ insert is given in Table 3.1.

To minimize the heat influx into the helium bath, an insert with a small thermal conductivity, a reduced cross section and a large length is desirable. At the same time, a good vacuum at the location of the sample requires a small pumping resistance, i.e., a large open cross section. Therefore, the outer shell of the insert is made from a wide (48 mm) stainless steel tube of minimal wall thickness (0.3 mm). It hosts five small stainless steel tubes, which can be used to guide wiring, glass fibres, and other connections to the MCBJ device. One of the inner tubes contains the driving axle of the bending mechanism. At distances of about 100 mm, the inner tubes are embedded in brass heat shields that absorb and reflect thermal radiation from the insert head.

The design of the bottom of the insert followed a different route to minimize the device temperature. All bulk parts of the actuation mechanism are made from either copper or brass (see Section 3.2.2). This increases the thermal conduction from the MCBJ device to the conical seal of the vacuum chamber, which is in direct contact with the helium bath, and effectively cools the device.

It is instructive to compare the experimental performance of the setup to the predictions of Equation 3.8. Theoretically, a temperature gradient from 300 K to 4.2 K over 100 cm leads to a heat influx on the order of 0.25 W via thermal conduction through the stainless steel tubing. For liquid helium with a standard enthalpy change of $\Delta_{\nu}H^{\Theta}=0.0845$ kJ/mol

or an evaporation rate of about 1.4 l/Wh, this would result in a helium loss of 0.3 l/h. This value is in reasonable agreement with cryogenic experiments, which show a liquid helium boil-off around 0.2 l/h. The reduced evaporation rate may be attributed to the additional cooling power of the surrounding, cold helium gas. The base temperature at the position of the MCBJ device is around 6 K, as measured by a temperature-dependent resistor on the moving sample support (see Section 3.2.3). This value is close to the temperature of liquid helium and confirms the efficient thermal anchoring of the MCBJ bending mechanism to the surrounding bath.

3.2.2 ACTUATION MECHANISM

The choice of the linear actuator used for bending the MCBJs is closely linked to the device design. It must supply a sufficient force to bend the substrate, a large enough range to enable full breaking and repeated fusing of the MCBJ, and a high-resolution encoding mechanism for a precise control of the deflection of the device.

In the case of experiments at room temperature, there is a vast choice of off-the-shelf components that offer these merits. These are largely based on combinations of piezoceramic stacks and screw-based actuators. Moving to cryogenic temperatures, however, immediately reduces the number of usable actuator concepts. Piezo stacks are still functional at 4.2 K but exhibit an expansion reduction to 10-20% of their room temperature range. For a 58-mm-long high-voltage piezo stack (PI P-016.40P, nominal expansion 60 μ m/1000 V), this results in a reduction of the mechanical range to less than 12 μ m/1000 V, a value that falls short of the required dynamic bending range derived in Section 3.1.1. Cryogenic screw-based actuators would cover this range but are not available commercially. However, the principle can readily be adapted if sufficient care is taken to match the thermal expansion coefficients of all components. Recent examples of the application of this principle include an external servo motor driving a MCBJ setup [13] and a cryogenic stepper motor for space applications [8].

The bending actuator in our first-generation setup is based on a brushless servo motor (Faulhaber 3564K024B) and a differential screw drive close to the MCBJ device (see Figure 3.5b). The rotation of the motor is transferred to the screw via a ferrofluidically sealed feedthrough in the insert head and a rotating axle in the tube section of the insert. At the bottom of the insert, the screw moves the two countersupports in the three-point bending mechanism downwards and effectively deflects the center of the substrate. The displacement resolution of this actuator can be determined from the angular resolution of the motor drive, $\Delta \phi$, and the pitch of the screw, P:

$$\Delta z = \frac{P}{2\pi} \Delta \phi. \tag{3.9}$$

For sub-micron resolution a pitch well below 1 mm and step angles on the order of degrees are desirable. The resolution can be increased by employing a differential screw with an inner pitch P_i and an outer pitch P_o , leading to an effective differential pitch of $P = P_{diff} = P_o - P_i$. A further refinement can be achieved by attenuating the motor action using a gear box with a ratio of $r_g >> 1$. The attainable displacement resolution then

becomes

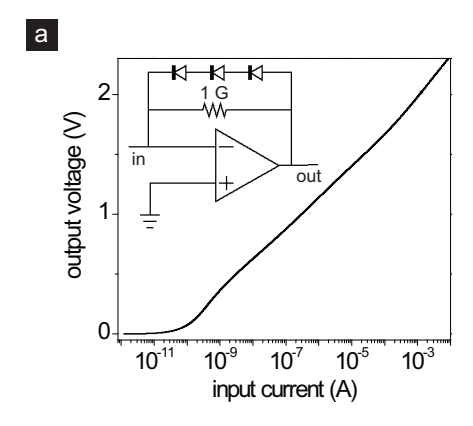
$$\Delta z = \frac{P_{diff}}{2\pi} \frac{\Delta \phi}{r_g}.$$
 (3.10)

In the case of the MCBJ actuator displayed in Figure 3.5b, the servo motor has been combined with a gear box of $r_g=246$ and a differential screw with a pitch of $P_{diff}=250~\mu m$. The design materials of the differential screw increase its useful life. With an outer nut from copper, a cylinder from brass, and an inner screw from brass, wear is kept to a minimum. Furthermore, the screw is coated with molybdenum disulfide powder, which acts as a dry lubricant. With a motor positioning accuracy on the order of 12° , the attainable resolution at the output side of the gear box becomes 0.05° . The resulting step size of the screw drive is about 25 nm, corresponding to about 1 pm in electrode distance. During a continuous actuation of the MCBJ, the speed of the servo motor is controlled and the deflection does not suffer from discretization inaccuracies (see Figure 3.8 for an example of continuous bending). The screw-based actuator is typically run at speeds up to $2~\mu m/s$.

In the second-generation MCBJ insert, which was built at the end of the PhD project that led to this Thesis, a differential screw with a pitch of $P_{diff}=150~\mu m$ has been combined with an amplified piezo actuator (see Figure 3.5c). Similar to the first setup, the differential screw can be used to control the substrate deflection over several 1000 μm . For improved lubrication, it is coated with a cryogenics-compatible tungsten disulfide layer (Dicronite DL-5, Lubrication Sciences International). Due to the combination of a piezo stack (PI P-016.40P) and a cantilever mechanism with a mechanical amplification of 4.6, the nominal piezo-driven deflection range of the second MCBJ actuator is as large as 280 $\mu m/1000$ V at room temperature. This value is sufficient for a full breaking and fusing cycle of a MCBJ (see Section 3.1.1). Furthermore, the large-signal response of the piezo-ceramic actuator is linear for voltage ramps up to 2000 V/s. This value corresponds to an actuation speed of about 600 μ m/s or 30 nm/s on the scale of the electrodes, using a displacement ratio of $5 \cdot 10^{-5}$. Such high actuation speeds enable a fast mechanical control over single-molecule junctions, which can be crucial in the case of statistical measurement approaches (see Section 3.3).

3.2.3 MEASUREMENT ELECTRONICS AND WIRING

All measurement electronics are controlled and read out with the help of an ADwin-Gold unit (Jäger Computergesteuerte Messtechnik). Besides analog-digital (AD) and digital-analog (DA) converters it hosts an on-board digital signal processor (DSP), which enables real-time analysis and control of all signal levels. The maximum data acquisition rate at 16 bit resolution is about 200 kHz, and the maximum DSP clock speed amounts to 400 MHz. All measurement electronics are hosted by a shielded rack. To reduce interference from the ADwin they are accessed via optically coupled isolation amplifiers. The power of the low-noise measurement electronics and the isolation amplifiers is supplied by two separate batteries, resulting in full galvanic isolation of the different circuits. The measurement rack can host several home-built electronics units, among which voltage sources,



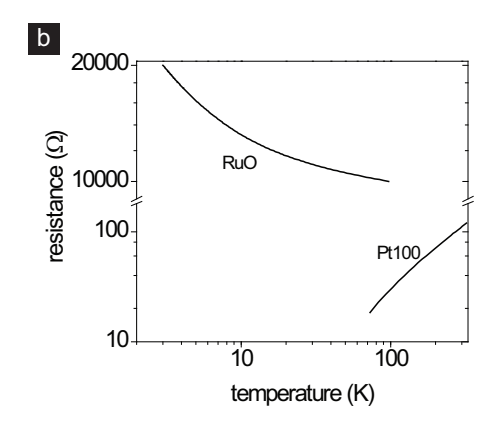


FIGURE 3.6: (a) Calibration curve of the logarithmic current-voltage converter that was designed for wide-range conductance measurements. The inset presents a very simplified schematic of the corresponding electronic circuit. (b) Temperature-dependent characteristics of the resistors that were mounted on the sample holder for thermometry.

current sources, current-voltage converters, and voltage amplifiers. For the MCBJ measurements, a dedicated logarithmic current-voltage converter has been developed. It allows for current measurements across more than six orders of magnitude and is equipped with a temperature-drift compensation stage. Pointwise calibration with standard resistors ranging from $100~\Omega$ to $1~G\Omega$ ensures the accuracy of the conversion, similar to experiments reported by He *et al.* [14]. A plot of the transmission characteristics of the converter is presented in Figure 3.6a.

The MCBJ setup can be accessed via a matrix box. The inputs of the matrix are equipped with grounding switches that prevent voltage spikes on the device. Furthermore, all lines are low-pass filtered to reduce high-frequency interference.

In order to prepare the MCBJ setup for future extensions, multi-pole electrical vacuum feedthroughs have been employed. The eight wires leading to the device are guided into the insert via a 24-pole connector (Fischer connectors). The connections to the sample space are made via shielded twisted pairs of $100~\mu m$ -thick phosphor bronze wires. These have a smaller thermal conductivity and a larger resistivity ($30~\Omega/m$) than copper and reduce heat conduction to the MCBJ device. At the bottom of the insert, all wires are connected to thermalization striplines. Connection to the pads of the MCBJ devices is made by eight gold-plated spring-loaded contacts (see parts b and c of Figure 3.5).

The eight wires leading to the MCBJ device are spatially separated from the thermometer wiring, which is guided through a 12-pole Jaeger connector (David Emery Corporation). The temperature of the sample holder in the bending mechanism can be monitored by means of a standard Pt-100 stripline resistor and a calibrated RuO thick-film resistor. To establish good thermal contact, these are glued onto the polished surface of the sample support (see Figure 3.5) using heat-conducting epoxy. Both resistors are contacted in a 4-probe configuration. Figure 3.6b presents the temperature-dependent resistances of the thermometers.

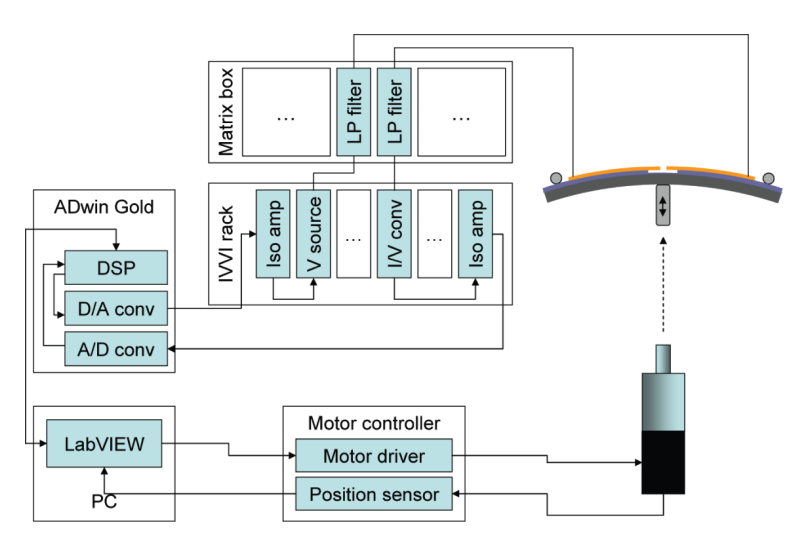


FIGURE 3.7: Schematic of the MCBJ measurement setup. The electronics and the actuator are simultaneously controlled by a LabView program.

3.3 MEASUREMENT TECHNIQUES

The MCBJ experiments have been automated using the LabView development package (National Instruments). Figure 3.7 presents a schematic of the complete experimental setup. The measurement software controls both the motorized bending mechanism and the measurement electronics, while outsourcing some of the real-time data analysis to the DSP of the ADwin-Gold unit. The program allows for the simultaneous control of three outputs (bias voltage, gate voltage, and piezo voltage) and for the monitoring of two inputs. It comprises the following sub-routines:

- Configuration of the actuator (bending limits, motor drive parameters) and the measurement electronics (bit resolution and gain)
- · Conductance measurement as a function of time
- Junction initialization to a set conductance value with the option of holding this value via a feedback loop with the actuator
- · Measurement of conductance traces during the bending of a MCBJ device
- Measurements of conductance histograms using the bending position or the junction conductance as a control parameter for the actuator motion
- Statistical measurement of IV-characteristics
- Three-terminal measurements for gated MCBJs

In the remaining part of this chapter, some of these measurements will be presented in more detail.

3.3.1 CONDUCTANCE TRACES

The measurement of the conductance evolution during the joining and the separation of two electrodes is one of the most established techniques for single-molecule studies in mechanically controllable break junctions [15, 16]. As a metallic contact is stretched its cross section is reduced. This leads to a decrease in conductance that can be monitored and plotted as a function of stretching. The details of the conductance evolution may vary from contact to contact, but it generally displays a step-like pattern [17]. Figure 3.8a presents examples of the conductance evolution of a clean gold junction at cryogenic temperatures. The step-like pattern in the metallic regime above 1 G_0 can be attributed to stable atomic configurations of the tip. The last plateau at 1 G_0 corresponds to a single-atom contact (see Chapter 2). Stable single-molecular junctions lead to steps in the conductance evolution in the sub- G_0 regime [16].

In measurements of conductance traces, the MCBJ substrate is bent at a constant speed and under a fixed applied bias while the current is being measured. The junction conductance is then deduced from the current by applying Ohm's law. Due to a variation in displacement ratios between different devices the conductance can not readily be displayed as a function of the electrode distance. Rather, it is plotted over time or substrate bending. A separate calibration experiment (see Section 3.4.3) would be required to obtain the exact displacement ratio of each MCBJ device.

3.3.2 CONDUCTANCE HISTOGRAMS

Due to intrinsic variations in the conductance evolution of atomic-scale junctions, a large number of breaking traces has to be acquired and analyzed statistically. The automatized acquisition of conductance traces for the construction of histograms can be controlled with a feedback on either the substrate bending or the junction conductance. Histograms within a fixed bending range may be useful when studying junctions with very reproducible mechanical behavior, i.e., mostly for measurements at low temperatures. In the case of mechanical drift or large conductance fluctuations, which are common at room temperature, it is more favorable to cycle a MCBJ device within a fixed conductance interval. This was the method of choice for all measurements for this Thesis.

Once a statistically significant dataset has been acquired (typically hundreds of conductance traces), it is analyzed by means of conductance histograms [17]. Individually sampled data points from conductance trace measurements serve as the elements in the construction of these histograms. The entire conductance range is split into short intervals, so-called conductance bins. Each time a particular conductance value is recorded the number of counts in the respective bin is increased. In the final histogram, the largest number of counts indicates the most stable junction configuration.

In conductance histograms of metal point contacts, the bins are usually spaced linearly. This approach is suitable since the studied conductance range is typically narrow. In single-molecule junctions, however, variations in the geometry may lead to a large spread in conductance. Consequently, conductance histograms of MCBJs that have been exposed to molecules may contain wide peaks in the sub- G_0 regime and, due to the finite probability of trapping a molecule, a considerable fraction of background counts from vacuum tunneling. The contribution of these counts to the histogram can be estimated from a

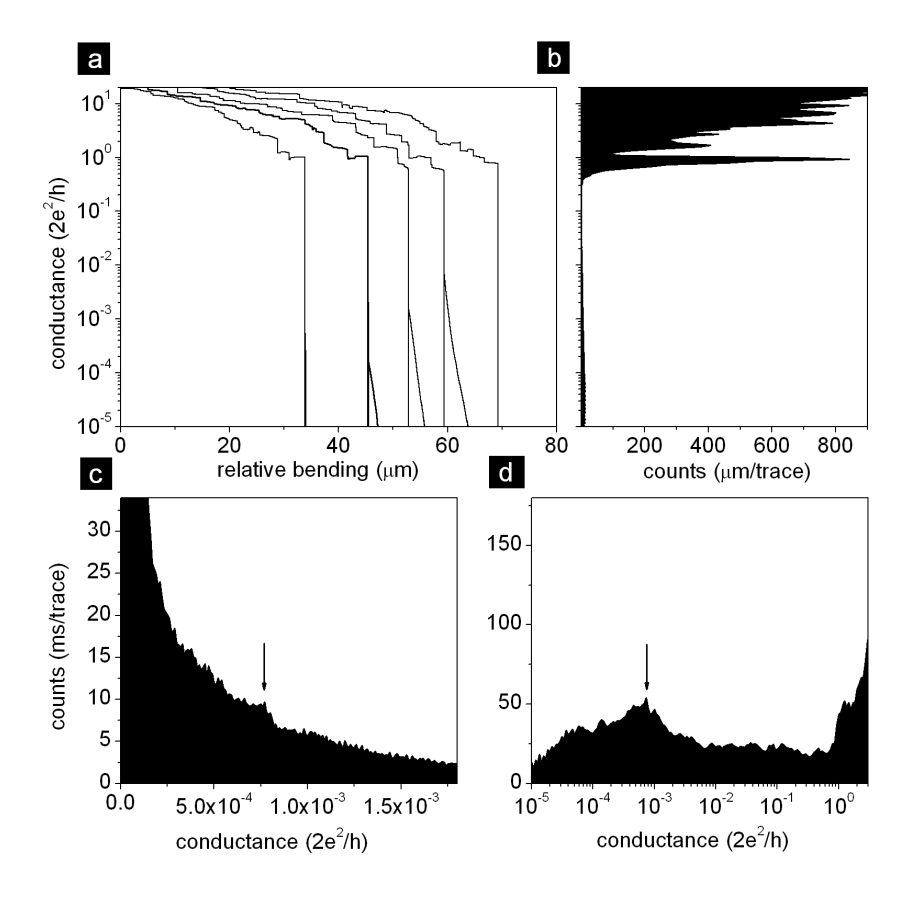


FIGURE 3.8: (a) Examples of the conductance evolution of a gated MCBJ with suspended gold electrodes during the bending of the substrate at 2 μ m/s. The experiment was carried out at a temperature of 6 K and a bias voltage of 50 mV. (b) Logarithmic conductance histogram from several hundreds of breaking traces similar to the ones in part a. (c) and (d) A linear and a logarithmic conductance histogram constructed from a dataset of 500 breaking traces of a two-terminal MCBJ exposed to 1,6-hexanedithiol. The experiment was carried out at room temperature with a bending speed of 2 μ m/s and a bias voltage of 50 mV. The arrows mark the position of the molecular signature in the histograms.

simple tunneling model, in which the conductance decreases exponentially with increasing electrode distance (see Chapter 2):

$$G(d_0 + \Delta d) = G(d_0) \exp(-2k\Delta d), \text{ and}$$
(3.11)

$$\lg G(d_0 + \Delta d) = \lg(G(d_0)) - 2k\Delta d \lg e, \text{ where}$$
(3.12)

$$k = \frac{\sqrt{2m_e\Phi_m}}{\hbar}. (3.13)$$

The distance change between the electrodes follows from the bending of the MCBJ device as $\Delta d = r\Delta z$, where Δz is the change in bending of the substrate and r is the displacement ratio of the junction (see Equation 3.6). The number of counts per bin in the conductance histogram can be deduced from

$$N_G(G)dG = N_{\lg G}(\lg G)d\lg G = -N_z(z)dz,$$
 (3.14)

where $N_G(G)$, $N_{\lg G}(\lg G)$, and $N_z(z)$ are the probability densities of acquiring conductance data at certain values of G, $\lg G$, and z. The data density N_z is a measurement parameter and can be deduced from the bending speed of the junction, v_z , and the data sampling rate S:

$$N_Z(z) = \frac{S}{\nu_Z},\tag{3.15}$$

Combining Equations 3.12, 3.13, 3.14 and 3.15 one obtains

$$N_{\lg G}(\lg G) = \frac{S}{2\nu_z k r \lg e} \text{ and }$$
 (3.16)

$$N_G(G) = \frac{S}{2\nu_z kr} \frac{1}{G}.$$
(3.17)

Obviously, the signature of vacuum tunneling in a linear conductance histogram increases with decreasing G. The tunneling background in a logarithmic histogram, in contrast, is constant. Figure 3.8b presents a logarithmic conductance histogram [18] constructed from hundreds of breaking curves of a clean gold contact. The dominant peak at 1 G_0 corresponds to recurring conductance plateaus in the breaking traces and indicates conductance quantization. Parts c and d of Figure 3.8 present a linear and a logarithmic conductance histogram that were constructed from the same set of consecutive breaking traces of a junction exposed to 1,6-hexanedithiol. The small conductance peak in the linear histogram is superimposed on a dominant hyperbolic background of counts that is in good agreement with Equation 3.17. In the case of logarithmic binning, the constant tunnelling background clearly facilitates the identification of the molecular signature. Hence, conductance histograms throughout this Thesis are plotted as a function of $\lg G$.

3.3.3 TRACE HISTOGRAMS

Two-dimensional trace histograms aim at a statistical analysis of the time-dependent conductance evolution of a molecular junction upon stretching [19, 20]. Thus far, the stretching dependence has almost exclusively been evaluated in the form of plateau length histograms [21–23]. However, lithographic MCBJs are broken at a very slow speed, which

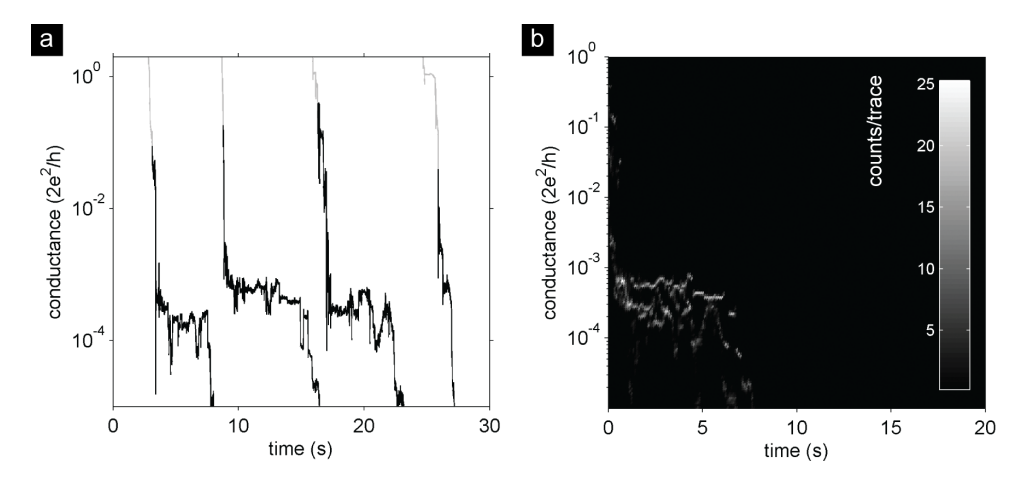


FIGURE 3.9: An example of the construction of two-dimensional trace histograms. Part (a) presents conductance traces obtained during the breaking of a junction exposed to 1,6-hexanedithiol at room temperature. For clarity, the traces are offset in time. Trace points in black have been identified as non-metallic by the algorithm described in the text. The end of the metallic regime was associated with the first conductance drop by more than a factor of 2. Part (b) presents the two-dimensional histogram constructed from the black data in (a). The binning has been carried out at 30 bins/lg G and 10 bins/s.

allows for fluctuations within and before conductance plateaus in the sub- G_0 regime (see Figure 3.9a). This renders algorithms for the detection of molecular conductance steps sensitive to artifacts. Hence, we based the construction of the trace histograms on the robust conductance plateau of gold at one quantum of conductance. The trace histogram method builds on the assumption that the part of the conductance trace that follows the rupture of the last gold-gold bond is characteristic of the formed single-molecule junction. To extract this data, the breaking traces are analyzed pointwise starting from a conductance slightly above 1 G_0 . The first substantial conductance drop is then regarded as the beginning of the non-metallic transport regime, and subsequent datapoints are analyzed further.

Figure 3.9a illustrates the application of this algorithm to breaking traces of a junction exposed to 1,6-hexanedithiol. The black breaking data in the figure are recognized as non-metallic. To enable the statistical analysis the time stamp of the first selected datapoint in each breaking trace is set to zero seconds. All black data are then binned in time and conductance. The resulting two-dimensional trace histogram is presented in Figure 3.9b. In the trace histogram, the conductance plateaus that are visible in the individual traces appear as horizontal lines. For a larger set of breaking traces, these signatures overlap to form an area of increased counts. The vertical spread of this area contains information on the variability in the conductance of the single-molecule junctions, and the horizontal spread corresponds to their lifetime.

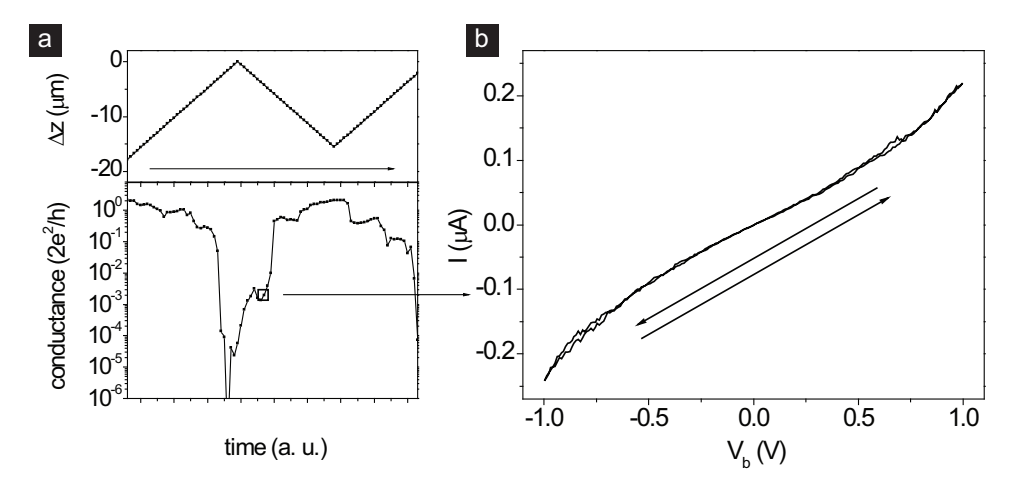


FIGURE 3.10: An example of the data obtained during a statistical IV measurement. Part (a) presents plots of the low-bias conductance at a dc bias of 25 mV and the relative bending of the substrate. Part (b) presents the IV characteristics of the junction at the point enclosed by a square.

3.3.4 STATISTICAL *IV* MEASUREMENTS

Similar to conductance traces, *IV* measurements on single molecule junctions exhibit large intrinsic variations. A method introduced by Lörtscher *et al.* tries to capture this spread by measuring statistically significant sets of *IV* characteristics on a junction that is subjected to repeated fusing and breaking [24]. This method has been adapted for some measurements for this Thesis.

In such an experiment, the MCBJ is bent in discrete steps on the order of 0.1 to 1 μ m with a feedback on the junction conductance. Typically, the upper boundary of the conductance window is given by a metallic contact of a few G_0 to enable a reorganization of the anchoring site. The lower boundary may be given by a finite conductance or the resolution limit of the measurement. At each bending position, the low-bias conductance and stability are examined during a short measurement of the current as a function of time. Subsequently, several voltage sweeps are carried out and the junction current is measured simultaneously. Besides the raw IV traces, the program also records an averaged curve with improved signal-to-noise ratio. Figure 3.10a presents an example of a low-bias conductance trace obtained during a statistical IV measurement together with the corresponding relative substrate bending. The data have been acquired from left to right, and each datapoint marks an individual IV measurement.

3.3.5 THREE-TERMINAL MEASUREMENTS

Three-terminal measurements represent the most detailed dc characterization of single molecule junctions and can be applied in gated MCBJ devices. The voltage on one of the device terminals, typically the gate, is ramped up in steps while the other voltage, the source-drain bias, is swept within a fixed interval. The junction current is measured simultaneously. Three examples of *IV* sweeps of a gated MCBJ at different gate voltages

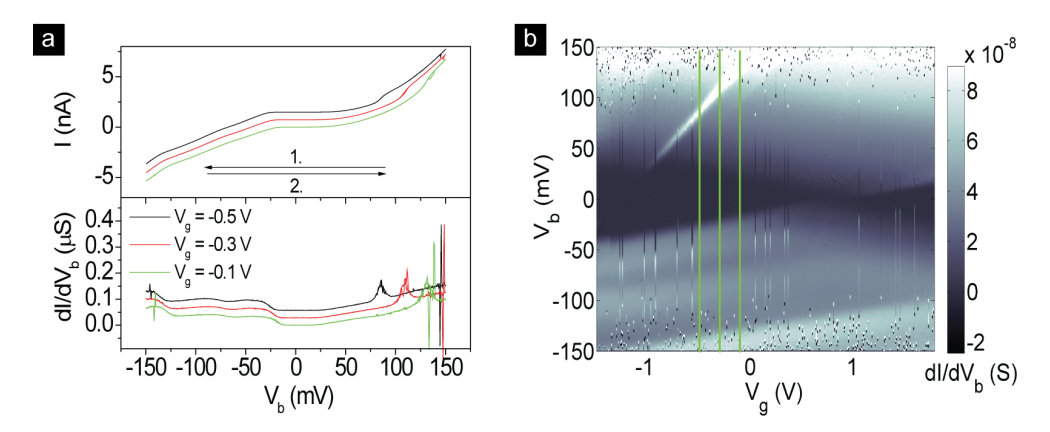


FIGURE 3.11: An illustration of the three-terminal measurement used to characterize gated MCBJs. (a) IV characteristics and numerical differential conductance for three different gate voltages. The arrows indicate the sweep direction of the bias voltage. (b) Two-dimensional greyscale plot of the differential conductance. The vertical lines indicate the locations of the scans in part (a). The differential conductance is encoded by different shades of grey as given in the scale bar.

are presented in Figure 3.11a. A numerical derivative of these characteristics is given in the lower panel. To illustrate the dependence of the differential conductance dI/dV_b on both the bias voltage and the gate voltage it can be plotted in a two-dimensional map (see Figure 3.11b).

3.4 MECHANICAL CHARACTERIZATION

3.4.1 STABILITY OF THE SETUP

The intrinsic mechanical attenuation of the MCBJ architecture leads to a very low drift and a good vibration isolation of the suspended electrodes [3]. To test the long-term stability of the electrodes we have broken a clean device at cryogenic temperatures and adjusted its tunneling resistance to a value in the M Ω range. Figure 3.12 presents the result of the subsequent conductance measurement over time. Within 4 hours, the device conductance of $5 \cdot 10^{-3}~G_0$ changed by not more than 10%. This value can be translated into a distance variation by less than 30 pm and confirms the stability of the electrodes. The time scales of most measurements of single-molecule junctions are much shorter than the one of Figure 3.12, meaning that the MCBJs are well suitable for the experiments described in Section 3.3.

3.4.2 BACKLASH OF THE ACTUATOR

We have tested the backlash in the first-generation measurement setup at both room temperature and at liquid helium temperatures. Figure 3.13a presents the conductance evolution of a clean MCBJ as a function of bending at room temperature. At a substrate deflection of 1013 μ m, its conductance drops from a value of 1 G_0 to about 10^{-4} G_0 ; the last single-atom contact between the electrodes has been cleaved and the junction has en-

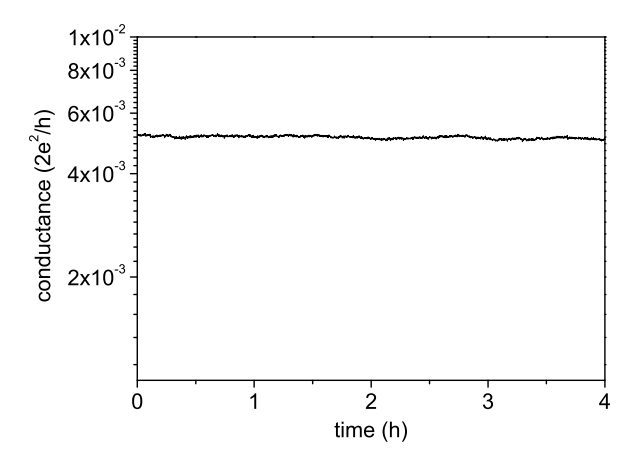


FIGURE 3.12: Test of the long-term stability of a MCBJ device in the tunneling regime at a temperature of 7 K. The conductance was measured at a bias voltage of 50 mV.

tered the vacuum tunneling regime. As the bending is increased further, the conductance decreases roughly exponentially before leaving the range of the logarithmic IV converter at a bending of about 1017 μ m. As the direction of the actuation is reversed, the conductance crosses the lower limit measurement range at a substrate bending of about 1012 μ m, compared to 1017 μ m in the breaking trace. The apparent difference of 5 μ m can be due to backlash in the actuator of the setup. However, part of it may also be attributed to a retraction of the electrodes between the measurements of the breaking and the fusing curve. At room temperature, gold is highly mobile and the diffusion of atoms can modify the shape of the electrodes. The fluctuations in the tunneling conductance during the fusing of the junction in Figure 3.13a indicate such rearrangements.

Detailed information on the intrinsic mechanical backlash of the setup can be obtained from the breaking characteristics at cryogenic temperatures (see Figure 3.13b). Compared to the exponential conductance decrease in the breaking trace, the exponential increase in the fusing trace is shifted by about 1 μm on the bending axis. This difference corresponds to the backlash in the actuator. Furthermore, the conductance slope of the fusing trace shows slight variations, which can be due to irregularities in the screw drive of the setup. In the bending mechanism, the MCBJ substrate acts as a spring that pushes the differential screw towards the top of the setup. Upon inverting the rotation direction of the differential screw, the substrate spring force may exhibit some variations that show up in a nonlinear response of the electrode distance. In all conductance trace measurements described in this Thesis, we have minimized the effect of the nonlinear actuator response on the fusing characteristics by adding a deflection of several micrometers at the end of a breaking trace. Furthermore, two supporting springs have been included in the second-generation

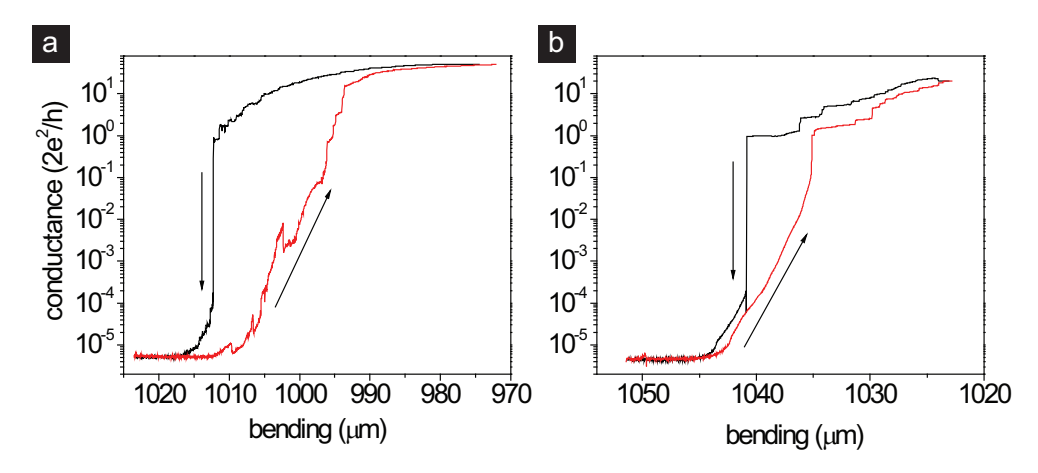


FIGURE 3.13: Test of the backlash of the MCBJ setup at (a) room temperature and (b) 6 K. The arrows indicate the direction of the actuator motion.

setup to provide a better-defined mechanical referencing of the differential screw (see Figure 3.5c).

3.4.3 CALIBRATION OF THE DISPLACEMENT RATIO OF THE MCBIS

We have compared the mechanical attenuation of a clean lithographic MCBJ device at 11 K to the displacement ratio estimated in Section 3.1.2. The experimental characteristics in both the tunneling and the metallic regime can be used to relate the substrate deflection to the distance of the electrode pair.

In the first approach, we analyze the exponential increase of the tunneling conductance with decreasing substrate deflection. Figure 3.14a presents a histogram of the tunneling slope of 240 consecutive closing traces in the range from 10^{-4} to 10^{-3} G_0 . At the end of each trace, the contact was fused to a conductance of 20 G_0 to ensure an atomic reconfiguration of the electrodes. The histogram exhibits a clear peak just above $\partial \left(\lg(G(d)/G_0)\right)/\partial d = 0.5\mu m^{-1}$, which corresponds to the typical tunneling slope of the traces. A more detailed analysis of the data yields a median of $0.54\pm0.06\mu m^{-1}$ that can be related to the theoretical distance dependence of the tunneling conductance in Equation 3.13. For a work function of 5.4 eV in gold, it yields a conductance slope of 1.028 Å $^{-1}$, so that the displacement ratio $r = \partial d/\partial w = (5.3\pm0.6)\cdot10^{-5}$. Compared to the theoretical prediction in Section 3.1.2 it is enhanced by a factor of 3.8, which is in good agreement with Ref. [5]. The large spread in the data in Figure 3.14a may be attributed to mechanical effects: both a misalignment of the electrode tips and nonlinear effects in the differential screw drive can lead to deviations in the conductance slope in the tunneling regime.

In the metallic regime, the signature of atomic chains can be used to calibrate the displacement ratio of the MCBJ. Similar to a single-atom contact, chains of gold atoms exhibit a conductance of nearly 1 G_0 [25, 26]. The corresponding conductance plateaus in breaking traces show statistically preferred lengths, which can be related to integer num-

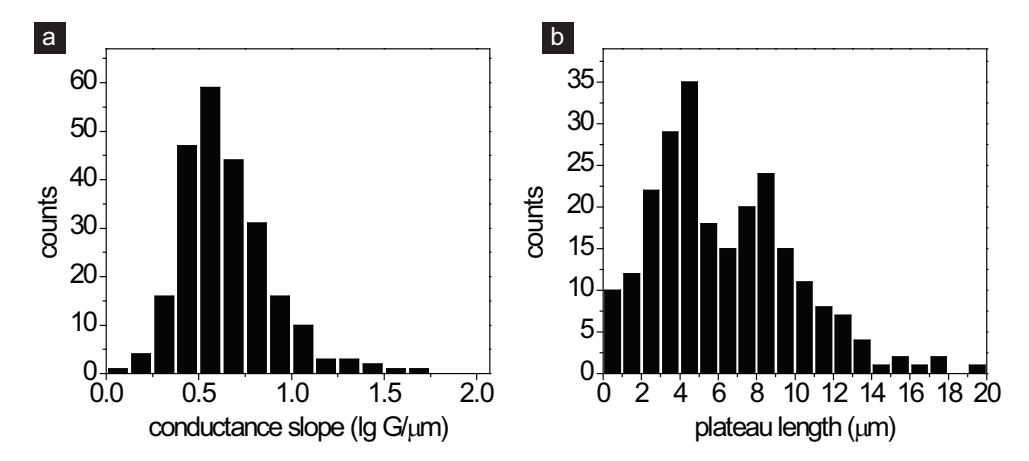


FIGURE 3.14: Calibration of the displacement ratio of a clean two-terminal MCBJ at 11 K. The data were obtained during 240 individual breaking and fusing cycles at a bias of 50 mV. Due to the small dataset the statistics are relatively coarse. (a) Histogram of the conductance slope in the tunneling regime during the closing of the junction. The data were obtained from a smoothed derivative of the bending-dependent conductance between $10^{-4}..10^{-3}~G_0$. (b) Histogram of the plateau lengths in the conductance interval between 0.5-1.2 G_0 . The double peak structure indicates the formation of monatomic chains.

bers of atoms in the chains [27]. We have carried out an analysis of the plateau lengths in the interval from 0.5 to 1.2 G_0 for the dataset discussed above. Figure 3.14b presents a histogram of the conductance plateau length in micrometers of bending. The two peaks just above 4 and 8 μ m indicate the formation of chains of gold atoms and can be used to verify the displacement ratio derived from the data in Figure 3.14a. Earlier experiments have established that the inter-atomic distance in these chains is 2.5 Å [27]. This allows us to estimate a displacement ratio of r = 2.5 Å/4 $\mu m = 6 \cdot 10^{-5}$, which is consistent with the analysis of the tunneling regime.

Hence, a dynamic bending range of 40 μ m is required to cycle the electrode distance by 2 nm. This value is at the upper end of the range of the piezo actuator at cryogenic temperatures but may still enable a fast driving of the junction for histogram measurements. It is also instructive to investigate the deflection that is required to break the pristine MCBJ devices and initiate the metal point contact. The first junctions on a set of 14 MCBJ devices have been found to break at a deflection of $w = 749 \pm 167 \ \mu$ m. Using a displacement ratio of $5 \cdot 10^{-5}$ this can be related to an average stretching distance of about 40 nm before rupture. This value is consistent with the design of the MBCJs and confirms the suitable choice of parameters (see Section 3.1.2).

REFERENCES

- [1] C. J. Muller, J. M. van Ruitenbeek, and L. J. de Jongh, *Experimental observation of the transition from weak link to tunnel junction*, Physica C **191**, 485 (1992).
- [2] J. Moreland and P. K. Hansma, Electromagnetic squeezer for compressing squeezable

REFERENCES 65

- electron tunneling junctions, Rev. Sci. Instrum. 55, 399 (1984).
- [3] J. M. van Ruitenbeek, A. Alvarez, I. Piñeyro, C. Grahmann, P. Joyez, M. H. Devoret, D. Esteve, and C. Urbina, *Adjustable nanofabricated atomic size contacts*, Rev. Sci. Instrum. 67, 108 (1996).
- [4] C. A. Martin, D. Ding, H. S. J. van der Zant, and J. M. van Ruitenbeek, *Lithographic mechanical break junctions for single-molecule measurements in vacuum: possibilities and limitations*, New J. Phys. **10**, 065008 (2008).
- [5] S. A. G. Vrouwe, E. van der Giessen, S. J. van der Molen, D. Dulic, M. L. Trouwborst, and B. J. van Wees, *Mechanics of lithographically defined break junctions*, Phys. Rev. B **71**, 035313 (2005).
- [6] C. Kergueris, J.-P. Bourgoin, S. Palacin, D. Esteve, C. Urbina, M. Magoga, and C. Joachim, *Electron transport through a metal-molecule-metal junction*, Phys. Rev. B **59**, 12505 (1999).
- [7] L. Grüter, M. T. González, R. Huber, M. Calame, and C. Schönenberger, *Electrical Conductance of Atomic Contacts in Liquid Environments*, Small 1, 1067 (2005).
- [8] R.-R. Rohloff, H. Baumeister, M. Ebert, N. Münch, and V. Naranjo, in *SPIE conference Glasgow* (SPIE, 2004), pp. 5495–87.
- [9] H. Ron, S. Matlis, and I. Rubinstein, *Self-Assembled Monolayers on Oxidised Metals. 2. Gold Surface Oxidative Pretreatment, Monolayer Properties, and Depression Formation*, Langmuir **14**, 1116 (1998).
- [10] H. Ron and I. Rubinstein, *Alkanethiol Monolayers on Preoxidised Gold. Encapsulation of Gold Oxide under an Organic Monolayer*, Langmuir **10**, 4566 (1994).
- [11] F. Pobell, Matter and Methods at Low Temperatures (Springer, Berlin, 1996).
- [12] Cryogenics Technologies Group, Tech. Rep., National Institute of Standards and Technology (2009), URLhttp://cryogenics.nist.gov/.
- [13] M. Trouwborst, Ph.D. thesis, Rijksuniversiteit Groningen (2009), URL http://irs.ub.rug.nl/ppn/315902124.
- [14] J. He, O. Sankey, M. Lee, N. Tao, X. Li, and S. Lindsay, *Measuring single molecule conductance with break junctions*, Faraday Discuss. **131**, 145 (2005).
- [15] R. H. M. Smit, Y. Noat, C. Untiedt, N. D. Lang, M. C. van Hemert, and J. M. van Ruitenbeek, *Measurement of the conductance of a hydrogen molecule*, Nature **419**, 906 (2002).
- [16] B. Xu and N. J. Tao, Measurement of Single-Molecule Resistance by Repeated Formation of Molecular Junctions, Science **301**, 1221 (2003).

- [17] J. M. Krans, C. J. Muller, I. K. Yanson, T. C. M. Govaert, R. Hesper, and J. M. van Ruitenbeek, *One-atom point contacts*, Phys. Rev. B **48**, 14721 (1993).
- [18] M. T. González, S. Wu, R. Huber, S. J. van der Molen, C. Schönenberger, and M. Calame, Electrical Conductance of Molecular Junctions by a Robust Statistical Analysis, Nano Lett. 6, 2238 (2006).
- [19] C. A. Martin, D. Ding, J. K. Sørensen, T. Bjørnholm, J. M. van Ruitenbeek, and H. S. J. van der Zant, *Fullerene-based anchoring groups for molecular electronics*, J. Am. Chem. Soc. **130**, 13198 (2008).
- [20] M. Kamenetska, M. Koentopp, A. C. Whalley, Y. S. Park, M. L. Steigerwald, C. Nuckolls, M. S. Hybertsen, and L. Venkataraman, *Formation and Evolution of Single-Molecule Junctions*, Phys. Rev. Lett. 102, 126803 (2009).
- [21] F. Chen, X. Li, J. Hihath, Z. Huang, and N. Tao, Effect of Anchoring Groups on Single-Molecule Conductance: Comparative Study of Thiol-, Amine-, and Carboxylic-Acid-Terminated Molecules, J. Am. Chem. Soc. 128, 15874 (2006).
- [22] Z. Huang, F. Chen, P. A. Bennett, and N. Tao, *Single Molecule Junctions Formed via Au-Thiol Contact: Stability and Breakdown Mechanism*, J. Am. Chem. Soc. **129**, 13225 (2007).
- [23] Y. S. Park, A. C. Whalley, M. Kamenetska, M. L. Steigerwald, M. S. Hybertsen, C. Nuckolls, and L. Venkataraman, Contact Chemistry and Single-Molecule Conductance: A Comparison of Phosphines, Methyl Sulfides, and Amines, J. Am. Chem. Soc. 129, 15768 (2007).
- [24] E. Lörtscher, H. B. Weber, and H. Riel, *Statistical Approach to Investigating Transport through Single Molecules*, Phys. Rev. Lett. **98**, 176807 (2007).
- [25] A. I. Yanson, G. R. Bollinger, H. E. van den Brom, N. Agraït, and J. M. van Ruitenbeek, *Formation and manipulation of a metallic wire of single gold atoms*, Nature **395**, 783 (1998).
- [26] R. H. M. Smit, C. Untiedt, G. Rubio-Bollinger, R. C. Segers, and J. M. van Ruitenbeek, *Observation of a Parity Oscillation in the Conductance of Atomic Wires*, Phys. Rev. Lett. **91**, 076805 (2003).
- [27] C. Untiedt, A. I. Yanson, R. Grande, G. Rubio-Bollinger, N. Agraït, S. Vieira, and J. van Ruitenbeek, *Calibration of the length of a chain of single gold atoms*, Phys. Rev. B **66**, 085418 (2002).

4

LITHOGRAPHIC MCBJS FOR SINGLE-MOLECULE MEASUREMENTS IN VACUUM

In this chapter, we investigate the potential of lithographic mechanically controllable break junctions for single-molecule measurements in vacuum. We study charge transport through the molecular model systems benzenedithiol, benzenediamine, hexanedithiol and hexanediamine. Conductance histograms under different experimental conditions indicate that measurements in vacuum are limited by the surface density of molecules at the contact. Hexanedithiol histograms typically exhibit a broad peak around $7 \cdot 10^{-4}$ G₀. In contrast to recent results on STM-based break junctions in solution we find that the spread in singlemolecule conductance is not reduced by amino anchoring groups. Histograms of hexanediamine exhibit a wide peak around $4\cdot10^{-4}$ G₀. For both benzenedithiol and benzenediamine we observe a large variability in low-bias conductance. We attribute these features to the slow breaking of the lithographic mechanically controllable break junctions and the absence of a solvent that may enable molecular readsorption after bond breaking. Nevertheless, we have been able to acquire reproducible and highly nonlinear current-voltage characteristics of benzenediamine and benzenedithiol junctions. Benzenedithiol measurements yield a conductance gap of about 0.9 V at room temperature and 0.6 V at 77 K. In contrast, the characteristics of benzendiamine-junctions typically display conductance gaps of about 0.9 V at both temperatures.

Parts of this chapter have been published as C. A. Martin, D. Ding, H. S. J. van der Zant, and J. M. van Ruitenbeek, New J. Phys. 10, 065008 (2008).

4.1 Introduction

Most break junction experiments to date have been carried out in solution and in modified scanning tunneling microscopes (STMs). Although this appears to be a very suitable environment for studying single-molecule properties, it also imposes important limitations on the experiments. The temperature range is restricted to a few tens of degrees, and the effect of an electrochemical gate on the molecule depends sensitively on the surrounding liquid. Mechanically controllable break junctions (MCBJs) do not suffer from these restrictions. They can easily be operated down to cryogenic temperatures in a vacuum environment. Furthermore, lithography allows for the combination of the MCBJ architecture with a gate electrode. However, their small displacement ratio of around 10^{-5} limits the measurement speed of lithographic MCBJs. They are usually broken at not more than 1 nm/s [1, 2]. STM break junctions, in contrast, can be operated at maximum breaking speeds of more than 100 nm/s.

This seemingly technical difference can have large consequences for break junction experiments. The importance of stretching speed for the lifetime of single-molecule junctions has only recently been appreciated [3, 4]. Experimental results suggest that the breaking mechanism of metal-molecule bonds changes from a force-dominated one at fast stretching to spontaneous breakdown at low speeds. Furthermore, the chemical nature of the bond is of large importance for the lifetime of single-molecule junctions [3, 5]. Accordingly, the statistical weight of molecular conductance steps in conductance histograms will strongly depend on both the breaking speed of the junction and the molecular anchoring group.

To explore the potential of lithographic MCBJs for single-molecule measurements in vacuum, we have investigated charge transport across different molecular model systems with thiol (SH) and amino (NH₂) anchoring groups (see Chapter 1). Dithiols are prototype systems for the study of single-molecule electronic properties. Their anchoring groups guarantee a dense coverage of both flat and rough gold surfaces [6-8]. Thiols are expected to bind to three sites on the Au(111) surface, the so-called top, hollow and bridge site [9]. Metal point contacts, which exhibit a larger roughness, might even allow for more degrees of freedom in binding and conformation [6]. The chemical versatility of the goldsulfur bond can, however, have detrimental consequences: Simulations suggest that different adsorption geometries can exhibit varying electronic properties both in terms of the electronic coupling and the Fermi-level alignment [10-12]. Experimental observations on a molecule as simple as hexanedithiol support these results. Literature data display a spread over more than two orders of magnitude in conductance and range from $2 \cdot 10^{-5}$ to $2\cdot10^{-3}$ G_0 [13–18]. Likewise, studies of the prototypical π -conjugated benzenedithiol have yielded low-bias conductances between $5\cdot10^{-5}$ and $1\cdot10^{-1}$ G_0 [1, 17, 19, 20]. Recently, the use of diamines for the formation of single-molecule junctions has been pioneered. By changing from thiol to amino anchoring groups, Venkataraman et al. [21] were able to reduce the spread of molecular conductance in STM-based break junctions in solution considerably. The well-defined conductance of amines may be due to the preferential binding to surface adatoms. This motif not only limits the possible adsorption geometries, but its coupling is also relatively independent of bond rotation and tilt angle [22, 23].

To compare the potential of the two different anchoring modes for MCBJ measurements in vacuum, we have studied the molecular model systems 1,6-hexanedithiol (HDT), 1,6-hexanediamine (HDA), 1,4-benzenedithiol (BDT), and 1,4-benzenediamine (BDA). In addition to measurements of the low-bias conductance, we have acquired IV characteristics for junctions of the two benzene derivatives.

4.2 EXPERIMENTAL DETAILS

The MCBJ devices were fabricated following the process described in Chapter 3. Shortly before each measurement we prepared a fresh solution of the molecules of interest in toluene. All glassware used during the preparation procedure was initially cleaned by ultrasonication in fuming nitric acid, followed by ultrasonication in deionized water. After drying, the glassware was ultrasonicated once more in pure toluene (high performance liquid chromatography (HPLC) grade, Aldrich). We then bubbled toluene with nitrogen for at least 30 min in order to expel dissolved oxygen from the solvent and increase the reproducibility of the self-assembly process [6]. BDA, HDT, HDA were used as received from Aldrich. BDT was obtained from Tokyo Chemical Industry (TCI). The concentration of all solutions was around 1 mmol/l. Immediately before the molecule deposition each sample was rinsed in pure toluene and blown dry in a flow of nitrogen gas. We then placed a small drop of the molecular solution on the area of the junctions and left the devices in a toluene-saturated atmosphere for 1 minute to enable the formation of a sub-monolayer of molecules on the electrode surface. After self-assembly, the devices were rinsed thoroughly in toluene and blown dry with nitrogen.

To determine the low-bias conductance of the different molecules we measured conductance histograms (see Chapter 3) at a dc bias of 50 mV. In order to break and re-establish the nanoscale contact (further referred to as breaking and making) the flexible MCBJ substrates were bent at an actuator speed of 2 μ m/s. We used the conductance as a control parameter for this process. Thus, the junctions were cycled between the open and the fused state, given by conductances below 10^{-5} and above several G_0 , respectively. In order to ensure the complete opening of the junction the substrate was automatically deflected by another 50 μ m after the conductance had crossed the lower limit.

During the statistical IV measurements on the benzene derivatives (see Chapter 3 for a description of the method) the MCBJs were bent in discrete steps of 0.5 to 0.7 μ m. At each position, we first determined the low-bias conductance at 25 mV and then acquired 3 to 4 IV traces. The junction currents were measured using a linear IV converter at 10^6 V/A, which resulted in sub-nA resolution. Furthermore, this setting limited the maximum current to 4 μ A. During the systematic IV measurements the low-bias conductance at 25 mV was used as a control parameter for the substrate bending. Thus, the maximum junction conductance during making was limited to a few G_0 .

4.3 OPTIMIZATION OF MEASUREMENT PARAMETERS

Typical breaking traces of the lithographic MCBJs in vacuum are presented in Figure 4.1a. As the junctions are stretched, their conductance decreases from several G_0 to a value below the noise floor of our setup. During this process, the conductance does not evolve

continuously, but it exhibits sudden jumps and plateaus. In junctions exposed to clean toluene the last pronounced plateau repeatedly occurs around 1 G_0 . It is well established that this conductance value corresponds to a single gold atom bridging the gap between the electrodes [24]. Upon further stretching, the conductance of the clean junctions decreases roughly exponentially with occasional jumps and fluctuations. In Au MCBJs, the observation of a plateau at the quantum of conductance is relatively robust and independent of measurement parameters. It is also present in devices that have been exposed to molecular solutions. In addition, many of the breaking traces on these junctions display steps of varying length and height below 1 G_0 . The conductance at these plateaus can exhibit significant fluctuations both at room temperature and at 77 K.

Due to microscopic variations in the contact geometry and the evolution of the conductance a large number of breaking traces has to be acquired and analyzed statistically. We constructed logarithmic conductance histograms (see Chapter 3) from 300 consecutive breaking traces of individual junctions without any data selection. We note that this approach differs from most other experiments. Often, only traces displaying plateaus are used to construct histograms. We have chosen to include all breaking data for two reasons. First, we are interested in the influence of measurement parameters on the behavior of the junctions - a selection of traces might prevent us from drawing valid conclusions. Secondly, we think that conductance noise and jumps are typical of molecular junctions. Traces exhibiting these features should be included in the statistical analysis. We normalized the counts in all bins of the histograms to an equivalent of milliseconds per trace in order to prevent sampling rates from affecting the histograms. This allows for comparisons across different experimental platforms and illustrates the time scales of the breaking process.

The breaking histogram of a typical junction exposed to pure toluene is presented in Figure 4.1b. In contrast to previous results on lithographic MCBJs in solution [2], we systematically observe detectable counts across the entire range below 1 G_0 . The counts are distributed rather uniformly, so that there are no indications for preferred conductance values. This uniform distribution can be rationalized by investigating the breaking traces. When compared to other data, particularly from STM measurements [17, 21], the traces measured in our MCBJs exhibit a much less pronounced conductance drop after the 1 G_0 plateau. Besides, we repeatedly record fluctuations in the regime of vacuum tunneling. We believe that impurities from the solvent can be excluded as a possible cause of this difference. First, control experiments on samples not exposed to any solvent did not lead to a reduction of counts below 1 G_0 . Furthermore, we fused devices exposed to toluene to conductances of more than 40 G_0 to create fresh breaking surfaces. Also in this case, the background signal in the tunneling regime could not be reduced.

We think that the uniform distribution of histogram counts below 1 G_0 must rather be related to the small indentation and the slow breaking of our lithographic MCBJs. Both may have an influence on the micromechanics of their contact area and their breaking behavior. The speed of contact separation in our junctions is on the order of 60 pm/s, which is by a factor of 20 slower than in the experiment reported by González *et al.* [2], and by more than 2 orders of magnitude below typical breaking speeds in STM [3].

During a fast breaking of Au MCBJs, the contact separation usually increases spontane-

ously after cleaving the last gold-gold bond. This can either be due to the relaxation of atomic chains [25] or due to the release of mechanical stress in the banks [26]. In histograms, such a spontaneous opening leads to a depletion in counts in the high tunneling regime. In slow measurements at room-temperature, thermal fluctuations may reduce the probability of forming chains significantly. Furthermore, the gentle deformation of our lithographic MCBJs may prevent mechanical stress in the banks, leading to a more uniform tunneling signal in the breaking histogram. The slow breaking speed may also explain the comparatively small and broad peak at 1 G_0 in our measurements. Thermal fluctuations can limit the lifetime and the statistical signature of the last gold-gold bond. The observed histogram peak height of 40 ms per trace is on the order of the natural lifetime of the gold-gold point contact obtained by Huang *et al.* [3].

We have systematically studied the influence of the measurement parameters on conductance histograms of the model system hexanedithiol. The fusing depth of the HDT-covered junctions in histogram measurements turned out to be a crucial parameter for the detection of molecular features. At room temperature, fusing the MCBJs to $40\ G_0$, i.e., to about 50% of their conductance after fabrication, did not result in a significant increase of the histogram counts below $1\ G_0$ as compared to junctions exposed to clean toluene (see Figure 4.1b). A target conductance of a few G_0 , in contrast, led to increasing difficulties in closing the junctions to high conductances after less than 100 cycles (not shown). Fusing the MCBJs to $20\ G_0$ eventually enabled us to carry out reliable histogram measurements comprising hundreds of breaking curves.

A histogram obtained with these parameters is presented in the center of Figure 4.1b. Compared to the data on clean toluene, the HDT histogram displays a pronounced peak around $7 \cdot 10^{-4} G_0$. It indicates a higher probability of measuring this conductance value in breaking traces, which is usually attributed to the formation of metal-molecule-metal junctions (for a more detailed discussion see the following section). At 77 K, in contrast, fusing the MCBJs to 20 G_0 completely suppresses any peaks in the histograms. A target conductance of 3 G_0 , corresponding to a few atoms only, again leads to signatures of the formation of molecular junctions, represented by a broad peak around $4 \cdot 10^{-4} G_0$.

These observations suggest that single-molecule measurements in vacuum may be limited by the surface density and diffusion of thiols. While insufficient fusing leads to a too dense coverage of the electrodes and prevents them from being fused after a number of cycles, deep indentation reduces the probability of creating single-molecule contacts significantly.

4.4 CONDUCTANCE HISTOGRAMS OF MODEL SYSTEMS

We have used the optimized parameters discussed above in histogram measurements of the molecular model systems hexanedithiol, hexanediamine, benzenedithiol and benzenediamine at room temperature. The junctions were cycled between the open state and $20\ G_0$ in order to increase the chance of trapping molecules during breaking.

Figure 4.2a presents histograms obtained on the substituted alkanes, hexanedithiol and hexanediamine. Histograms obtained for HDT at room temperature displayed a broad peak around $7 \cdot 10^{-4}$ G_0 . Depending on the experiment, peaks below this value could also

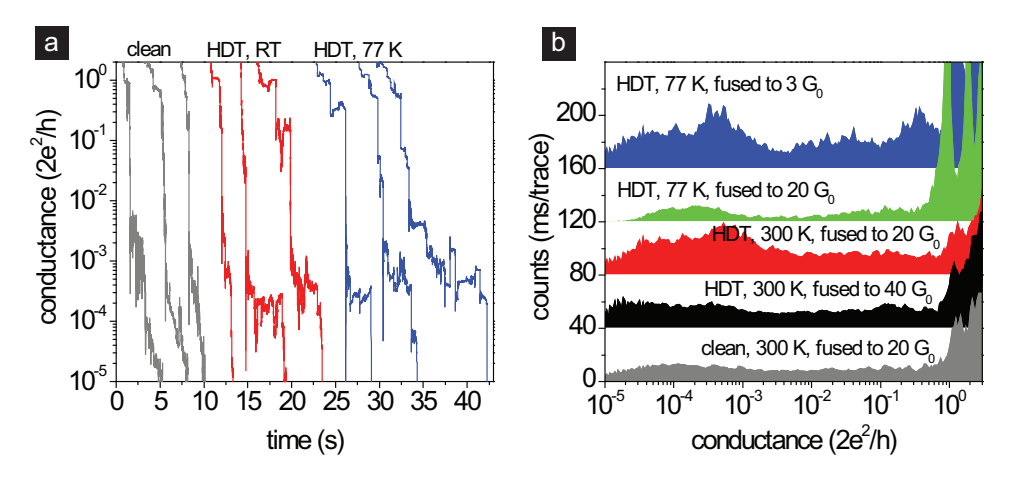


FIGURE 4.1: Breaking characteristics of MCBJs exposed to clean toluene and to solutions of hexanedithiol. The temperature and the fusing depth of the junctions were varied in between the different experiments. The conductance was measured at a bias voltage of 50 mV. (a) Examples of breaking traces of a clean junction at room temperature and of junctions exposed to hexanedithiol. (b) Conductance histograms for different temperatures and fusing depths. Histograms were constructed from 300 subsequent breaking curves using 42 bins per decade. The data are offset by 40 ms/trace for clarity.

be observed. The histogram in Figure 4.2a, for example, contains a series of smaller peaks around $3 \cdot 10^{-5}$, $7 \cdot 10^{-5}$, $1.5 \cdot 10^{-4}$ G_0 .

The presence of more than one peak is not unusual - STM-based experiments on HDT in solution have yielded two peaks at $3\cdot 10^{-4}$ and $1\cdot 10^{-3}$ G_0 [18]. Similar measurements in vacuum even showed 3 different conductance regimes at $3\cdot 10^{-5}$, $2\cdot 10^{-4}$, and $3\cdot 10^{-3}$ G_0 [9]. The conductance observed in our measurement falls well within this range, but there is not a close agreement with one previously published dataset.

Recent theoretical and experimental results shed more light on this difference. In general, the presence of several peaks can be attributed to different molecular conformations or varying contact geometries. Series of peaks corresponding to integer multiples of a basic conductance are sometimes associated with junctions containing several molecules in parallel. Furthermore, density functional theory (DFT)-based simulations and delicate STM-based experiments have indicated that different core and contact geometries of alkanedithiols may give rise to a conductance spread over 2 decades. Li *et al.* attribute most of this spread to conformational changes in the alkane units [27]. This effect can be of foremost importance in the case of sparse monolayers, where a large degree of steric freedom is given. The molecular concentrations and self-assembly times in our work are comparable to those of Li *et al.* [27], who reported a mixture of high and low-coverage phases.

Surprisingly, HDA exhibits a considerably smaller and broader peak than HDT. The conductance of about $4\cdot 10^{-4}~G_0$ is in reasonable agreement with previous reports on HDA, which indicate conductances of $1.2\cdot 10^{-4}$ and $3\cdot 10^{-4}~G_0$ [18, 21]. However, the large peak width is in contrast to the results obtained by Venkataraman *et al.*, who observed a reduction in spread of the conductance of amines with respect to thiols [21].

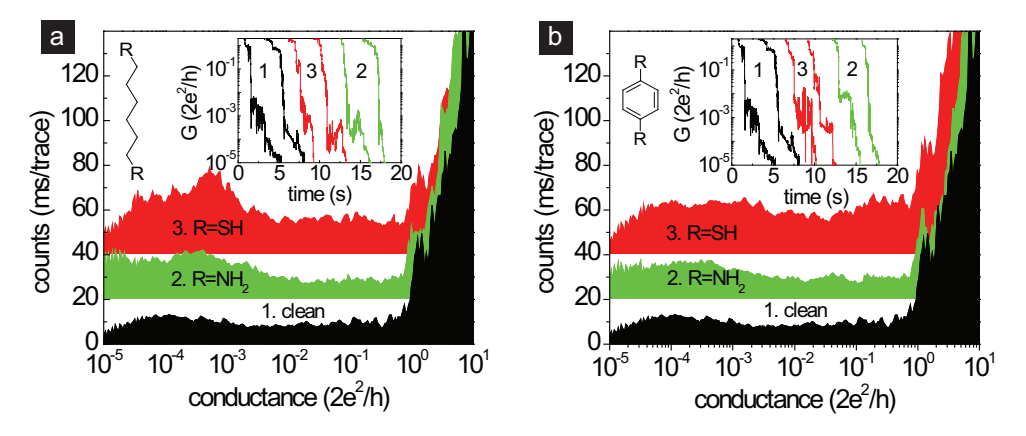


FIGURE 4.2: Conductance histograms of MCBJs exposed to clean toluene and to solutions of the molecular model systems. All histograms were constructed from 300 breaking curves without any selection using 42 bins/decade. The inset shows examples of the conductance traces measured during breaking. (a) Conductance histograms of the substituted hexanes. (b) Conductance histograms of the substituted benzenes.

We believe that this difference is due to the different experimental parameters. Recent STM experiments at varying breaking speeds in solution suggest that bond re-formation after desorption can increase the lifetime of single-molecule junctions [3]. This effect may be suppressed in the absence of a stabilizing solvent and at a sparse surface coverage. Furthermore, simulations and experiments on amine junctions have indicated that these break faster upon stretching than thiols [5, 22]. In fact, the Au-S bond is even more stable than the Au-Au bond itself, allowing for the deformation of gold electrodes during pulling [28]. In the case of a measurement limited by the lifetime of a bond, the signature of amines in histograms will be much smaller than the one of thiols. This could be crucial in lithographic MCBJs, which are broken at a very slow speed. The slow breaking leads to a large statistical weight of counts from the vacuum-tunneling regime (see Chapter 3) and an enhanced histogram background below 1 G_0 , which may obscure the signature of molecular conductance steps.

In histograms of MCBJs exposed to benzenedithiol (see Figure 4.2b), the entire conductance regime below 1 G_0 displayed enhanced counts. The probability distribution also showed variation between different experiments. Above an enhanced background of counts, small peaks in the region between 0.1 and 1 G_0 and just above 10^{-3} G_0 are visible. Overall, these are much less pronounced than the ones observed in the histograms of HDT.

The previously reported peak at 0.011 G_0 [29] is not evident in our data. Nevertheless, the high conductances are in the range of previous data from MCBJ measurements [19], and the small peak around $3 \cdot 10^{-3} G_0$ agrees with recent results from STM measurements [17]. However, the broad distribution of junction conductances clearly dominates the histogram. A similar spread in conductance values has been observed by Ulrich *et al.* [17]. It was attributed to geometrical variations in the metal-molecule junctions. We think that

both the binding motif of the thiol groups and possible interactions between the benzene core and the gold electrodes contribute to the variation in our data. In the absence of a stabilizing solvent, even junction configurations with a molecule lying flat on the gold surface are conceivable. Due to the interaction of π -orbitals with the electrodes their electronic coupling could differ considerably from that of upright molecules, leading to different conductance values.

Similar to the measurements on the hexane derivatives, the use of amino anchoring groups did not lead to clearer peaks in the histogram measurements of benzenediamine (see Figure 4.2b). In its conductance histogram the region below a few $10^{-3}\ G_0$ exhibits increased counts, but it misses a pronounced peak structure. This is different from previous data obtained in solution [21], but in agreement with our measurements on HDA. Again, the absence of a solvent and a fast rupture of the metal-molecule bond must have reduced the probability of forming stable molecular junctions, which are a prerequisite for pronounced peaks in the histograms.

4.5 IV MEASUREMENTS ON BENZENE DERIVATIVES

During the stepwise breaking and making of MCBJs exposed to benzenedithiol and benzenediamine we repeatedly observed series of reproducible IV curves that displayed a low conductance around zero bias and a step-like increase in current at higher bias voltages. Within these series, which typically lasted for a few micrometers of bending, both the shape and the current level of the IV characteristics remained similar.

An example of such a series of reproducible current-voltage characteristics is presented in Figure 4.3a. For a large contact separation, the junction exhibits rather smooth IVs with low currents. As the electrodes approach in discrete steps, the measurement yields a group of IV curves that barely change upon pushing. They are marked by a distinct nonlinearity, i.e., a suppression of the junction current in the bias window from -0.3 V to 0.2 V. After several steps in the making of the junction, this series ends and a second group of nonlinear characteristics is measured, which again exhibit a current suppression around zero bias. Current levels in this series are considerably larger than in the first one, and the conductance gap differs slightly. Upon moving the electrodes closer together, the gap structure is lost. Instead, smooth IV curves with high current levels are measured. These high-conductance curves saturate around 4 μ A (not shown in the graph), corresponding to the compliance of the measurement electronics. It is important to note that the conductance of these junctions is below 1 G_0 and their characteristics are slightly superlinear. Only after fusing the MCBJ further a contact with a conductance above 1 G_0 is formed.

Control experiments on MCBJs exposed to pure toluene did not show reproducible IV-characteristics with step-like increases in current. The low-bias conductance of these junctions evolved rather steadily in the interval from less than $5 \cdot 10^{-6} \ G_0$ to $2.1 \ G_0$. An example of this evolution is given in Figure 4.3b. As the junction is fused, the maximum current in the smooth IV characteristics slowly increases from the nA-range to about $4 \ \mu A$. The observation of reproducible, nonlinear IVs during the making of MCBJs exposed to organic molecules agrees well with recent statistical IV measurements by Lörtscher et al. [1]. In their experiments, three different regimes of transport were identified: conduc-

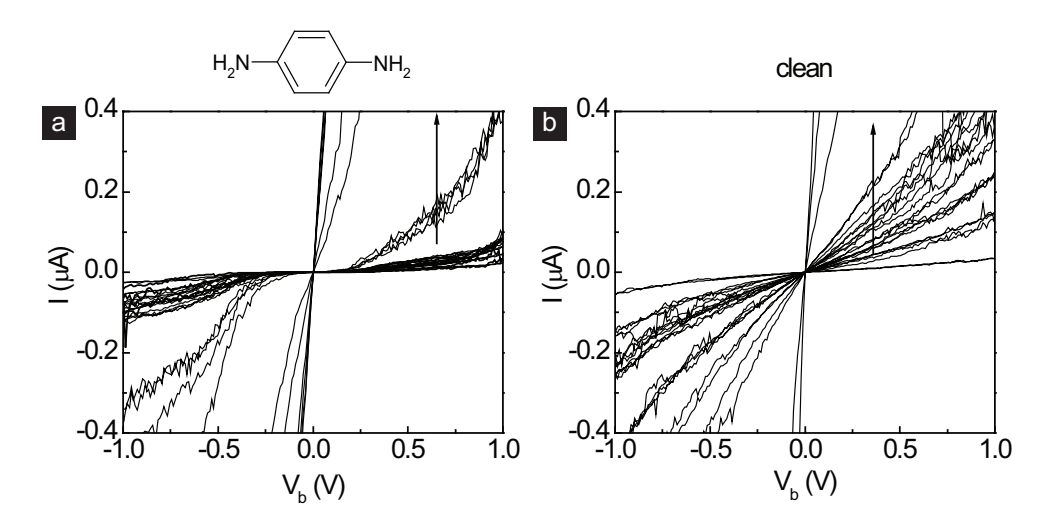


FIGURE 4.3: Consecutive IV traces obtained during the stepwise closing of lithographic MCBJs at room temperature. The change in electrode distance between the steps was on the order of 15 pm. The arrows mark the time evolution of the characteristics. (a) Consecutive IVs obtained during the closing of a junction exposed to BDA in toluene. Groups of nonlinear characteristics can be observed. (b) Smooth IV curves typical of junctions exposed to clean toluene. The current increases rather steadily with decreasing gap size.

tion through vacuum (described by smooth tunneling characteristics with low currents), transport through a single molecule (marked by highly nonlinear IV characteristics), and a fused metal-metal connection (with an ohmic bias response). The transition between these regimes was very abrupt, with signatures of single-molecule junctions appearing exclusively during the making of the MCBJ. In our MCBJs, in contrast, reproducible, nonlinear IVs could be measured both during breaking and making. Furthermore, the transition between the different regimes was less systematic and less pronounced.

Both differences may be related to our method of molecule deposition. While Lörtscher *et al.* [1] applied BDT to open junctions, we carried out the self-assembly before breaking. This may lead to different adsorption geometries and surface densities of the molecular (sub-)monolayer in the contact area, and possibly a larger variation in the probed metal-molecule-metal junctions.

It is important to note that the IV characteristics of junctions exposed to BDT and BDA were not always symmetric. Generally, the presence of asymmetric IVs agrees with previous reports on single-molecule measurements [1, 30]. Within the series of reproducible IV characteristics the asymmetry did not change significantly, nor did the overall current level. Therefore, the asymmetric IVs may be attributed to two dissimilar metal-molecule bonds rather than to a molecule chemisorbed to a single electrode only. In the latter case the electronic coupling to the other electrode would be characterized by vacuum tunneling, leading to highly stretching-dependent IV characteristics.

We have analyzed data from hundreds of *IV* measurements on MCBJs exposed to BDT and BDA and identified series of reproducible characteristics. Figure 4.4 presents typical

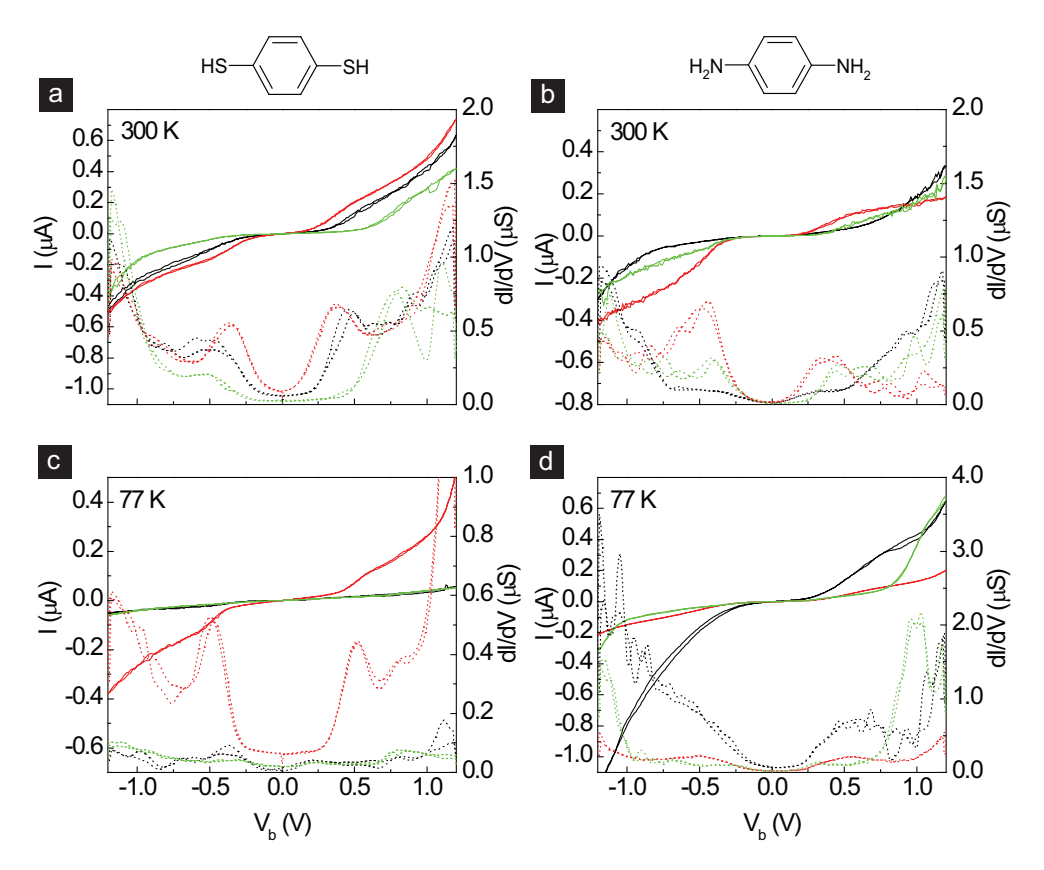


FIGURE 4.4: Typical nonlinear IV characteristics (solid lines) of MCBJs exposed to benzenedithiol and benzenediamine. The differential conductance dI/dV (dotted lines) was calculated by smoothing and differentiating the measurement data. The left side displays IV characteristics that remained stable during the stretching of junctions containing BDT at (a) room temperature and (c) 77 K. The right graphs present typical IV traces of MCBJs containing BDA at (b) room temperature and (d) 77 K.

IV characteristics obtained on several junctions at room temperature and at 77 K together with their respective numerical dI/dV spectra. At room temperature, junctions containing benzenedithiol repeatedly displayed conductance gaps at low bias. Three examples of such characteristics are presented in Figure 4.4a. In this set, the black curve represents a junction with a conductance gap of 1.0 V, framed by two peaks at -0.5 and +0.5 V in the numerical dI/dV spectrum. This gap size is close to the average value in our measurements, which was around 0.9 V. However, the conductance gaps in dI/dV showed considerable variation between different IV series, ranging from 0.6 V to 1.6 V. Furthermore, the junction characteristics were not always symmetric. In the graph, this variation is exemplified by the green and the red curves.

The nonlinear IV characteristics observed at 77 K differ from the ones at room temperature. Measurements typically yielded smaller conductance gaps on the order of 0.6 V,

similar to the black and green characteristics in Figure 4.4c. Occasionally, larger gaps and different current levels could be observed. With two dI/dV peaks located around ± 0.5 V the red IV curve in the graph illustrates this variation.

The BDT characteristics presented in parts a and c of Figure 4.4 are markedly different from the ones reported by Reed $et\ al.\ [31]$. In our measurements, the differential conductance beyond the first peak in dI/dV is by one order of magnitude larger. Furthermore, the typical gap sizes are by a factor of 2.5 smaller than the ones in reference [31]. Our room-temperature results are, however, in good agreement with more recent data of Lörtscher $et\ al.\ [1]$. At 250 K, these authors reported reproducible IV characteristics with an average conductance gap on the order of 0.9 V. In the same study, they obtained a conductance gap of about 0.6 V at 77 K, again in good agreement with the average value in our measurements. However, the wide gap indicated in Figure 4.4c differs from the results in reference [1].

The presence of varying IV characteristics in single-molecule measurements may be related to changes in electronic coupling or band offset [32, 33]. Computational transport studies on BDT junctions have yielded a variation in the position of the electronic levels of the molecule by more than 1 eV [22, 33–35]. Furthermore, it has been suggested that single-molecule transport is influenced by the stretching of the molecule [36], the non-equilibrium situation established by finite bias voltages [35], and the adsorption motif of the thiol [22]. However, the quantitative agreement between theoretical and experimental data is generally too limited for a detailed comparison.

Interestingly, the junctions formed in our experiments appear to be more stable than the ones reported earlier. Lörtscher *et al.* [1] were only able to establish stable metal-BDT-metal junctions at temperatures of 250 K and below. In our experiments, reproducible characteristics could even be measured at room temperature. Furthermore, the junction currents we observed were by a factor of more than 10 larger. While the similarity in conductance gaps suggests a comparable band lineup of the BDT, the current and stability data support a larger metal-molecule coupling compared to the experiments of Lörtscher *et al.* [1]. Regarding the variability of the conductance observed in the histogram measurements on BDT, the signature of many possible junction configurations in *IV* measurements is not surprising.

Measurements on benzenediamine at room temperature revealed conductance gaps on the order of 0.9 V. Typical *IV* curves are presented in parts b and d of Figure 4.4. The gaps show a spread similar to the one in BDT junctions. In contrast to BDT, the gap sizes for BDA at 77 K are not systematically smaller than the ones at room temperature.

In a recent theoretical study motivated by the STM-based measurements in reference [21], Quek *et al.* [23] calculated the transmission spectrum of various configurations of BDA between gold electrodes. Their simulations yield an energy difference of 3 eV between the gold Fermi level and the highest occupied molecular orbital (HOMO) of the BDA. In a second study of BDA in gold break junctions, the first molecular level was located at about 1.5 eV from the Fermi energy [22]. The observation of a conductance gap around 0.9 V supports a very different band lineup in our experiments. However, a direct comparison with the results by Venkataraman *et al.* [21] and with calculations should be made with care, as histograms are recorded at low bias. Therefore, they may probe other configurations than

the ones that are stable over the wide voltage range in our IV measurements [37]. Moreover, the position of the energy level in the calculations may not be interpreted directly in terms of the gap in IV as levels can shift and broaden under the influence of the applied bias.

4.6 SUMMARY AND CONCLUSIONS

We have studied the electronic properties of single prototypical molecules using lithographic MCBJs in vacuum. Hexane and benzene with thiol and amino anchoring groups were applied using a self-assembly scheme before breaking.

Histogram measurements of HDT with different parameters suggest that the resulting concentration of molecules in the junction is low and governed by surface diffusion. Using fusing depths of 20 G_0 at room temperature and 3 G_0 at 77 K, it was possible to reliably form single-molecule junctions of HDT.

In contrast to recent STM-based experiments in solution [21], the exchange of thiol for amino anchoring groups did not reduce the spread in molecular conductance, neither for hexane nor for benzene cores. Supposedly, the slow breaking and the absence of a surrounding solvent are detrimental for the measurement of conductance histograms. Recent theoretical and experimental data suggest that the amine bond breaks fast under applied stress. Thiols, in contrast, are able to maintain contact upon stretching of the junctions. At low surface coverage and in the absence of bond-reformation, as in MCBJ experiments in vacuum, the lifetime of metal-molecule bond may be the determining factor in conductance measurements. In the case of short-lived junctions and slow breaking, histograms will be dominated by a uniform background from vacuum tunneling.

Nevertheless, junctions of benzenedithiol and benzenediamine displayed series of reproducible, nonlinear IV characteristics during stepwise bending. In contrast to recent BDT measurements by Lörtscher $et\ al.$ [1], which were limited to a maximum temperature of 250 K, we were able to measure stable IVs at 300 K. The observed conductance gaps of BDT-junctions were largely in agreement with their results. However, a larger spread in gap sizes and a difference in junction currents indicate the probing of several metal-molecule-metal configurations. The obtained IV characteristics of BDA-junctions at room temperature and at 77 K also displayed some variation, but no systematic difference in conductance gaps at room temperature and 77 K.

In conclusion, the experimental parameters are of large importance for single-molecule measurements with lithographic MCBJs in vacuum. The molecular signature in conductance histograms may be limited by the low surface concentration of molecules and the lifetime of the molecular bond. Furthermore, both histograms and IV measurements may exhibit considerable variation due to the probing of different junction geometries in the absence of a stabilizing solvent.

REFERENCES

[1] E. Lörtscher, H. B. Weber, and H. Riel, *Statistical Approach to Investigating Transport through Single Molecules*, Phys. Rev. Lett. **98**, 176807 (2007).

References 79

[2] M. T. González, S. Wu, R. Huber, S. J. van der Molen, C. Schönenberger, and M. Calame, *Electrical Conductance of Molecular Junctions by a Robust Statistical Analysis*, Nano Lett. **6**, 2238 (2006).

- [3] Z. Huang, F. Chen, P. A. Bennett, and N. Tao, *Single Molecule Junctions Formed via Au-Thiol Contact: Stability and Breakdown Mechanism*, J. Am. Chem. Soc. **129**, 13225 (2007).
- [4] M. Tsutsui, K. Shoji, M. Taniguchi, and T. Kawai, *Formation and Self-Breaking Mechanism of Stable Atom-Sized Junctions*, Nano Lett. **8**, 345 (2008).
- [5] Y. S. Park, A. C. Whalley, M. Kamenetska, M. L. Steigerwald, M. S. Hybertsen, C. Nuckolls, and L. Venkataraman, Contact Chemistry and Single-Molecule Conductance: A Comparison of Phosphines, Methyl Sulfides, and Amines, J. Am. Chem. Soc. 129, 15768 (2007).
- [6] J. C. Love, L. A. Estroff, J. K. Kriebel, R. G. Nuzzo, and G. M. Whitesides, *Self-Assembled Monolayers of Thiolates on Metals as a Form of Nanotechnology*, Chem. Rev. **105**, 1103 (2005).
- [7] D. Losic, J. G. Shapter, and J. J. Gooding, Influence of Surface Topography on Alkanethiol SAMs Assembled from Solution and by Microcontact Printing, Langmuir 17, 3307 (2001).
- [8] M. Kawasaki, T. Sato, T. Tanaka, and K. Takao, *Rapid Self-Assembly of Alkanethiol Monolayers on Sputter-Grown Au(111)*, Langmuir **16**, 1719 (2000).
- [9] M. Fujihira, M. Suzuki, S. Fujii, and A. Nishikawa, *Currents through single molecular junction of Au/hexanedithiolate/Au measured by repeated formation of break junction in STM under UHV: Effects of conformational change in an alkylene chain from gauche to trans and binding sites of thiolates on gold, Phys. Chem. Chem. Phys. 8*, 3876 (2006).
- [10] H. Basch, R. Cohen, and M. A. Ratner, *Interface Geometry and Molecular Junction Conductance: Geometric Fluctuation and Stochastic Switching*, Nano Lett. **5**, 1668 (2005).
- [11] J. Tomfohr and O. F. Sankey, *Theoretical analysis of electron transport through organic molecules*, J. Chem. Phys. **120**, 1542 (2004).
- [12] K. Müller, Effect of the atomic configuration of gold electrodes on the electrical conduction of alkanedithiol molecules, Phys. Rev. B **73**, 045403 (2006).
- [13] B. Xu and N. J. Tao, Measurement of Single-Molecule Resistance by Repeated Formation of Molecular Junctions, Science **301**, 1221 (2003).
- [14] W. Haiss, R. J. Nichols, H. van Zalinge, S. J. Higgins, D. Bethell, and D. J. Schiffrin, *Measurement of single molecule conductivity using the spontaneous formation of molecular wires*, Phys. Chem. Chem. Phys. **6**, 4330 (2004).

- [15] A. Nishikawa, J. Tobita, Y. Kato, S. Fujii, M. Suzuki, and M. Fujihira, *Accurate determination of multiple sets of single molecular conductance of Au/1,6-hexanedithiol/Au break junctions by ultra-high vacuum-scanning tunneling microscope and analyses of individual current-separation curves*, Nanotechnology **18**, 424005 (2007).
- [16] S.-Y. Jang, P. Reddy, A. Majumdar, and R. A. Segalman, *Interpretation of Stochastic Events in Single Molecule Conductance Measurements*, Nano Lett. **6**, 2362 (2006).
- [17] J. Ulrich, D. Esrail, W. Pontius, L. Venkataraman, D. Millar, and L. H. Doerrer, *Variability of Conductance in Molecular Junctions*, J. Phys. Chem. B **110**, 2462 (2006).
- [18] F. Chen, X. Li, J. Hihath, Z. Huang, and N. Tao, Effect of Anchoring Groups on Single-Molecule Conductance: Comparative Study of Thiol-, Amine-, and Carboxylic-Acid-Terminated Molecules, J. Am. Chem. Soc. 128, 15874 (2006).
- [19] M. Tsutsui, Y. Teramae, S. Kurokawa, and A. Sakai, *High-conductance states of single benzenedithiol molecules*, Appl. Phys. Lett. **89**, 163111 (2006).
- [20] J. He, O. Sankey, M. Lee, N. Tao, X. Li, and S. Lindsay, *Measuring single molecule conductance with break junctions*, Faraday Discuss. **131**, 145 (2005).
- [21] L. Venkataraman, J. E. Klare, I. W. Tam, C. Nuckolls, M. S. Hybertsen, and M. L. Steiger-wald, Single-Molecule Circuits with Well-Defined Molecular Conductance, Nano Lett. 6, 458 (2006).
- [22] Z. Li and D. S. Kosov, *Nature of well-defined conductance of amine-anchored molecular junctions: Density functional calculations*, Phys. Rev. B **76**, 035415 (2007).
- [23] S. Y. Quek, L. Venkataraman, H. J. Choi, S. G. Louie, M. S. Hybertsen, and J. B. Neaton, Amine-Gold Linked Single-Molecule Junctions: Experiment and Theory, Nano Lett. 7, 3477 (2007).
- [24] N. Agraït, A. L. Yeyati, and J. M. van Ruitenbeek, Quantum properties of atomic-sized conductors, Phys. Rept. 377, 81 (2003).
- [25] A. I. Yanson, G. R. Bollinger, H. E. van den Brom, N. Agraït, and J. M. van Ruitenbeek, *Formation and manipulation of a metallic wire of single gold atoms*, Nature **395**, 783 (1998).
- [26] G. Rubio, N. Agraït, and S. Vieira, Atomic-Sized Metallic Contacts: Mechanical Properties and Electronic Transport, Phys. Rev. Lett. 76, 2302 (1996).
- [27] C. Li, I. Pobelov, T. Wandlowski, A. Bagrets, A. Arnold, and F. Evers, *Charge Transport in Single Au/alkanedithiol/Au Junctions: Coordination Geometries and Conformational Degrees of Freedom*, J. Am. Chem. Soc. **130**, 318 (2008).
- [28] B. Xu, X. Xiao, and N. J. Tao, *Measurements of Single-Molecule Electromechanical Properties*, J. Am. Chem. Soc. **125**, 16164 (2003).

REFERENCES 81

[29] X. Xiao, B. Xu, and N. J. Tao, Measurement of Single Molecule Conductance: Benzenedithiol and Benzenedimethanethiol, Nano Lett. 4, 267 (2004).

- [30] J. Reichert, R. Ochs, D. Beckmann, H. B. Weber, M. Mayor, and H. v. Löhneysen, *Driving Current through Single Organic Molecules*, Phys. Rev. Lett. **88**, 176804 (2002).
- [31] M. A. Reed, C. Zhou, C. J. Muller, T. P. Burgin, and J. M. Tour, *Conductance of a Molecular Junction*, Science **278**, 252 (1997).
- [32] A. Troisi and M. A. Ratner, *Molecular Signatures in the Transport Properties of Molecular Wire Junctions: What Makes a Junction 'Molecular'?*, Small **2**, 172 (2006).
- [33] Y. Xue and M. A. Ratner, *Microscopic study of electrical transport through individual molecules with metallic contacts. I. Band lineup, voltage drop, and high-field transport*, Phys. Rev. B **68**, 115406 (2003).
- [34] R. Stadler, K. S. Thygesen, and K. W. Jakobsen, *An ab inito study of electron transport through nitrobenzene: the influence of leads and contacts*, Nanotechnology **16**, S155 (2005).
- [35] A. Arnold, F. Weigend, and F. Evers, *Quantum chemistry calculations for molecules coupled to reservoirs: Formalism, implementation, and application to benzenedithiol,* J. Chem. Phys. **126**, 174101 (2007).
- [36] L. Romaner, G. Heimel, M. Gruber, J.-L. Brédas, and E. Zojer, *Stretching and Breaking of a Molecular Junction*, Small **2**, 1468 (2006).
- [37] J. R. Widawsky, M. Kamenetska, J. Klare, C. Nuckolls, M. L. Steigerwald, M. S. Hybertsen, and L. Venkataraman, *Measurement of voltage-dependent electronic transport across amine-linked single-molecular-wire junctions*, Nanotechnology 20, 4009 (2009).

FULLERENE-BASED ANCHORING GROUPS FOR MOLECULAR ELECTRONICS

In this chapter, we present results on a new fullerene-based anchoring group for molecular electronics. Using lithographic mechanically controllable break junctions in vacuum we have determined the conductance and the stability of single-molecule junctions of 1,4-bis(fullero[c]pyrrolidin-1-yl)benzene. We find that the compound can be self-assembled from solution and that it has a low-bias conductance around $3\cdot 10^{-4}\,G_0$. Compared to 1,4-benzenedithiol the fullerene-anchored molecule exhibits a considerably lower conductance spread. In addition, the signature of the new compound in histograms is larger than that of 1,4-benzenediamine, probably owing to a more stable adsorption motif. Statistical analyses of the breaking of the junctions confirm the stability of the fullerene-gold bond.

Parts of this chapter have been published as C. A. Martin, D. Ding, J. K. Sørensen, T. Bjørnholm, J. M. van Ruitenbeek, and H. S. J. van der Zant, J. Am. Chem. Soc. **130**, 13198 (2008).

5.1 Introduction

Self-assembly from solution with stable chemical anchoring is an important step in the robust formation of single-molecule junctions. To date, thiol moieties have been used extensively to attach single molecules to gold electrodes [1, 2]. However, the thiol-gold bond exhibits variations and fluctuations that are reflected in the electronic properties of molecular junctions [3–5]. Only very recently, amino groups have successfully been applied in solution-based break junction experiments. Their binding motif reduced the conductance spread of single-molecule junctions significantly and allowed for more systematic studies of structure-property relationships [6, 7]. However, we found that the signature of amines in mechanically controllable break junctions in vacuum is small (see Chapter 4), probably due to the weak amine-gold bond.

To attain larger junction stabilities and to minimize fluctuations due to atomic details at the anchoring site we have designed and synthesized a linear and rigid C_{60} -capped molecule (see Figure 5.1). With their high symmetry and their affinity for noble metals, fullerenes are very interesting candidates for anchoring. Stable C_{60} adlayers have been deposited from various solvents [8, 9]. Furthermore, C_{60} is known to hybridize strongly with gold surfaces [10], leading to single-molecule conductances on the order of one tenth of the conductance quantum G_0 [11]. As an anchoring moiety, C_{60} may lead to a significant increase in the contact area with the electrodes and to a shift of the limiting barriers for electronic transport from the molecule-gold contact to the stable covalent bonds of the pyrrolidine moieties that connect the C_{60} with the molecular backbone (see Figure 5.1). This can also be advantageous for comparisons with theoretical models: In the extended molecule picture [12], the strong hybridization with the gold allows the fullerene anchors to be treated as effective electrodes, leading to well-defined charge injection into the molecular core.

To test the C_{60} anchoring we have compared the electrical characteristics of the model compound 1,4-bis(fullero[c]pyrrolidin-1-yl)benzene (BDC60) to those of 1,4-benzenediamine (BDA) and 1,4-benzenedithiol (BDT). Using lithographic mechanically controllable break junctions (MCBJs) we have studied both low-bias conductances and junction stabilities.

5.2 MOLECULAR DESIGN AND SYNTHESIS (J. K. SØRENSEN AND T. BJØRNHOLM, UNIVERSITY OF COPENHAGEN)

The C_{60} -anchored molecule (1,4-bis(fullero[c]pyrrolidin-1-yl)benzene) was synthesized via [2+3]cycloaddition reaction of an in situ generated azomethine ylide to a fullerene carbon-carbon double bond. This reaction is known as the Prato-reaction [13].

N,N'-(1,4-phenylene)bisglycine (16 mg, 0.07 mmol) and paraformaldehyde (13 mg, 0.4 mmol) was sonicated in 1,2-dichlorobenzene (7 mL) for ten minutes. [60]Fullerene (630 mg, 0.88 mmol) was dissolved in 1,2-dichlorobenzene (50 mL) and the suspension of paraformaldehyde and the bisglycine was added, after which the reaction mixture was refluxed under an atmosphere of N_2 for six hours. Purification was achieved by repeated precipitation (heptane added to the 1,2-dichlorobenzene fraction) followed by Soxhlet extrac-

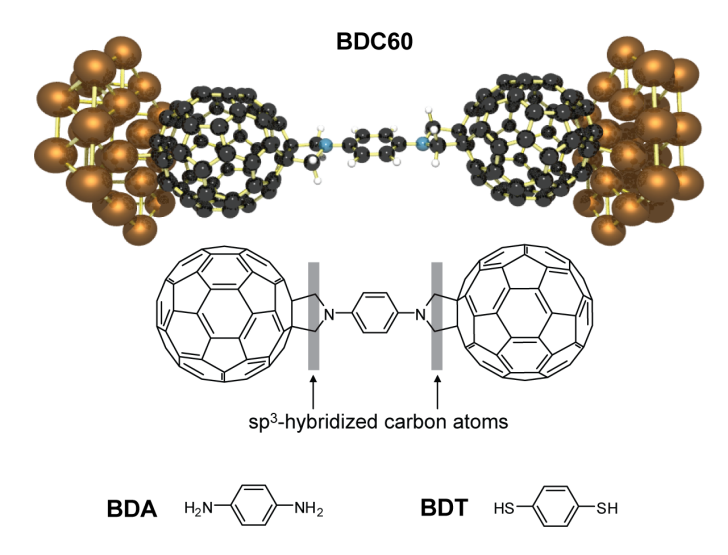


FIGURE 5.1: Molecular structures of the new fullerene-anchored molecule and the benzenedithiol and benzenediamine references. The upper part presents a rendering of a BDC60 molecule between two gold electrodes (courtesy of Jos Seldenthuis, TU Delft).

tion (1,2-dichlorobenzene). After three of such cycles, the product was further purified by column chromatography (SiO2, decalin/1,2-dichlorobenzene gradient starting at 50:50, ending at 20:80). Yield: 30 mg, 28 % (based on the bisglycine, which was the limiting compound). $^1\text{H-NMR}$ (300 MHz): δ 5.26 (s, 8H), 7.51 (s, 4H). MALDI-MS: m/z 1600 (M $^-$), 880 (retro-Prato fragment), Mp > 500°C.

Figure 5.2 presents the UV/vis absorption spectra of BDC60 and two reference species for the core and anchoring moieties, respectively. Within the range of the measurement, the absorption spectrum of BDC60 is in good agreement with a simple sum of the spectra of the individual fulleropyrrolidine and phenylenediamine moieties. These results suggest that the transition dipole moments of the subunits of the BDC60 molecule are hardly altered with respect to the free reference species. Furthermore, the sum spectrum and the spectrum of the fullerene-anchored molecule hardly differ for wavelengths above 450 nm or photon energies below 2.75 eV, respectively (see inset in Figure 5.2). The absence of an absorption band at low energies is consistent with the molecular design. It leads to an electronic decoupling of the π -conjugated system of the benzene core from that of the anchoring groups and prevents the formation of an extended molecular orbital.

5.3 EXPERIMENTAL DETAILS

The MCBJ devices were fabricated according to the process described in Chapter 3. Before the conductance measurements we rinsed each device in the pure solvent (toluene or 1,2-dichlorobenzene, respectively) and placed a small drop of the molecular solution on the area of the junctions. The 1,4-bis(fullero[c]pyrrolidin-1-yl)benzene was self-assembled

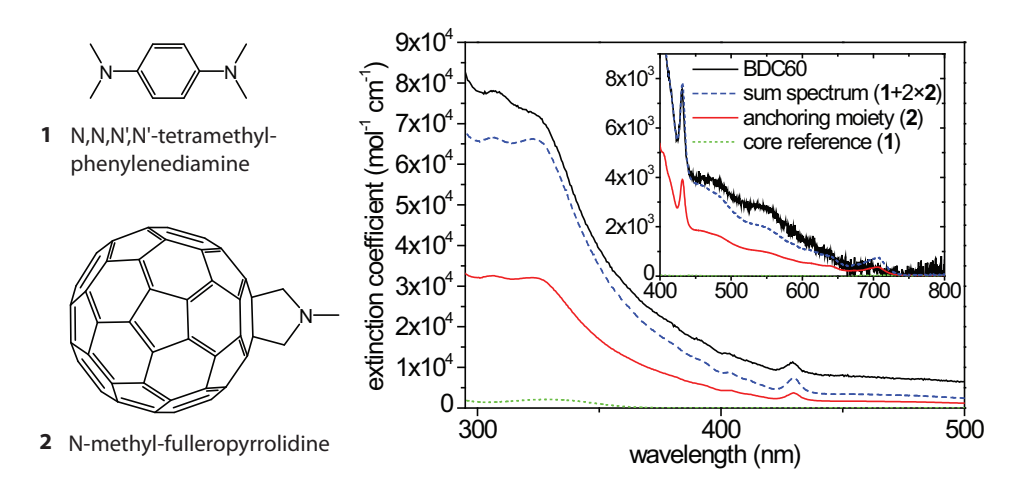


FIGURE 5.2: UV/vis absorption spectra of the fullerene-anchored molecule and two reference species in decalin and 1,2-dichlorobenzene (inset). The data are courtesy of Jeppe Fock and Jakob Kryger Sørensen, University of Copenhagen. The sum spectrum was constructed by doubling the spectrum of the anchoring moiety and adding the spectrum of tetramethyl-phenylenediamine.

from a saturated solution in 1,2-dichlorobenzene (Aldrich, HPLC grade). The two other species, 1,4-benzenedithiol (Tokyo Chemical Industry) and 1,4-benzenediamine (Aldrich), were dissolved in toluene (Aldrich, HPLC grade) at concentrations around 1 mmol/l. Self-assembly times for all molecules were 1 to 2 minutes. After self-assembly, the devices were again rinsed thoroughly in pure solvent. All glassware that was used in the preparation of the molecular solutions was cleaned extensively (see Chapter 4 for details of the protocol). Furthermore, the pure solvent for each experiment was bubbled with nitrogen for at least 30 min in order to expel dissolved oxygen.

All measurements were carried out in a vacuum of about 10^{-5} mbar and at room temperature. During the acquisition of conductance traces the flexible MCBJ substrates were bent at a speed of $2~\mu m/s$. With a typical displacement ratio of $3 \cdot 10^{-5}$ for the devices in this set of experiments, the bending leads to a stretching of the electrodes on the order of 60 pm/s. In order to acquire hundreds of breaking curves the junctions were cycled repeatedly between the fused and the open state, given by a conductance above 20 and below $10^{-5}~G_0$, respectively. The complete opening of the contacts was guaranteed by an additional bending of 50 μ m after the conductance had crossed the lower boundary of this conductance interval. The fusing to $20~G_0$, at the other end of the scale, ensured the atomic reconfiguration of the contacts after each cycle. We collected all conductance traces consecutively on individual junctions. All data were evaluated statistically using 30 bins per decade of conductance.

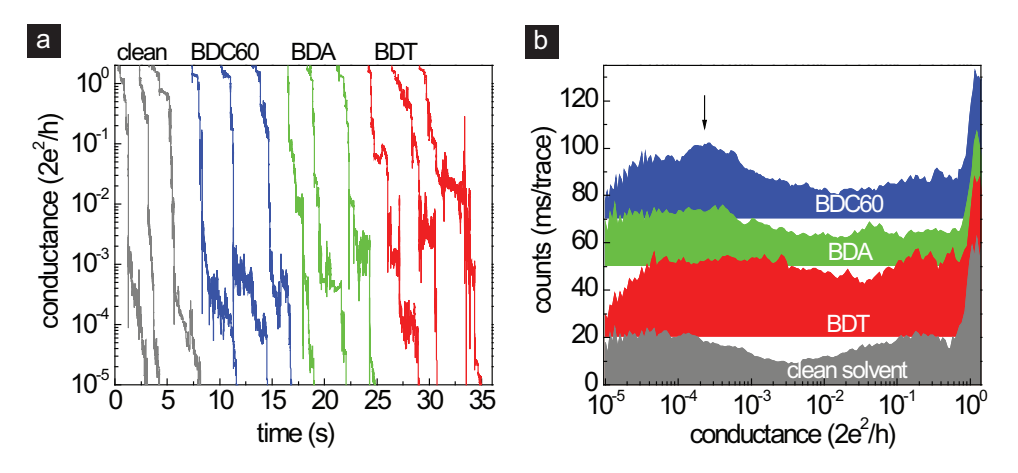


FIGURE 5.3: Breaking characteristics of junctions exposed to clean solvent and to solutions of the benzene derivatives at a dc bias of 50 mV and at room temperature. (a) Examples of conductance traces during breaking. (b) Conductance histograms on a semilog scale, constructed from 400 consecutive traces. The arrow marks the typical junction conductance of BDC60. All curves are offset for clarity. Colors in subfigure a correspond to those in subfigure b.

5.4 HISTOGRAM MEASUREMENTS

Figure 5.3a presents breaking traces of the lithographic MCBJs. As the bending of the substrates is increased, the junctions are stretched and their conductance decreases from several conductance quanta to a value below the noise floor of our setup. Nearly all breaking traces exhibit a plateau around 1 G_0 , which corresponds to a single gold atom bridging the gap between the electrodes. Below 1 G_0 , junctions that have been exposed to pure solvents display a jump out of contact followed by a roughly exponential decay upon stretching, typical of vacuum tunneling. The self-assembly of molecules on the junctions, in contrast, leads to pronounced plateaus in the sub- G_0 regime. These can be attributed to conduction through individual molecules bridging the gap between the gold electrodes [14]. The statistical spread in plateau shapes and positions can be captured by constructing logarithmic conductance histograms [15] from hundreds of breaking traces (see Figure 5.3b). Histograms of junctions exposed to clean solvents typically exhibit a low and rather smooth background below 1 G_0 . Deviations from the expected flat signature of vacuum tunneling may be due to the slow breaking in vacuum (see Chapter 4). Histograms of BDC60, in contrast, display a peak around $3 \cdot 10^{-4}$ G_0 , which we attribute to junctions of the fullereneanchored molecule. Its signature is more pronounced than that of both other benzene derivatives. For benzenediamine, faint features around $4 \cdot 10^{-4}$ G_0 may be observed. Histograms of benzenedithiol do not show a clear structure but increased counts across the entire conductance range, indicating a large variation in junction conductance.

To investigate the stability of the new anchoring mode further we have compared the breaking dynamics of BDC60-junctions to those of the other benzene derivatives. Re-

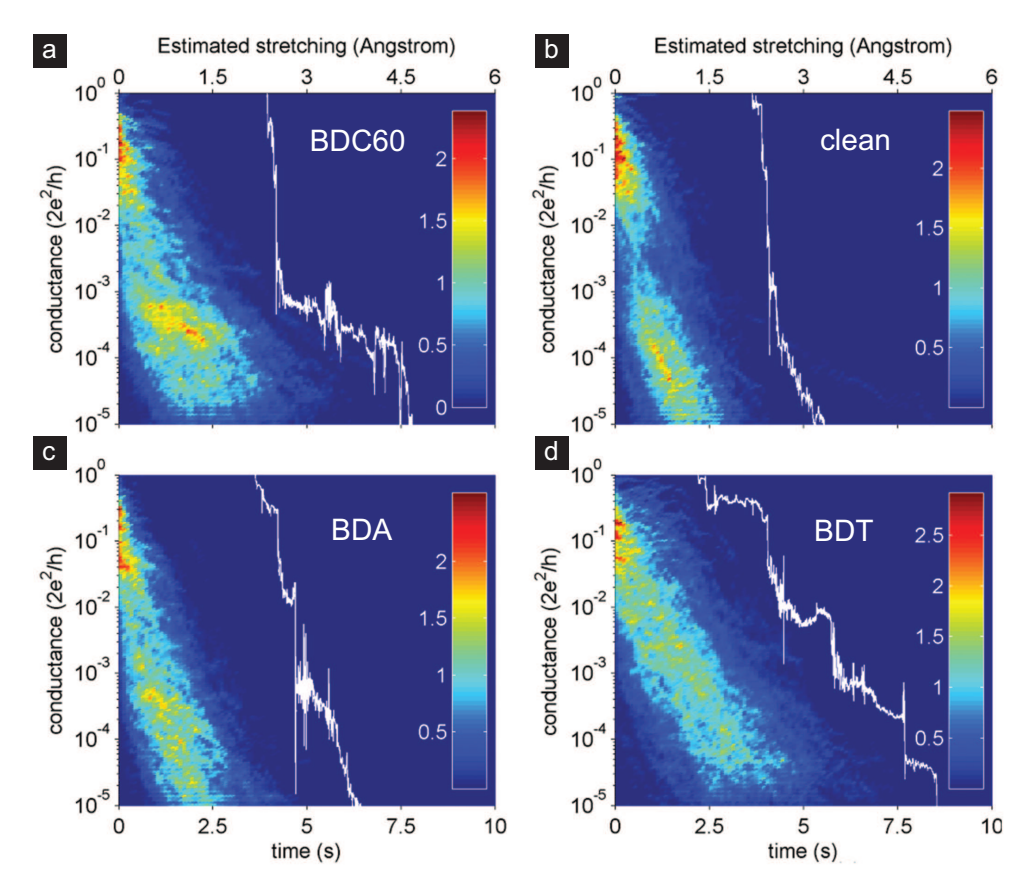


FIGURE 5.4: Trace histograms from 400 consecutive breaking traces. Histogram counts have been normalized to ms/trace and are color-encoded. Areas with highest counts represent the most typical breaking behavior of the individual junctions. In each histogram this is exemplified by one breaking trace (white). The stretching distance has been estimated from the displacement ratio of clean lithographic break junctions.

cently, histograms of plateau lengths have been used to characterize the stability of single-molecule junctions [16]. However, spontaneous conductance fluctuations during the slow breaking of lithographic MCBJs can render plateau detection in the sub- G_0 regime erroneous. We have applied a new statistical method that extracts the complete breaking dynamics below 1 G_0 (see Chapter 3). All data beyond the rupture of the last monatomic gold contact are evaluated statistically in both time, that is, stretching distance and conductance. In the resulting trace histograms, areas of high counts represent the most typical breaking behavior of the molecular junctions.

Figure 5.4a presents such a trace histogram for BDC60. Immediately after breaking it exhibits a narrow region of high counts around $0.1\ G_0$. It is a sign of short-lived high-conductance states that are observed in all graphs in Figure 5.4. They may not be a characteristic feature of the molecular junctions and will hence be ignored in the discussion.

5.5. Conclusions 89

After these initial states the trace histogram of BDC60 reflects a fast conductance decay and an extended region of high counts around $3 \cdot 10^{-4} G_0$ that is consistent with the histogram in Figure 5.3b. This region is due to individual breaking traces with plateaus at the same conductance, similar to the white curve superimposed on Figure 5.4a. In trace histograms, flat plateaus below 1 G_0 result in horizontal lines. Any variation in the molecular conductance causes a vertical blurring of these lines. Such a spread is indeed present in Figure 5.4a. Furthermore, the trace histogram indicates the presence of slightly sloped plateaus, which are also visible in the traces in Figure 5.3a. The horizontal spread of the accumulation region indicates that the fullerene-anchored junctions can be stable for more than 3 s. Figure 5.4b presents the trace histogram of a junction that has been exposed to clean toluene. In contrast to molecular conductance plateaus, the exponential decay typical of vacuum tunneling results in a steeply sloped region of accumulation from about 10^{-3} to 10^{-5} G_0 . No accumulation regions of well-defined conductance can be observed. The trace histogram of BDA (Figure 5.4c) exhibits only a small region of enhanced counts around $4 \cdot 10^{-4}$ G_0 . Its width is smaller than for BDC60, supposedly due to the limited stability of the amine-gold bond (see Chapter 4). Note that this conductance value is smaller than the one observed in recent experiments in solution[6]. Possibly, the absence of a surrounding solvent leads to different junction geometries, and hence different electronic properties (see also Chapter 4). BDT junctions do not exhibit any preferred breaking behavior but a slow conductance decay with uniformly distributed counts (Figure 5.4d). The lack of a clear signature is consistent with the histogram in Figure 5.3b and can be attributed to the variability of the thiol-gold bond [3].

5.5 CONCLUSIONS

In conclusion, we have demonstrated the suitability of fullerene anchoring for single-molecule electronic measurements. Compared to thiols the fullerene-anchoring leads to a considerably lower spread in low-bias conductance. In addition, junctions of fullerene-anchored benzenes exhibit an increased stretching length before breaking. These findings open up new opportunities for the formation of stable molecular junctions.

REFERENCES

- [1] J. C. Love, L. A. Estroff, J. K. Kriebel, R. G. Nuzzo, and G. M. Whitesides, *Self-Assembled Monolayers of Thiolates on Metals as a Form of Nanotechnology*, Chem. Rev. **105**, 1103 (2005).
- [2] N. J. Tao, Electron transport in molecular junctions, Nat. Nano. 1, 173 (2006).
- [3] J. Ulrich, D. Esrail, W. Pontius, L. Venkataraman, D. Millar, and L. H. Doerrer, *Variability of Conductance in Molecular Junctions*, J. Phys. Chem. B **110**, 2462 (2006).
- [4] C. Li, I. Pobelov, T. Wandlowski, A. Bagrets, A. Arnold, and F. Evers, *Charge Transport in Single Au/alkanedithiol/Au Junctions: Coordination Geometries and Conformational Degrees of Freedom*, J. Am. Chem. Soc. **130**, 318 (2008).

- [5] A. M. Moore, A. A. Dameron, B. A. Mantooth, R. K. Smith, D. J. Fuchs, J. W. Ciszek, F. Maya, Y. Yao, J. M. Tour, and P. S. Weiss, *Molecular Engineering and Measurements To Test Hypothesized Mechanisms in Single Molecule Conductance Switching*, J. Am. Chem. Soc. 128, 1959 (2006).
- [6] L. Venkataraman, J. E. Klare, I. W. Tam, C. Nuckolls, M. S. Hybertsen, and M. L. Steiger-wald, Single-Molecule Circuits with Well-Defined Molecular Conductance, Nano Lett. 6, 458 (2006).
- [7] L. Venkataraman, J. E. Klare, C. Nuckolls, M. S. Hybertsen, and M. L. Steigerwald, *Dependence of single-molecule junction conductance on molecular conformation*, Nature **442**, 904 (2006).
- [8] S. Yoshimoto, R. Narita, E. Tsutsumi, M. Matsumoto, K. Itaya, O. Ito, K. Fujiwara, Y. Murata, and K. Komatsu, *Adlayers of Fullerene Monomer and* [2 + 2]-Type Dimer on Au(111) in Aqueous Solution Studied by in Situ Scanning Tunneling Microscopy, Langmuir 18, 8518 (2002).
- [9] S. Uemura, P. Samory, M. Kunitake, C. Hirayamaa, and J. P. Rabe, *Crystalline C*₆₀ *monolayers at the solid–organic solution interface*, J. Mater. Chem. **12**, 3366 (2002).
- [10] C. Rogero, J. I. Pascual, J. Gómez-Herrero, and A. M. Baró, *Resolution of site-specific bonding properties of C*₆₀ adsorbed on Au(111), J. Chem. Phys. **116**, 832 (2002).
- [11] T. Böhler, A. Edtbauer, and E. Scheer, Conductance of individual C_{60} molecules measured with controllable gold electrodes, Phys. Rev. B **76**, 125432 (2007).
- [12] Y. Xue, S. Datta, and M. A. Ratner, *Charge transfer and 'band lineup' in molecular electronic devices: A chemical and numerical interpretation*, J. Chem. Phys. **115**, 4292 (2001).
- [13] M. Maggini, G. Scorrano, and M. Prato, *Addition of azomethine ylides to C*₆₀: *synthesis, characterization, and functionalization of fullerene pyrrolidines*, J. Am. Chem. Soc. **115**, 9798 (1993).
- [14] B. Xu and N. J. Tao, Measurement of Single-Molecule Resistance by Repeated Formation of Molecular Junctions, Science **301**, 1221 (2003).
- [15] M. T. González, S. Wu, R. Huber, S. J. van der Molen, C. Schönenberger, and M. Calame, *Electrical Conductance of Molecular Junctions by a Robust Statistical Analysis*, Nano Lett. **6**, 2238 (2006).
- [16] Y. S. Park, A. C. Whalley, M. Kamenetska, M. L. Steigerwald, M. S. Hybertsen, C. Nuckolls, and L. Venkataraman, Contact Chemistry and Single-Molecule Conductance: A Comparison of Phosphines, Methyl Sulfides, and Amines, J. Am. Chem. Soc. 129, 15768 (2007).

GATED MCBJS WITH SUSPENDED SOURCE-DRAIN ELECTRODES - A NANOELECTROMECHANICAL SYSTEM

This chapter explores the electromechanical characteristics of gated MCBJs with suspended source-drain electrodes. The actuation of the source-drain electrode pair by the gate voltage can be exploited to reversibly switch between a monatomic contact with a conductance around $2e^2/h$ and the tunneling regime. In tunneling, the source-drain conductance varies smoothly with gate voltage. The characteristics of the devices can be understood within a simple continuum model. It indicates that the elastic properties of the substrate facilitate the electromechanical tuning and that the details of the switching depend sensitively on the nanoscale geometry of the electrode tips.

Parts of this chapter have been published as C. A. Martin, R. H. M. Smit, H. S. J. van der Zant, and J. M. van Ruitenbeek, Nano Lett. 9, 2940 (2009).

6.1 Introduction

In the course of the down-scaling of integrated circuits, the active area in individual electronic and electromechanical devices may ultimately be reduced to a few atoms. The implementation of functionality at such a small size requires a detailed understanding of electronic and mechanical processes on the atomic scale. In metallic wires, a reduction of the cross-section to a few atoms leads to the onset of quantum mechanical effects and, for gold, a quantization of the conductance in units of $1 G_0 = 2e^2/h \approx 77 \mu S$ [1]. The implementation of active nanoscale devices such as switches requires the control of individual atoms in either metal junctions [2, 3], or semiconductor structures [4], or individually wired molecules [5-9]. In single-molecule devices, conductance switching has thus far been achieved through photon irradiation [5, 6], bias voltage tuning [7], mechanical tuning [8], and electrochemical gating [9]. Electrically controlled single-atom switches have only recently been realized [2]. By means of an electrochemical gate in liquid, two nanoscale silver electrodes were deposited in a bottom-up process. The gatedependent surface tension of the electrolyte could then be used to mechanically switch the junctions between an insulating off-state and an on-state with a high conductance of several G_0 [3]. Top-down fabricated and vacuum-compatible nanoelectromechanical switches have been based on carbon nanotube cantilevers [10] and TiN beams [11]. However, their on-conductance was intrinsically limited by a non-metallic electrical contact between the two electrodes. In this chapter, we demonstrate that gated mechanical break junctions (gated MCBJs) [12] can be used as prototypical nanoelectromechanical relays that can be operated in vacuum and that possess a high conductance in the on-state. A well-defined single-atom gold contact is formed in a gated MCBJ at cryogenic temperatures. The gate potential then controls the breaking and the formation of the Au-Au bond and switches the source-drain conductance between about 1 G_0 and the tunneling regime. In tunneling, the conductance of the device can be tuned over several orders of magnitude. A simple continuum model is developed to explain the electromechanical effect.

6.2 EXPERIMENTAL DETAILS

The fabrication of the gated MCBJs extends the batch process for two-terminal junctions that is described in Chapter 3. In short, phosphor bronze wafers are polished, cleaned thoroughly, and coated with an insulating polyimide layer of about 3 μ m thickness (PI2610, HD Microsystems). The devices on these wafers are then fabricated by repeated cycles of spin-coating of double-layer resist (MMA/MAA copolymer and PMMA 950k), patterning with high-resolution e-beam lithography, evaporation of metal layers, and lift-off in hot acetone. Figure 6.1a presents a scanning electron micrograph of a gated MCBJ after the complete process. The fabrication steps are illustrated in Figure 6.1b. In the first step we fabricate lithography markers (2 nm Ti and 130 nm Au) on the bare wafers (not shown). The gate (2 nm Cr and 50 nm Au) is aligned with respect to these markers. To enable the fabrication of a vacuum gap between the gate and the break junction electrodes a sacrificial polymeric layer is applied: The wafers are spin-coated with a diluted polyimide precursor solution (1 part PI2610 in 3 parts T9039, HD Microsystems, 70 s at 4000 rpm) and baked out in a vacuum oven (30 min at 250°C). This leads to a polyimide thickness

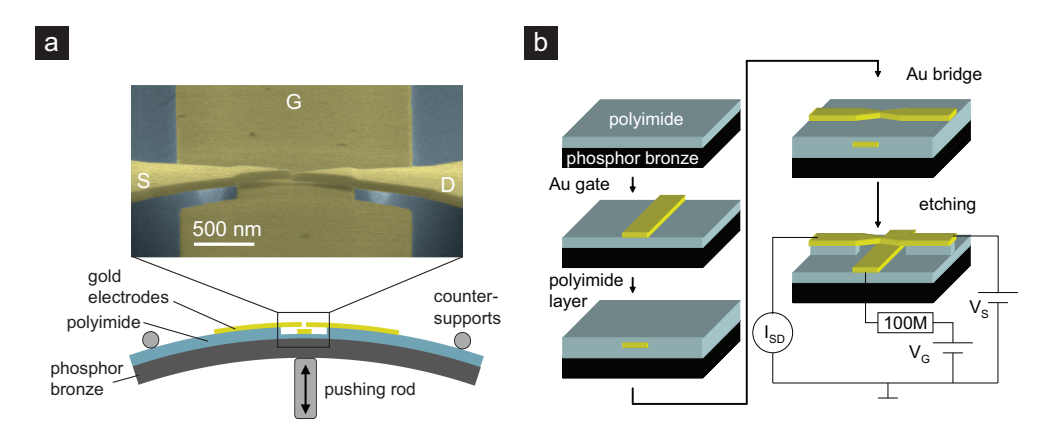


FIGURE 6.1: A gated mechanical break junction with suspended source-drain electrodes. (a) Electron micrograph of device A (see text, colorized for clarity). The source-drain electrodes (S,D) are suspended 45 nm above the gate (G) and have been stretched and broken by bending the flexible MCBJ substrate in a 3-point bending mechanism. The electrode tips are slightly misaligned, possibly due to the release of processing-induced stress in the metal film. (b) Schematic of the device fabrication and the electrical measurement circuit. The gate is protected from electrostatic discharges by a series resistor.

of about 50 nm, corresponding to the size of the intended vacuum gap between the gate and the suspended electrodes (a further reduction of the gap size is hindered by dewetting of the precursor solution at higher dilutions). On top of the polyimide layer, 3 bridges with approximately 80 nm-wide constrictions (2 nm of Cr and 80 nm of Au) are aligned with the buried gate electrode. In the region of the constrictions, the gate electrode narrows down to facilitate the subsequent underetching process. The device fabrication is completed by dry etching in a reactive ion plasma of CF_4 and O_2 (flow rate ratio 6:50 sccm, pressure 0.2 mbar, RF power 30 W). This removes the sacrificial layer between the gate and the source-drain electrodes as well as some of the supporting polyimide layer and leads to a suspended gold bridge with a length of about 1.7 μ m, as depicted in Figure 6.1a.

Before the measurements, the sample chamber was evacuated to 10^{-5} mbar and cooled in liquid helium to a base temperature of about 6 K, leading to a cryogenic vacuum at the position of the gated MCBJs.

The MCBJs could be broken and rejoined by controlling the bending of the flexible substrate both at 6 K and at room temperature. Throughout this process, the integrity of the gate electrode was maintained. Since the high surface mobility of gold can be expected to hamper the formation of stable contacts at room temperature, all experiments on single-atom switching were carried out at cryogenic temperatures.

6.3 GATE-INDUCED SWITCHING OF QUANTUM POINT CONTACTS

We have established the gate-induced tuning of the source-drain conductance in the tunneling regime for five out of five devices that we studied. In two gated MCBJs, the suspended electrodes were subjected to a generic training procedure (to be discussed later),

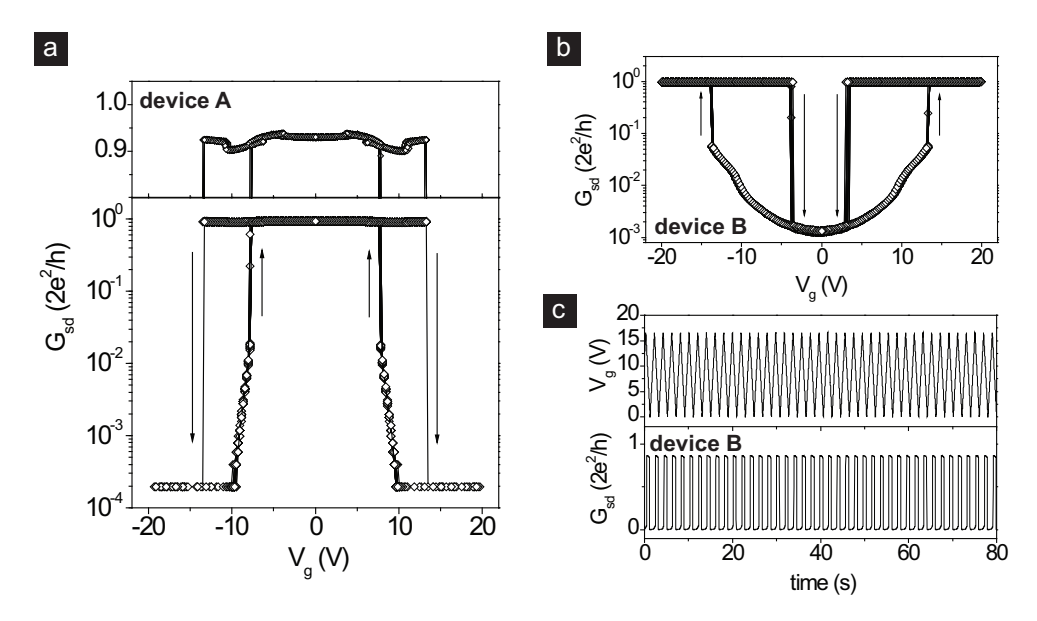


FIGURE 6.2: Gate-induced reversible switching of single-atom contacts in mechanical break junctions. (a) Switching characteristics of a gated mechanical break junction during 20 consecutive gate voltage cycles at a bias voltage of 50 mV on a linear and semilogarithmic scale. The gate voltage sweeps took about 200 s each. (b) Switching characteristics of another device, in which a single atom contact is established at high gate voltages. Measurement parameters are identical to the ones for device A, but the switching direction is inverted. (c) Repeated switching of device B between a single-atom contact with a conductance around 0.9 G_0 and the tunneling regime. The upper panel presents the applied triangular gate voltage signal.

at the end of which both exhibited highly reproducible gate-controlled switching. Parts a and b of Figure 6.2 present the resulting switching characteristics during 20 consecutive gate voltage cycles. The source-drain conductance in both devices switches reproducibly and hysteretically between the tunneling regime and a single-atom contact with a conductance of about 1 G_0 . In device A, the single-atom contact is broken at large absolute gate voltages. Device B, in contrast, switches from the tunneling regime to a conductance of 1 G_0 as the gate voltage is increased. The hysteresis in conductance is inverted with respect to device A and the switching occurs at different gate voltages. Figure 6.2c presents single-atom switching in device B at a rate of about 0.5 Hz and illustrates the repeatability of the effect. The origin of the different switching directions will be discussed later. In the following we analyze the electromechanical characteristics of device A in detail and develop a general model of the gate effect.

At zero gate voltage, the source-drain conductance in device A is about 1 G_0 , corresponding to a monatomic contact between the two suspended electrodes. As the gate voltage is increased, the junction conductance remains around this value but exhibits small, reproducible variations (see upper panel in Figure 6.2a). These may originate from reversible atomic-scale changes of the electrodes that affect the electron transmission of the point contact [1]. Once the gate voltage exceeds 13.5 V, the junction conductance drops sponta-

neously and sharply from 1 G_0 to a value below the measurement resolution. For all larger gate voltages up to 20 V, the conductance remains below this value. Clearly, the single-atom contact has been broken by means of the gate electrode. Only as the gate voltage is decreased below 10 V does the conductance re-enter the measurement window. Subsequently, the conductance increases nearly exponentially with decreasing gate voltage until it exhibits an abrupt jump to about 1 G_0 at about 8 V; the single-atom contact has been formed again. When the gate voltage is decreased to zero, the conductance remains around 1 G_0 but again exhibits small variations. As the gate voltage polarity is inverted, the switching behavior is reproduced with remarkable symmetry. Below a gate voltage of -13.5 V, the contact breaks. Only when the voltage is increased above -8 V is the single-atom contact formed again. Importantly, there is a highly reproducible hysteresis between the breaking and the fusing of the contact, with the spontaneous formation occurring at lower gate voltage.

In two-terminal MCBJs made from gold, similar, but bending-controlled, hysteresis loops have been observed [13]. Here, the cleavage of the last monatomic contact with a rapid transition to the tunneling regime is commonly referred to as the jump out of contact (JOC). Its characteristics can be explained by the elastic properties of the topmost atomic layers of the electrodes, which allow for an elongation of the 1 G_0 -contact preceding the JOC [13]. After the rupture of the last Au-Au bond, the electrode tips relax and their distance increases spontaneously by several angstroms, leading to a large conductance drop. Upon fusing, a large part of this elastic relaxation needs to be compensated for before a metallic contact can be re-established. The spontaneous formation of a single-atom contact is then accompanied by an abrupt jump from tunneling to a conductance of about 1 G_0 , the jump to contact (JC).

The reproducibility and the fine structure of the JOC and the JC in Figure 6.2a suggest similar processes in the gated MCBJ; at the JOC, the conductance drops below the detection limit, whereas it increases smoothly before the JC. The difference can be explained by a mechanical relaxation of the electrodes after the rupture of the monatomic contact.

The symmetry of the switching of the quantum point contacts with gate voltage indicates an electromechanical actuation of the suspended electrodes, similar to nanofabricated relays [10, 11]. The electric field in the vacuum gap leads to an attractive force toward the gate, which is independent of the gate voltage polarity. In device A, the resulting bending then causes the cleaving of the monatomic contact. In the following sections, we discuss the switching mechanism in more detail and develop a continuum model of the electromechanical actuation of the electrodes.

We found that the presence of reproducible jumps in and out of contact during the bending of the substrate is an important prerequisite for successful single-atom switching. In two-terminal MCBJs, monatomic junctions with well-defined geometries and highly reproducible breaking characteristics have recently been formed via repeated mechanical cycling [13]. This training procedure was also applied in the case of the gated MCBJs. Before studying the single-atom switching, we bent and cycled the devices several times between the broken state and a conductance of about 1 G_0 using a wide-range logarithmic current-voltage converter (see Chapter 3). Figure 6.3a presents three consecutive breaking and fusing characteristics for device A at the end of several such cycles. After about 3.5 s of

bending, the conductance drops from 1 to $10^{-4}\ G_0$ at the JOC (solid lines). As the electrode distance is increased further, the conductance decreases exponentially. Upon fusing, the JC occurs around $10^{-2}\ G_0$ (dotted lines). Figure 6.3a illustrates the reproducibility and the hysteresis of the JOC and the JC during the bending of the gated MCBJ, which are in good agreement with two-terminal MCBJs [13]. Furthermore, the degree of reproducibility is comparable to that in the gate-controlled switching in Figure 6.2a and suggests similar microscopic switching mechanisms.

After having observed a reproducible JOC and JC during the bending of the substrate, we broke the junction to a conductance below the noise floor of the measurement. We then closed the junction stepwise while repeatedly measuring the gate-dependence of the source-drain current with a linear current-voltage converter (see the next paragraph for a detailed discussion). Throughout this process, the MCBJ architecture allows for a precise adjustment of the electrode gap via the bending of the macroscopic substrate. Figure 6.3b presents the exponential increase of the conductance during this process. The small deviations from a smooth exponential are due to irregularities in the mechanical drive of the device. The exponential dependence allows us to determine the displacement ratio of the junction, which relates the electrode stretching to the deflection of the substrate center. The theoretical displacement ratio of a uniformly bent gated MCBJ device can be deduced from its geometry as $r = 12LH_S/L_S^2$, where 2L is the suspended length of the source-drain electrode pair (see Chapter 3). For our devices, we obtain a theoretical displacement ratio of $r = 1.2 \cdot 10^{-5}$. The experimental value can be estimated from the conductance slope in tunneling assuming a simple exponential decay with increasing electrode separation (see Chapter 2):

$$G(d_0 + \Delta d) = G(d_0) \exp(-\frac{\sqrt{8m_e \Phi_m}}{\hbar} \Delta d)$$
(6.1)

A fit of the tunneling characteristics in Figure 6.3b yields a displacement ratio of $2.6 \cdot 10^{-5}$, which is by a factor of 2.2 larger than the theoretical result. The effective enhancement of the displacement ratio can be attributed to the elasticity of the polyimide insulator [14]. The Young's modulus of polyimide is as small as a few GPa, as compared to about 82 GPa for bulk gold.

At several points during the fusing, we studied the dependence of the tunneling current on gate voltage. The gated junctions were usually found to be stable up to gate voltages of 20 V, i.e., beyond the values reported in [12]. This difference can be attributed to the use of a local gate electrode instead of a common back gate. Figure 6.3c presents the results of a typical three-terminal measurement in the gate voltage interval from -20 to 20 V. The dependence of the source-drain differential conductance on gate voltage is symmetric in polarity. As the absolute value of the gate voltage is increased, the tunneling conductance is reduced to a value below the measurement resolution (black regions in Figure 6.3c). The conductance as a function of gate voltage for four different configurations in the tunneling regime is presented in Figure 6.3d. Notably, the relative conductance decrease as a function of gate voltage is almost independent of the starting value of the conductance, i.e., the initial separation of the electrodes. Only for the highest conductance can a slightly faster decay be observed. It may be due to image force-induced barrier lowering at such small

6.4. Modeling 97

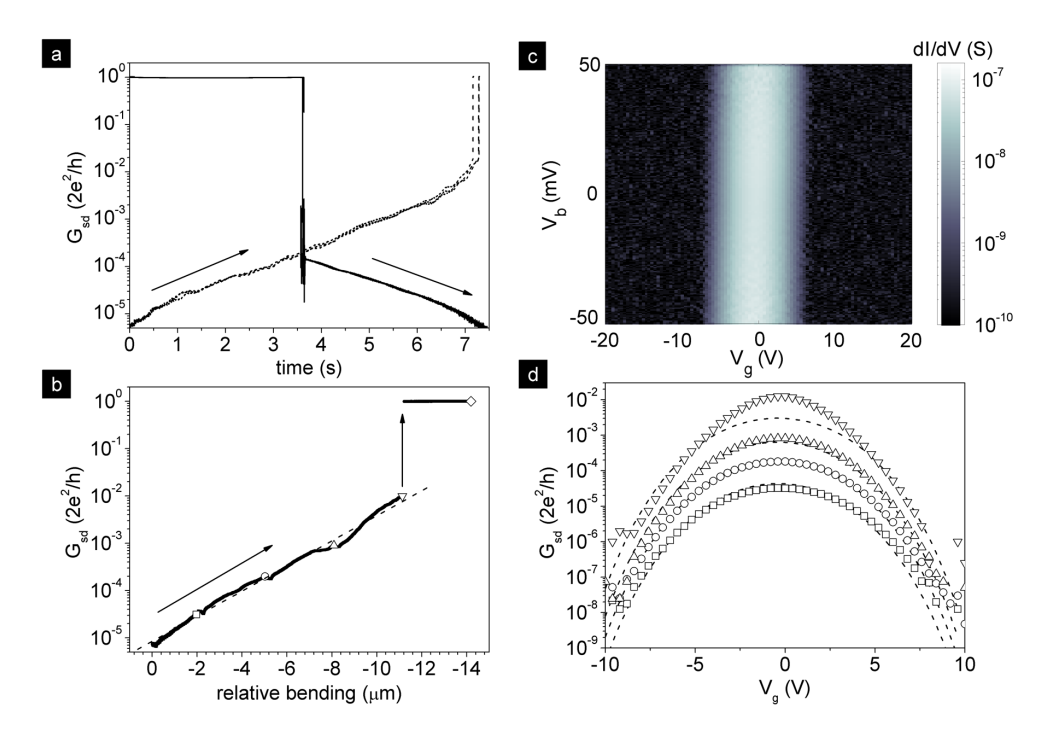


FIGURE 6.3: Details of the bending and gate-controlled conductance tuning of device A. (a) Reproducible mechanically controlled breaking of a single-atom contact. The graph presents three consecutive breaking and fusing characteristics at a bias of 50 mV and a bending speed of 2 μ m/s. (b) Conductance evolution during the fusing at a bias of 50 mV. The dashed line presents a fit to an exponential tunneling law (see text). The open symbols mark locations of three-terminal measurements. (c) Plot of the differential conductance as a function of gate voltage and source-drain bias in the tunneling regime, corresponding to the open upward-pointing triangle in part b. (d) Mean conductance in the bias interval ± 20 mV as obtained from a linear fit of three-terminal measurements. The symbols correspond to those in part b. The dotted lines present a fit to the electromechanical continuum model described in the text.

electrode distances [15].

6.4 Modeling

The symmetric gate potential dependences in both the tunneling and the single-atom regime are consistent with an electrostatic attraction of the suspended electrodes by the gate. Since the displacements of the electrodes can be expected to be small, we apply linear continuum mechanics to calculate the electromechanical response of the device. In a first approximation, the gate and each suspended electrode can be modeled as a parallel-plate capacitor. The attractive force per unit length of the clamped electrode can then be obtained by differentiating the electrostatic energy in the gap with respect to the

distance to the gate:

$$F'_z(x) = -\frac{d}{dz} \left(-\frac{1}{2} C'(x) V^2 \right) \approx \frac{\epsilon_0 V^2}{2} \frac{W(x)}{(D_0 - z(x))^2}.$$
 (6.2)

Here, C'(x) is the capacitance per unit length, ϵ_0 is the permittivity of the vacuum, and W(x), D_0 , and z(x) are the geometrical parameters indicated in Figure 6.4a. For small ratios W/D_0 such as the ones in our devices, however, the parallel-plate approximation breaks down and fringing electric fields have to be included. Following an approach of Chowdhury *et al.* [16], we apply a semi-empirical formula [17] to model the capacitance in our device

$$C'(x) = \epsilon_0 \left[\frac{W(x)}{D_0 - z(x)} + 0.77 + 1.06 \left(\frac{W(x)}{D_0 - z(x)} \right)^{0.25} + 1.06 \left(\frac{H}{D_0 - z(x)} \right)^{0.5} \right]. \tag{6.3}$$

Once an expression of the electrostatic attractive force has been obtained, the deflection of the electrodes can be calculated from the Euler-Bernoulli equation,

$$\frac{d^2}{dx^2} \left(EI_{yy} \frac{d^2z}{dx^2} \right) = F_z'(x) \tag{6.4}$$

where E = 82 GPa is the Young's modulus of the gold electrodes and $I_{yy}(x) = H^3 W(x)/12$ is the position-dependent moment of inertia.

The integration is carried out using the boundary conditions for a clamped cantilever. Since the bending of the electrode leads to an increase in electrostatic force, the calculation has to be carried out self-consistently. The bending that is obtained from one numerical integration run serves as an input for calculating the electrostatic force in the next one. The loop continues until the change in the computed bending becomes negligibly small, in our case

$$\left\langle \left(\frac{z(x)_{k+1} - z(x)_k}{z(x)_{k+1}} \right)^2 \right\rangle \le 10^{-10}$$
 (6.5)

for two consecutive iterations k and k + 1.

The change in tunneling distance Δd between the source-drain electrodes follows from the bending profile of a single clamped electrode as

$$\Delta d(h) \approx 2 \left\{ L \left[1 - \cos \left(\arcsin \frac{z(L)}{L} \right) \right] + \left(h - \frac{H}{2} \right) \sin \left(\arctan \frac{dz}{dx} \Big|_{z=L} \right) \right\}$$
 (6.6)

where H and L are the thickness and suspended length of the electrode and $0 \le h \le H$ denotes the location of the point contact from the top of the electrode (see detail in Figure 6.4a). The first term of Equation 6.6 approximates the increase in electrode distance due to the deflection of the tip. The second term models the contribution of the tip rotation, which depends on the location of the tunneling junction. While the rotation leads to a decrease in distance in the upper half of the electrodes ($0 \le h < H/2$), points closer to the bottom of the electrodes ($H/2 < h \le H$) are separated further. Inserting Equation 6.6

6.4. Modeling 99

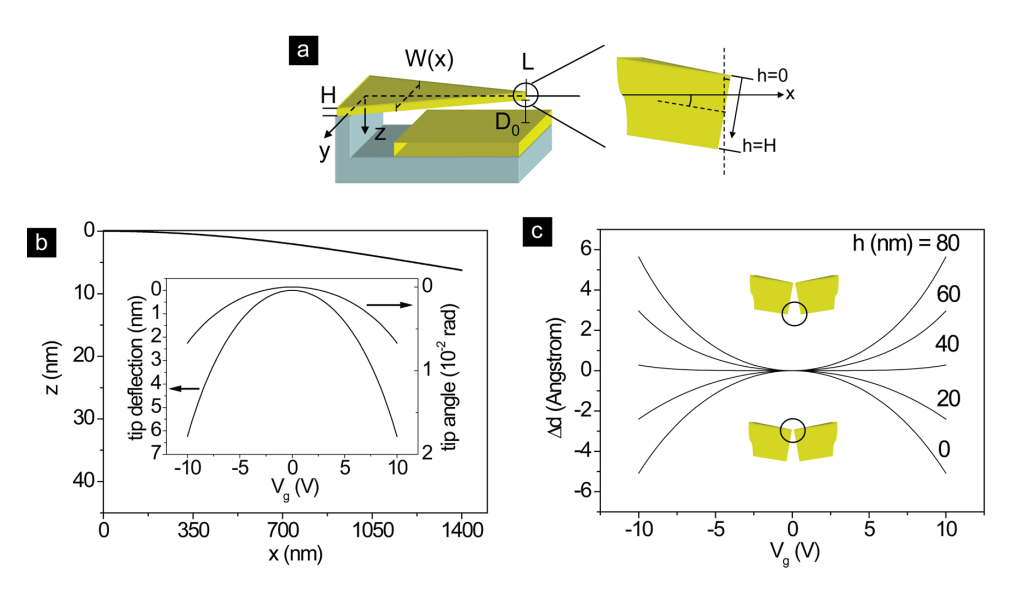


FIGURE 6.4: Model of the electromechanical actuation. (a) Schematic of one freely suspended electrode with the parameters used in the calculations and detail of the electrode tip. (b) Calculated bending profile for one electrode at a gate voltage of 10 V and a suspended length of 1400 nm. The inset presents the deflection and the angle of the electrode tip for varying gate voltage. (c) Change in tip distance at several positions along the electrode face.

in Equation 6.1 finally yields the gate-induced tuning of the tunneling conductance.

The strong dependence of the change in electrode distance on the position of the point contact on the tips is supported by the different switching characteristics of devices A and B (see parts a and b of Figure 6.2). Within the framework of our model, we can deduce that the single-atom contact in device B is located in the upper half of the electrodes. This configuration results in a decreasing tunneling distance with increasing gate voltage and, finally, the fusing of the contact. The monatomic contact in device A, in contrast, breaks at large gate voltages, indicative of a location in the lower half of the electrode faces. For the fit of our model to the gate-dependent tunneling conductances of device A we assumed the location of the point contact to be at the bottom of the suspended electrodes, i.e., h = 80 nm, and used the geometrical parameters H, D_0 , and W(x) as obtained from scanning electron microscopy. With the suspended electrode length as the only remaining fit parameter, we achieve good quantitative agreement of our calculations with the three lower curves in Figure 6.3d for $L = 1.4 \mu m$. The deviation for the highest conductance may be due to the omission of image forces [15] in our simple tunneling model. Interestingly, the suspended length obtained from the fit is by a factor of 1.6 larger than the geometrical underetching of the junction (see Figure 6.1a). Similar to the displacement ratio of MCBI devices [14], the electromechanical properties of the gated MCBJs may be influenced by the elasticity of the polyimide layer; here, it allows for a bending of the electrodes beyond the geometrical clamping point.

A plot of the calculated bending characteristics for $L=1.4~\mu m$ is presented in Figure 6.4b. At a gate voltage of 10 V, the tip deflection is on the order of 6 nm. This is much smaller than the electrode length, confirming that linear continuum mechanics can be applied. The calculated changes in tip distance for a point contact at different positions along the electrode tip are presented in Figure 6.4c. With increasing distance of the point contact from the electrode top, a transition from an effective fusing to a gate-induced stretching can be observed. The nearly flat characteristics for h=40 nm indicate that the distance tuning due to tip deflection is much smaller than the one due to tip rotation. For the assumed location of the junction at h=80 nm, the gap increase at a gate voltage of 10 V is as large as 6 Å, one order of magnitude smaller than the corresponding tip deflection.

It is also instructive to compare the calculations to the switching data in Figure 6.2a. From experiments in two-terminal MCBJs it is known that the breaking and the formation of a monatomic bond show a hysteresis of up to 2 Å, which can be attributed to the elastic properties of the atomic-scale electrodes [13]. Within our model, however, we obtain a theoretical mechanical hysteresis of 12 Å for the gate-induced single-atom switching presented in Figure 6.2a. This value is larger than expected, since it exceeds the atomic spacing in bulk gold by far. Most likely, the hysteresis is strongly influenced by the atomic structure near the contact. We have observed variations in the switching of single-atom contacts in devices A and B that support this interpretation. When the contact is mechanically fused to a conductance of several G_0 , the switching can be modified through a rearrangement of the atoms at the electrode tips. The adhesive forces within the monatomic contact [1, 13], which can be on the order of 1.5 nN, may hence lead to more complicated elastic deformations in the sensitive atomic environment that increase the effective hysteresis.

6.5 CONCLUSIONS

In this chapter, we have demonstrated that gated MCBJs can be used as tunable singleatom switches. The electrostatic attraction of the source-drain electrodes by the gate leads to a deflection and rotation of the electrode tips and a change in electrode separation, which can be exploited to reversibly break and form a single-atom contact. We have studied repeated switching at a rate of 0.5 Hz for more than 200 cycles without observing any sign of deterioration. The switching characteristics are clearly influenced by the microscopic environment and the location of the single atom contact on the electrode tip, as expected for a relay in this limit. A further miniaturization of the devices may be possible, provided the gate modulation of the electrode distance exceeds the mechanical hysteresis of the single-atom switch. Based on the value of 12 Å that is obtained from the modeling of device A, a possible length reduction by about 30% can be derived for a gate voltage range of 20 V. Gate voltages in excess of this value would allow for larger electrostatic forces and hence a further miniaturization. The integration of several individually gated devices on a single substrate may enable the independent electronic control of the conductance of several point contacts. This has only recently been achieved for two MCBJs on a flexible membrane [18]. Furthermore, the use of platinum electrodes could allow for the fabrication of single-atom relays that are stable at room temperature [19]. In contrast REFERENCES 101

to silicon-based gated MCBJs [12], the phosphor bronze devices possess sufficient flexibility to vary the electrode spacing over several nanometers. This also makes them suitable for three-terminal measurements on single molecules [20]. However, the observed electromechanical actuation imposes important restrictions on the device geometry; to prevent a convolution of electrical and mechanical conductance tuning, the electrode rigidity needs to be maximized while keeping a small enough cross section to form gate-tunable single-molecule junctions. A solution to this design challenge is presented in Chapter 8 of this Thesis.

REFERENCES

- [1] N. Agraït, A. L. Yeyati, and J. M. van Ruitenbeek, *Quantum properties of atomic-sized conductors*, Phys. Rept. **377**, 81 (2003).
- [2] F.-Q. Xie, L. Nittler, C. Obermair, and T. Schimmel, *Gate-Controlled Atomic Quantum Switch*, Phys. Rev. Lett. **93**, 128303 (2004).
- [3] F.-Q. Xie, R. Maul, A. Augenstein, C. Obermair, E. B. Starikov, G. Schoen, T. Schimmel, and W. Wenzel, *Independently Switchable Atomic Quantum Transistors by Reversible Contact Reconstruction*, Nano Lett. 8, 4493 (2008).
- [4] M. Klein, G. P. Lansbergen, J. A. Mol, S. Rogge, R. D. Levine, and F. Remacle, *Reconfigurable Logic Devices on a Single Dopant Atom-Operation up to a Full Adder by Using Electrical Spectroscopy*, Chem. Phys. Chem. **10**, 162 (2009).
- [5] D. Dulić, S. J. van der Molen, T. Kudernac, H. T. Jonkman, J. J. D. de Jong, T. N. Bowden, J. van Esch, B. L. Feringa, and B. J. van Wees, *One-Way Optoelectronic Switching of Photochromic Molecules on Gold*, Phys. Rev. Lett. 91, 207402 (2003).
- [6] A. C. Whalley, M. L. Steigerwald, X. Guo, and C. Nuckolls, *Reversible switching in molecular electronic devices*, J. Am. Chem. Soc. **129**, 12590 (2007).
- [7] E. Lörtscher, J. W. Ciszek, J. Tour, and H. Riel, *Reversible and Controllable Switching of a Single-Molecule Junction*, Small **2**, 973 (2006).
- [8] S. Y. Quek, M. Kamenetska, M. L. Steigerwald, H. J. Choi, S. G. Louie, M. S. Hybert-sen, J. B. Neaton, and L. Venkataraman, *Mechanically controlled binary conductance switching of a single-molecule junction*, Nat. Nano. 4, 230 (2009).
- [9] T. Morita and S. Lindsay, *Reduction-induced switching of single-molecule conductance of fullerene derivatives*, J. Phys. Chem. B **112**, 10563 (2008).
- [10] S. W. Lee, D. S. Lee, R. E. Morjan, S. H. Jhang, M. Sveningsson, O. A. Nerushev, Y. W. Park, and E. E. B. Campbell, A three-terminal carbon nanorelay, Nano Lett. 4, 2027 (2004).
- [11] W. W. Jang, J. O. Lee, J.-B. Yoon, M.-S. Kim, J.-M. Lee, S.-M. Kim, K.-H. Cho, D.-W. Kim, D. Park, and W.-S. Lee, *Fabrication and characterization of a nanoelectromechanical switch with 15-nm-thick suspension air gap*, Appl. Phys. Lett. **92**, 103110 (2008).

- [12] A. R. Champagne, A. N. Pasupathy, and D. C. Ralph, *Mechanically Adjustable and Electrically Gated Single-Molecule Transistors*, Nano Lett. **5**, 305 (2005).
- [13] M. L. Trouwborst, E. H. Huisman, F. L. Bakker, S. J. van der Molen, and B. J. van Wees, Single Atom Adhesion in Optimized Gold Nanojunctions, Phys. Rev. Lett. 100, 175502 (2008).
- [14] S. A. G. Vrouwe, E. van der Giessen, S. J. van der Molen, D. Dulic, M. L. Trouwborst, and B. J. van Wees, *Mechanics of lithographically defined break junctions*, Phys. Rev. B **71**, 035313 (2005).
- [15] J. G. Simmons, Generalized Formula for the Electric Tunnel Effect between Similar Electrodes Separated by a Thin Insulating Film, J. Appl. Phys. **34**, 1793 (1963).
- [16] S. Chowdhury, M. Ahmadi, and W. C. Miller, *A closed-form model for the pull-in voltage of electrostatically actuated cantilever beams*, J. Micromech. Microeng. **15**, 756 (2005).
- [17] N. P. van der Meijs and J. T. Fokkema, *VLSI circuit reconstruction from mask topology*, VLSI Integration **2**, 85 (1984).
- [18] R. Waitz, O. Schecker, and E. Scheer, *Nanofabricated adjustable multicontact devices on membranes*, Rev. Sci. Instrum. **79**, 093901 (2008).
- [19] F. Prins, T. Hayashi, B. J. A. de Vos van Steenwijk, B. Gao, E. A. Osorio, K. Muraki, and H. S. J. van der Zant, *Room-temperature stability of Pt nanogaps formed by self-breaking*, Appl. Phys. Lett. **94**, 123108 (2009).
- [20] E. A. Osorio, T. Bjørnholm, J.-M. Lehn, M. Ruben, and H. S. J. van der Zant, Single-molecule transport in three-terminal devices, J. Phys.: Condens. Matter 20, 374121 (2008).

7

CHARGE TRANSPORT IN JUNCTIONS OF C_{60}

This chapter explores the electrical characteristics of C_{60} in two- and three-terminal mechanically controllable break junctions. In contrast to earlier studies on electromigration-based devices we do not find clear signatures of Coulomb blockade at low temperatures. However, the frequent observation of a zero-bias peak in the differential conductance is in agreement with previous reports of Kondo physics in single-molecule junctions of C_{60} . It indicates an intermediate electronic coupling to the gold electrodes and a clean metal-molecule interface.

We investigate the tuning of a zero-bias peak in the differential conductance of a gated MCBJ with suspended source-drain electrodes. The peak dependence on both the applied gate voltage and the electrode distance is analyzed with respect to the theory of the Kondo effect. The obtained Kondo temperatures and electronic couplings are in good agreement with previous measurements on C_{60} and consistent with a mechanical tuning of the junction by the gate.

7.1 Introduction

Since the first electrical characterization of a fullerene molecule in a scanning tunneling microscope [1], C_{60} has been one of the model systems in molecular electronics. Its low-temperature characteristics have been studied in a variety of experimental systems, such as mechanically controllable break junctions (MCBJs) [2–4], scanning-tunneling microscopes [5], nanoscale electrodes deposited by shadow evaporation [6], and in gaps formed by the electromigration of thin metal wires [7–9]. Despite the use of gold electrodes in all these experiments, the measured electronic properties of C_{60} have shown considerable spread. The reported transport characteristics have ranged from resonant tunneling with high conductances on the order of 0.1 C_{60} [3, 5, 6] to Coulomb blockade with current suppression at low bias voltages [2, 7, 8]. Moreover, some measurements have shown signatures of the Kondo effect [3, 4, 8, 9], which indicate an intermediate electronic coupling combined with the transfer of a full electron charge to the molecule.

The discrepancies in the electronic properties of C_{60} have largely been attributed to imperfections of the metal-molecule interface. Unlike the widely employed thiols, which form a covalent chemical bond with gold, C_{60} binds to metal surfaces through a combination of van-der-Waals interactions with partial electron transfer [10, 11]. On the clean Au(111) surface the excess charge on the fullerene amounts to an equivalent of 0.1 electrons, which leads to a stable bond with a dissociation energy of about 2.4 eV [12]. The associated electronic coupling in a Au- C_{60} -Au junction is strong and results in a theoretical conductance on the order of 1 G_0 [13].

So far, single-molecule conductances close to this value have only been observed in between electrodes that were formed in ultra-high vacuum [3, 14] or cryogenic vacuum [4]. Accordingly, measurements of lower conductances have been attributed to the solution-based deposition of C_{60} and an injection barrier of residual solvent molecules or other contaminants [3, 6]. Such a barrier would be critical for the fullerene-based anchoring group that was presented in Chapter 5; to attain a large hybridization of the C_{60} with the electrodes and to shift the injection barriers from the metal-molecule interface into the molecule a good electronic coupling is required.

To explore the nature of the Au-fullerene bond in our experiments, we have carried out reference measurements on pure C_{60} . We have studied its electronic properties in both two-terminal and gated MCBJs with suspended source-drain electrodes (see Chapter 6). In the three-terminal devices, C_{60} may also serve as a test system for the simultateous electrical and mechanical tuning of single-molecule transport [2].

To ensure a well-defined metal-molecule interface, we based our deposition on the adsorption of C_{60} from saturated solutions on the as-fabricated gold electrodes (see Chapter 5). A similar scheme has previously been applied to form stable adlayers of fullerenes in various solvents [15–17]. Both our two- and three-terminal MCBJs then allow us to create a nanoscale gap by breaking the source-drain electrode pair in high vacuum, which guarantees the exposure of clean gold surfaces for the formation of single-molecule junctions.

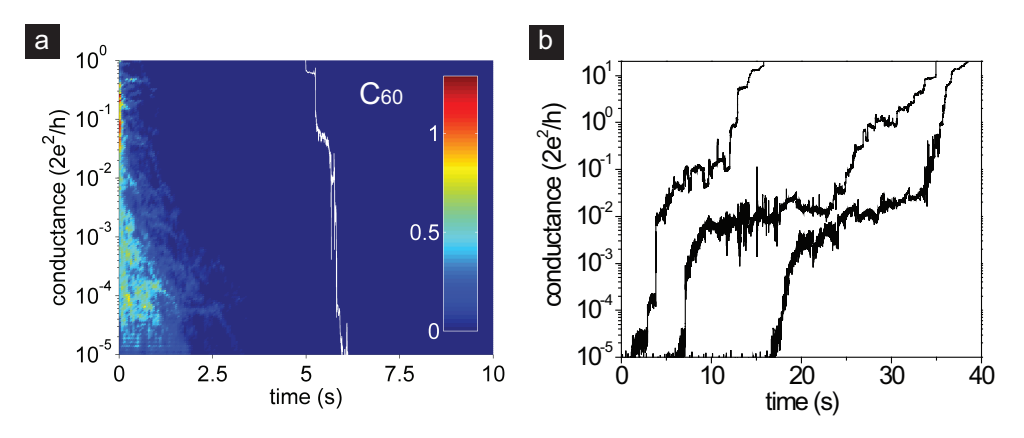


FIGURE 7.1: Room-temperature breaking and fusing characteristics of a MCBJ that was exposed to a solution of C_{60} in 1,2-dichlorobenzene. (a) Trace histogram from 400 consecutive breaking traces. Histogram counts have been normalized to ms/trace and are color-encoded. The superimposed white curve exemplifies the breaking behavior of the MCBJ. (b) Examples of fusing traces with particularly long plateaus that may be attributed to molecular junctions.

7.2 EXPERIMENTAL DETAILS

In all experiments, the C_{60} (Aldrich, sublimation-refined grade) was applied to the asfabricated MBCJs from saturated solutions in either 1,2-dichlorobenzene or toluene. The deposition followed the procedure described in Chapter 5. Before the electrical measurements we evacuated the measurement setup to a pressure below 10^{-5} mbar.

To determine the low-bias conductance of C_{60} we measured conductance histograms (see Chapter 3) at a dc bias of 50 mV. In order to break and re-establish the nanoscale contact the flexible MCBJ substrates were bent at an actuator speed of 2 μ m/s between the open and the fused state, given by conductances below 10^{-5} and above 20 G_0 , respectively.

After the measurements at room temperature, the devices were cooled to about 6 K while maintaining the previously characterized junction in the open state at a conductance below 1 G_0 by means of a feedback loop. The feedback is crucial, since an unintentional fusing of the electrodes can remove molecules from the junction area (see Chapter 4). At base temperature, we carried out IV measurements while varying the electrode distance.

7.3 CONDUCTANCE TRACE MEASUREMENTS

At room temperature, the rupture of junctions exposed to C_{60} typically progresses rapidly with occasional steps at varying conductances(see Figure 7.1a). Earlier, ultra-high vacuum-based experiments on evaporated C_{60} in MCBJs with gold electrodes have indicated single-molecule conductances around 0.2 G_0 [14] at room temperature. Since this value is in the range of the short-lived high-conductance steps that can even be observed in clean lithographic MCBJs (see Chapter 5), we cannot attribute the small signature around 0.1 G_0 in the breaking trace histogram in Figure 7.1a to C_{60} . However, if such highly conducting single-molecule junctions are formed, their lifetime must be limited. Possibly,

the combination of an elastic relaxation of the gold electrodes after the rupture of the last metal contact with a low surface concentration of C_{60} reduces the formation probability of stable single-molecule junctions. Below 0.1 G_0 , junctions exposed to pure C_{60} exhibit no clear signature. This observation is in contrast to the measurements of the fullereneanchored molecule presented in Chapter 5, which show pronounced regions of accumulation in trace histograms.

Despite the absence of a clear signature in the breaking traces, evidence for the formation of C_{60} junctions could be obtained during the fusing of some devices. It is important to note that the fusing characteristics of clean junctions may also show deviations from a straight exponential increase (see Chapter 3). However, some measurements on C_{60} yielded pronounced plateaus in the range from 0.01 to 0.1 G_0 (see Figure 7.1b) that are typically not present in MCBJs exposed to the clean solvent. These might be attributed to conduction through individual fullerene molecules that cover the tip of the electrodes after breaking. The observed conductance range is slightly lower than that in MCBJ-based experiments in ultra-high vacuum [3, 14]. In our experiments, a small remaining injection barrier may be formed by adsorbates from the high-vacuum environment.

7.4 IV MEASUREMENTS AT LOW TEMPERATURES

In contrast to earlier, electromigration-based experiments on C_{60} [2, 7–9], systematic IV-measurements on a total of three MCBJ devices did not yield any junctions in Coulomb blockade. Since the dI/dV characteristics at low temperatures provided convincing evidence of the formation of single-molecule junctions (see next paragraph), the absence of Coulomb blockade must be attributed to our molecule deposition scheme. The controlled adsorption of C_{60} on the as-fabricated MCBJs and a purely mechanical breaking of the source-drain electrode pair in high vacuum may lead to single-molecule junctions with larger electronic couplings than in gaps formed by electromigration.

During the stepwise breaking and fusing of the MCBJs at liquid helium temperatures, we frequently observed an enhancement of the differential conductance at zero bias (see parts a and b of Figure 7.2), bistabilities in the junction current above bias voltages of 20 mV (see Figure 7.2c), and steps and peaks in the dI/dV characteristics at varying bias voltages. Since the zero-bias resonances and the current instabilities occurred systematically, our discussion will focus on these two features.

Zero-bias peaks in the differential conductance have been observed in a number of low-temperature measurements on C_{60} [3, 4, 8, 9] and other nanoscale systems, such as semi-conductor quantum dots [18, 19] and metal point contacts [20]. Within the framework of the Kondo effect, they may be attributed to a single localized spin that couples antiferromagnetically to the electronic states on the electrodes (see Chapter 2). The coupling leads to the formation of a resonance at the Fermi energy in the density of states, which is reflected in the differential conductance. In experiments on C_{60} , signatures of the Kondo effect have been attributed to a charging of the molecule with a single electron [4].

To support the interpretation of the zero-bias resonances as signatures of the Kondo effect, an analysis of their scaling with temperature would be required (see Chapter 2). Since the MCBJ setup does not allow for active temperature control, we could not obtain this addi-

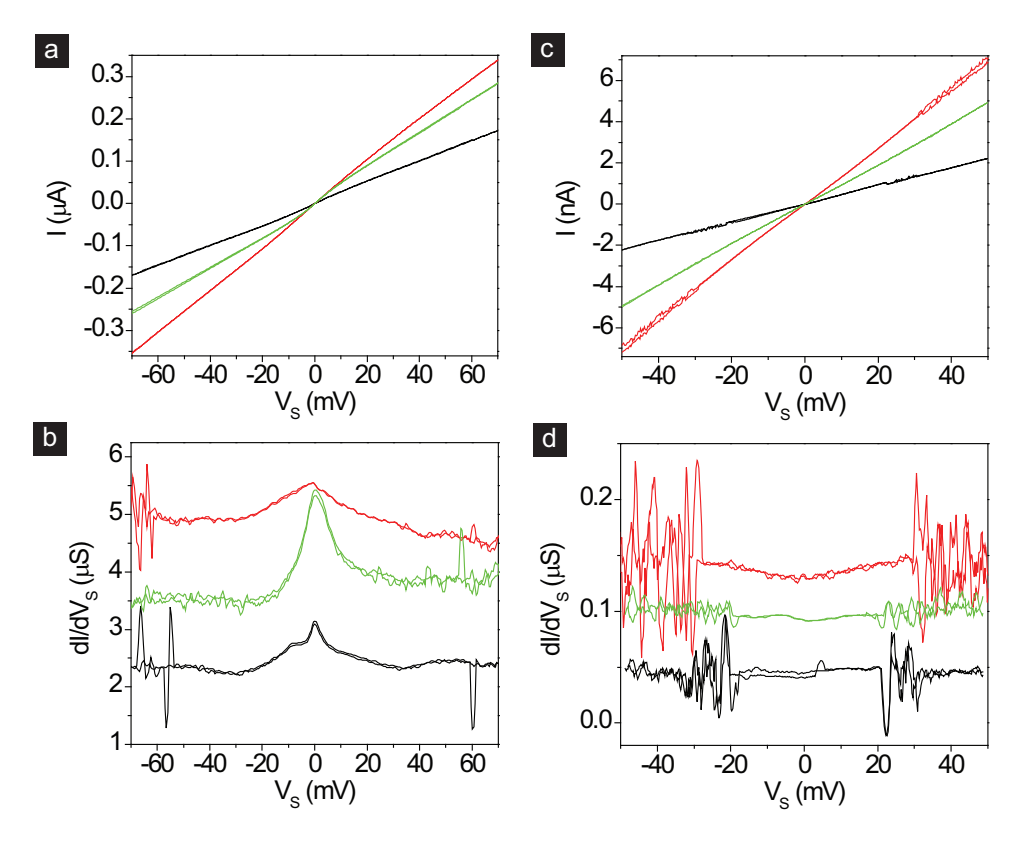


FIGURE 7.2: Current-voltage characteristics and differential conductance plots of MCBJs exposed to C_{60} (T=6.3 K). The differential conductance dI/dV was calculated by smoothing and differentiating the measurement data over 2.5 mV. Parts (a) and (b) display typical characteristics of junctions with an enhanced differential conductance at zero bias. Parts (c) and (d) illustrate bistabilities in junctions of C_{60} .

tional evidence. Nevertheless, we will continue our analysis in the framework of a S = 1/2 Kondo effect, which has been observed in earlier experiments on C_{60} [4, 8, 9].

Previously, the lineshape of the Kondo resonance in the differential conductance has been described by a Lorentzian peak above a constant background from elastic tunneling [4]:

$$\frac{dI}{dV} = G_{peak} \frac{\gamma^2}{V^2 + \gamma^2} + G_{el}. \tag{7.1}$$

Here G_{el} represents the background conductance due to elastic tunneling, G_{peak} corresponds to the enhancement of the differential conductance at zero bias, and 2γ is the full width at half maximum (FWHM) of the Lorentzian. The FWHM at T=0 K is linked to the energy scale of the Kondo effect, the Kondo temperature T_K , by the relation $\gamma \approx k_B T_K/e$ [4]. Fits of the measured characteristics at 6.3 K by Equation 7.1 allow us to obtain estimated Kondo temperatures from 25 K to 80 K. These are in good agreement with earlier measure-

ments on Au- C_{60} -Au junctions, which have yielded Kondo temperatures of 5 K [9] up to 100 K [8].

In addition to the zero-bias signatures, junctions of C_{60} often displayed fluctuations and bistabilities at bias voltages larger than 20 mV (see parts c and d of Figure 7.2). Their occurrence was highly sensitive to the electrode distance, and their position could shift during the fusing or the stretching of the junction. Similar instabilities in the bias range from 30 mV to 100 mV have been reported for C_{60} trapped between shadow-evaporated electrodes [6, 21]. They have been attributed to nanomechanical oscillations of the metal-molecule-metal junction, which may mediate a switching of the fullerene molecule between two configurations with different conductances. The lowest intra-cage vibration of C_{60} possesses an energy of 35 meV, which is beyond the onset of the switching in our junctions. However, vibrational modes of the metal-molecule bond, which can exhibit energies down to 5 meV [7], could be responsible for the instabilities in our experiments.

7.5 GATE-INDUCED TUNING OF ZERO-BIAS RESONANCES

We have studied the gate voltage dependence of the zero-bias peaks in a gated MCBJ with suspended source-drain electrodes. Measurements for two different junction configurations revealed qualitatively similar effects, namely a symmetric tuning of the resonance in gate voltage around $V_G=0$ V. In one case, however, the tuning was smooth, whereas the other measurement showed abrupt changes in the peak shape. In the following, we will discuss the characteristics that depended smoothly on gate voltage.

Figure 7.3a presents the differential conductance map of the junction. In addition to the resonance at zero bias, it exhibits instabilities around $V_S=\pm 20$ mV that are similar to the ones in Figure 7.2d. Overall, there seems to be little gate dependence. However, a closer investigation of selected dI/dV characteristics reveals a subtle gate effect (see Figure 7.3b): At high absolute gate voltages, the height of the zero-bias increases slightly. Furthermore, the instabilities at bias voltages of ± 20 mV disappear and pronounced dI/dV-noise beyond $V_S=\pm 30$ mV can be observed.

It is important to note that the evolution of the differential conductance is highly symmetric around $V_G=0$ V. This symmetry is reminiscent of the gate-induced tuning of the tunneling gaps in clean gated MCBJs that has been discussed in Chapter 6. Earlier experiments on C_{60} in MCBJs have shown that both the Kondo resonance and the signature of vibrational modes are very sensitive to changes in the electrode distance [4]. Accordingly, we attribute the symmetric gate dependence of the zero-bias resonance and the instabilities to an electromechanical actuation of the source-drain electrodes by the gate. In the following, we will provide additional evidence for this interpretation.

To explore the dependence of the zero-bias peak on the electrode distance, we have studied the evolution of the differential conductance during the stepwise bending of the substrate (see Figure 7.3c). With increasing distance of the source-drain electrodes the height of the zero-bias peak decreases, as does the nearly bias-independent background conductance. We have modeled each dI/dV spectrum in the series by a Lorentzian peak at zero bias and a constant contribution G_{el} from elastic tunneling (see Equation 7.1). The dotted line in Figure 7.3c presents an example of such a fit. Within the experimental error, the

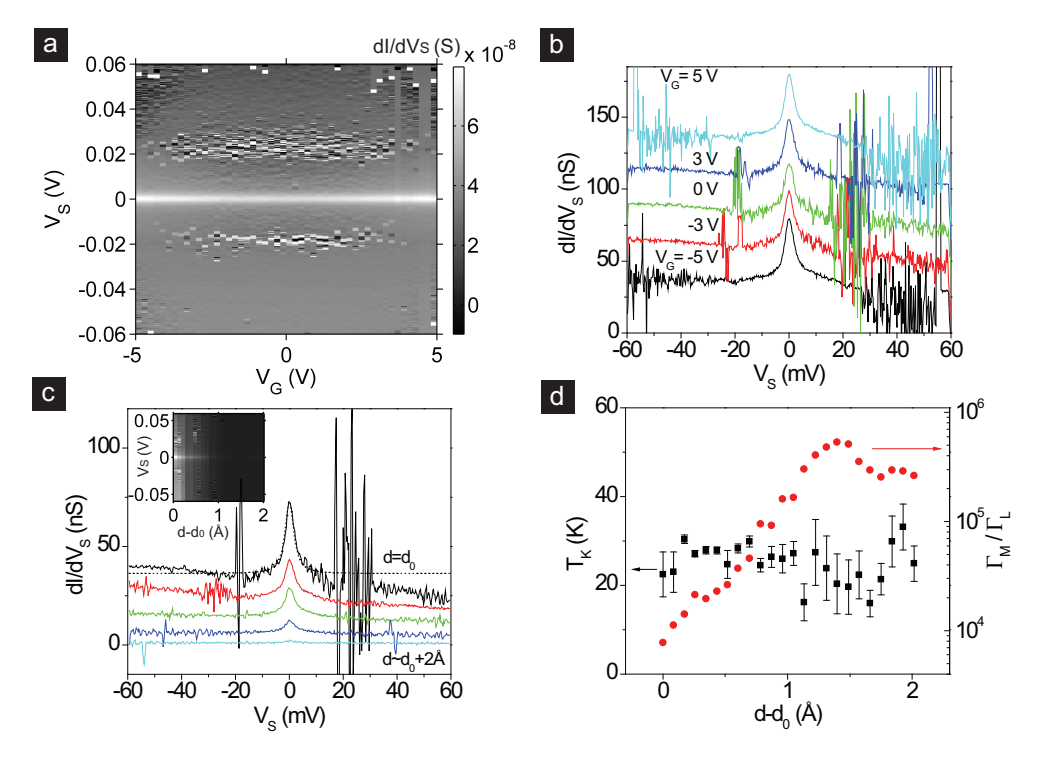


FIGURE 7.3: Details of the tuning of a zero-bias peak in the differential conductance of a junction of C_{60} (T=6.3 K). The derivative was calculated numerically after smoothing the measured IV characteristics over 1.2 mV. Distances were calculated from the substrate bending using a displacement ratio of $2.6 \cdot 10^{-5}$ (see Chapter 6). (a) Conductance map of the junction as a function of gate voltage and source-drain bias. (b) Selected dI/dV characteristics at different gate voltages. For clarity, the curves have been offset by 25nS. (c) Evolution of the differential conductance during the stretching of the junction. The dotted line is the result of a fit in the interval $V_S=\pm 18$ mV (see text). The inset presents a differential conductance map as a function of bias voltage and electrode distance. (d) Evolution of the Kondo temperature T_K and the coupling ratio Γ_L/Γ_M with electrode distance as obtained from fits of the dI/dV characteristics. The error bars give the 95% confidence interval.

fitting allows us to derive a Kondo temperature of 20-30 K that does not depend systematically on the electrode distance (see Figure 7.3d). The peak heights obtained from the fits enable us to determine the ratio of the electronic couplings to the electrodes according to

$$G_{max}(T) = G_0 \frac{4\Gamma_M \Gamma_L}{(\Gamma_M + \Gamma_L)^2} \left(1 + 2^{\frac{1}{s} - 1} \frac{T^2}{T_K^2} \right)^{-s} + G_{el}, \tag{7.2}$$

where s=0.22, and Γ_M and Γ_L are the electronic couplings to the more and less strongly coupled electrode, respectively. For an estimated junction temperature of T=6.3 K (measured on the moving sample support), we find a steady exponential increase in the coupling ratio Γ_M/Γ_L from about $8\cdot 10^3$ at $d=d_0$ to $4\cdot 10^5$ over a stretching of 1.2 Å. This evolution is comparable to earlier measurements of the Kondo effect in a junction of Γ_{60} [4]

with a similar peak height and width in dI/dV. The observation of a low conductance around $10^{-3}~G_0$, the stretching-induced increase in the coupling ratio, and the rather constant Kondo temperature are consistent with a very asymmetrically coupled junction. In this case, the increase in electrode distance only affects the weakly coupled contact and leads to a large increase in the coupling ratio. The Kondo temperature, which is determined by the more strongly coupled metal-molecule interface (see Chapter 2), remains unchanged. It is interesting to note that the coupling ratio decreases again for stretching distances beyond 1.4 Å. For a straight Au- C_{60} -Au junction, a complete breaking would be expected. Most likely, the junction geometry in our experiment is more complicated and leads to a sliding motion of the molecule along the less strongly coupled electrode.

The bending dependence of the zero-bias peak enables us to attribute the symmetric gate dependence in Figure 7.3 to an electromechanically induced fusing of the junction. As the absolute gate voltage is increased, the source-drain electrodes are attracted by the gate and their distance decreases. However, the effect of this actuation is very small compared to the bending-induced tuning in Figure 7.3c. This suggests a location of the molecule in the center of the electrode cross section (see Chapter 6). Such a geometry could also explain the absence of a clear electrostatic modulation of the resonance. In the case of a small intermediately coupled molecule located far from the bottom of the source-drain electrodes, the gate coupling can be expected to be negligible (see Chapter 2).

7.6 CONCLUSIONS

In conclusion, we have provided evidence of an intermediate coupling of C_{60} to the gold electrodes in our MCBJs. Pronounced plateaus around $10^{-2}\ G_0$ in the fusing characteristics of the junctions at room temperature and low-temperature features reminiscent of Kondo physics indicate a rather clean metal-molecule interface resulting from our controlled molecule deposition scheme. The adsorption of the molecules on the as-fabricated electrodes and the subsequent breaking in vacuum guarantee the exposure of clean gold surfaces for the formation of molecular junctions. This result also supports the applicability of fullerene-based anchoring groups for single-molecule measurement in vacuum.

REFERENCES

- [1] C. Joachim, J. K. Gimzewski, R. R. Schlittler, and C. Chavy, *Electronic Transparence of a Single C*₆₀ *Molecule*, Phys. Rev. Lett. **74**, 2102 (1995).
- [2] A. R. Champagne, A. N. Pasupathy, and D. C. Ralph, *Mechanically Adjustable and Electrically Gated Single-Molecule Transistors*, Nano Lett. **5**, 305 (2005).
- [3] T. Böhler, A. Edtbauer, and E. Scheer, Conductance of individual C_{60} molecules measured with controllable gold electrodes, Phys. Rev. B **76**, 125432 (2007).
- [4] J. J. Parks, A. R. Champagne, G. R. Hutchison, S. Flores-Torres, H. D. Abruña, and D. C. Ralph, *Tuning the Kondo Effect with a Mechanically Controllable Break Junction*, Phys. Rev. Lett. 99, 026601 (2007).

REFERENCES 111

[5] G. Schulze, K. J. Franke, and J. I. Pascual, *Resonant heating and substrate-mediated cooling of a single C*₆₀ *molecule in a tunnel junction*, New J. Phys. **10**, 065005 (2008).

- [6] A. V. Danilov, S. E. Kubatkin, S. G. Kafanov, and T. Bjørnholm, Strong electronic coupling between single C_{60} molecules and gold electrodes prepared by quench condensation at 4 K. A single molecule three terminal device study, Faraday Discuss. **131**, 337 (2006).
- [7] H. Park, J. Park, A. K. Lim, E. H. Anderson, P. A. Alivisatos, and P. L. McEuen, *Nanome-chanical oscillations in a single-C*₆₀ *transistor*, Nature **407**, 57 (2000).
- [8] L. H. Yu and D. Natelson, *The Kondo Effect in C*₆₀ *Single-Molecule Transistors*, Nano Lett. **4**, 79 (2004).
- [9] N. Roch, S. Florens, V. Bouchiat, W. Wernsdorfer, and F. Balestro, *Quantum phase transition in a single-molecule quantum dot*, Nature **453**, 633 (2008).
- [10] B. W. Hoogenboom, R. Hesper, L. H. Tjeng, and G. A. Sawatzky, Charge transfer and doping-dependent hybridization of C₆₀ on noble metals, Phys. Rev. B 57, 11939 (1998).
- [11] C.-T. Tzeng, W.-S. Lo, J.-Y. Yuh, R.-Y. Chu, and K.-D. Tsuei, *Photoemission, near-edge* x-ray-absorption spectroscopy, and low-energy electron-diffraction study of C_{60} on Au(111) surfaces, Phys. Rev. B **61**, 2263 (2000).
- [12] E. I. Altman and R. J. Colton, *Nucleation, growth, and structure of fullerene films on Au(111)*, Surf. Sci. **279**, 49 (1992).
- [13] N. Sergueev, D. Roubtsov, and H. Guo, (unpublished), URL http://arxiv.org/abs/ cond-mat/0309614v1.
- [14] M. Kiguchi and K. Murakoshi, *Conductance of Single C*₆₀ *Molecule Bridging Metal Electrodes*, J. Phys. Chem. C **112**, 8140 (2008).
- [15] S. Yoshimoto, R. Narita, E. Tsutsumi, M. Matsumoto, K. Itaya, O. Ito, K. Fujiwara, Y. Murata, and K. Komatsu, *Adlayers of Fullerene Monomer and* [2 + 2]-Type Dimer on Au(111) in Aqueous Solution Studied by in Situ Scanning Tunneling Microscopy, Langmuir 18, 8518 (2002).
- [16] S. Uemura, P. Samory, M. Kunitake, C. Hirayamaa, and J. P. Rabe, *Crystalline C*₆₀ *monolayers at the solid–organic solution interface*, J. Mater. Chem. **12**, 3366 (2002).
- [17] A. Kuzume, E. Herrero, J. M. Feliu, R. J. Nichols, and D. J. Schiffrin, Fullerene monolayers adsorbed on high index gold single crystal surfaces, Phys. Chem. Chem. Phys. 6, 619 (2004).
- [18] D. Goldhaber-Gordon, H. Shtrikman, D. Mahalu, D. Abusch-Magder, U. Meirav, and M. A. Kastner, *Kondo effect in a single-electron transistor*, Nature **391**, 156 (1998).

- [19] S. M. Cronenwett, T. H. Oosterkamp, and L. P. Kouwenhoven, *A Tunable Kondo Effect in Quantum Dots*, Science **281**, 540 (1998).
- [20] M. R. Calvo, J. Fernandez-Rossier, J. J. Palacios, D. Jacob, D. Natelson, and C. Untiedt, *The Kondo effect in ferromagnetic atomic contacts*, Nature **458**, 1150 (2009).
- [21] A. V. Danilov, P. Hedegård, D. S. Golubev, T. Bjørnholm, and S. E. Kubatkin, *Nanoelectromechanical Switch Operating by Tunneling of an Entire C*₆₀ *Molecule*, Nano Lett. **8**, 2393 (2008).

TRANSPORT IN MECHANICALLY STABLE GATED MCBJS

This chapter reports on a new fabrication process for gated mechanically controllable break junctions. The devices are based on a direct deposition of the source and the drain electrodes on an aluminium gate. The plasma-enhanced native oxide on the aluminium electrode serves as the gate insulator and enables measurements at gate voltages up to 1.8 V. Throughout the bending-controlled tuning of the source-drain distance, the electrical continuity of the gate electrode is maintained. A nanoscale island in the Coulomb blockade regime serves as a first experimental test system for the devices, in which the mechanical and electrical control of charge transport is demonstrated.

This chapter will be part of a forthcoming publication.

8.1 Introduction

During recent years, the field of molecular electronics has experienced a tremendous increase in experimental techniques. Two-terminal measurements on single molecules can now be carried out using scanning tunneling microscopes (STMs), mechanically controllable break junctions (MCBJs), or conducting AFMs (CAFMs). Break junction-type measurements at a fixed bias voltage allow us to study the statistics of the low-bias conductance [1] and the time-dependent evolution [2, 3] of single-molecule junctions for hundreds of different configurations of the metal-molecule interface. Statistical measurements of current-voltage characteristics, in turn, can yield some information on the electronic level structure of molecular junctions [4, 5]. Vibrational modes can be revealed by inelastic tunneling spectroscopy (IETS) at low temperatures [6, 7].

Despite this wealth of experimental techniques, the amount of information that can be extracted from two-terminal measurements is still limited. Some interesting characteristics of molecular junctions, such as the electronic level spacing and the dependence of the electron-vibron coupling on the charge state of the molecule, can only be obtained by modulating the potential on the molecule with a gate electrode.

To ensure a large electrostatic coupling of the molecular junction to the gate, almost all three-terminal studies to date have employed the electromigration method. Here, a thin metal wire is deposited directly on top of a gate electrode and broken by means of a high current [8] and, in some cases, thermal activation [9, 10]. This method is hampered by the statistical nature of the electromigration process, which prevents a precise control of the gap between the two resulting electrodes and leads to low yields of molecular junctions around a few percent [11]. Moreover, it has been shown that electromigration can lead to the formation of gold clusters in the source-drain gap, the spectroscopic signature of which can be similar to molecular junctions [11]. Hence, it remains a major challenge to unambiguously attribute the transport characteristics in three-terminal measurements to a single molecule between the electrode pair. At sufficiently low temperatures, the spectroscopic 'fingerprint' of low-energy excitations can be compared to infrared and Raman absorption spectra to confirm the presence of a molecule in the junction [12].

The ability to control the spacing of the source-drain electrode pair offers an elegant solution to the drawbacks of electromigration. If an electrode gap can be formed by mechanical breaking alone, excessive heating and the formation of nanoscale clusters can be avoided. Furthermore, the control over the gap enables in-depth studies of the influence of the metal-molecule coupling on the charge transport characteristics of a molecular junction. To date, gating with mechanical control has been demonstrated in a STM [13] and in gated mechanically controllable break junctions on ultra-thin silicon [14]. In the latter case, the highly doped substrate served as the back gate for a pair of suspended source-drain electrodes. To prevent the brittle devices from breaking, the mechanical control in the gated MCBJs had to be limited to an electrode displacement of a few angstroms. Hence, the junctions were fully or partially broken by electromigration before studying single-molecule transport.

In Chapter 6, a fabrication process for gated MCBJs on flexible phosphor bronze substrates has been presented. It has been shown that the as-fabricated suspended electrode pair can

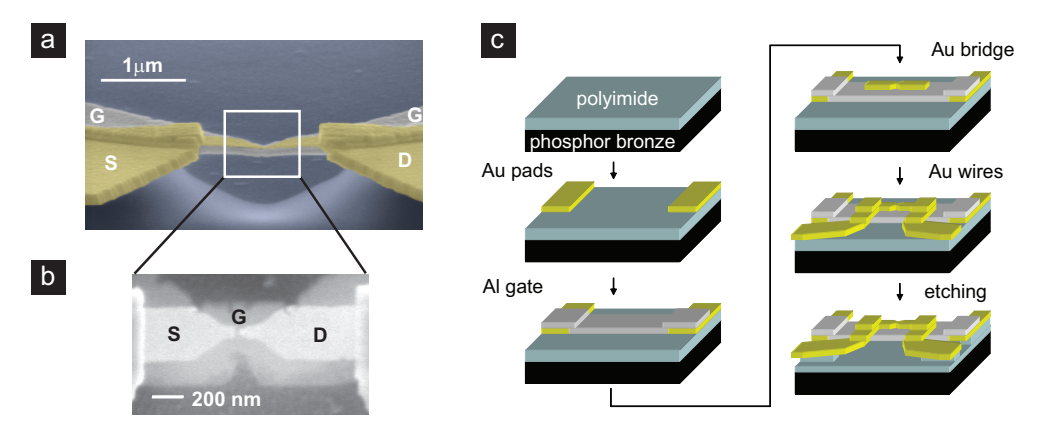


FIGURE 8.1: (a) Scanning electron micrograph of a gated MCBJ (colorized for clarity) (b) Detail of the contact area. The gold bridge has been broken, whereas the gate electrode is still continuous. (c) Schematic of four out of five steps in the microfabrication process. Each pattern is written by electron-beam lithography before evaporation and lift-off.

be broken by bending alone. However, the suspended source-drain electrodes are intrinsically susceptible to electromechanical actuation by the gate, which may lead to a convolution of mechanical and electrostatic tuning in molecular junctions. In this chapter, we report on gated MCBJs that can be broken by bending, that have mechanically stable source-drain electrodes, and that possess a potentially high gate coupling.

8.2 EXPERIMENTAL DETAILS

The fabrication process of the gated MCBJs combines a plasma-oxidized aluminium gate with a pair of thin gold electrodes in a sandwich architecture, similar to three-terminal devices used in electromigration-based measurements [15]. A side view of a typical gated MCBJ is presented in Figure 8.1a. The structure is suspended above a flexible phosphor bronze substrate with a polyimide coating, comparable to two-terminal MCBJs [16]. Figure 8.1b presents a top view of the active area of the gated device. The gold electrodes, which are located directly on the wide and thick gate, can be broken and rejoined upon bending the substrate. The details of the mechanical response of the source-drain spacing will be discussed later.

The fabrication of the gated MCBJs builds on the batch process for two-terminal junctions that has been described in Chapter 3. Initially, phosphor bronze wafers are polished, cleaned thoroughly, and coated with an insulating and planarizing polyimide layer of about 3 μ m thickness (PI2610, HD Microsystems). The devices on these wafers are then fabricated by repeated spin-coating of double-layer resist (MMA/MAA copolymer and PMMA 950k), patterning with high-resolution e-beam lithography, evaporation of metal layers, and lift-off in hot acetone. Each substrate contains two electrically isolated gated junctions.

Figure 8.1c presents an overview of the different structural layers of the gated MCBJs. In

the first step we fabricate lithography markers (2 nm Ti followed by 130 nm Au, not shown) on the bare wafers. Subsequently, two thin connector pads (3 nm Cr and 37 nm Au) are aligned with respect to these markers. These pads establish a metallic connection between the aluminium gate and the large access wires of the gated MCBJ. In the following step, the aluminium gate (1 nm Ti and 60 nm Al, evaporated at a base pressure of $5 \cdot 10^{-7}$ mbar and a speed of 0.1 nm/s) is aligned with the pads. It is known that aluminium surfaces form a native oxide layer when exposed to ambient atmosphere [17, 18]. However, we found that the quality of the native oxide that forms on our evaporated gate structures is insufficient for reliable electrical isolation. To increase the strength of the native aluminium oxide, the wafers are exposed to a high-power oxygen plasma in a reactive ion etcher (O₂ flow 20 sccm, pressure 0.1 mbar, RF power 150 W, duration 10 s). This treatment has been used earlier for the formation of several nanometers of aluminium oxide [19, 20] and is sufficient for the electrical isolation of the gate from the source and the drain electrodes. On top of the gate, a thin gold bridge with a 40 nm-wide constriction is patterned. Before the evaporation of the bridge structure (20 nm Au) the surface of the gate is cleaned by reactive ion etching in an oxygen plasma (O_2 flow 20 sccm, pressure 3 μ bar, RF power 50 W, duration 15 s). This so-called descum step removes resist residue from the gate surface and ensures the adhesion and the cleanliness of the bare gold bridge. In the last patterning step, large wires and contact pads (2 nm Ti and 170 nm Au) are deposited to electrically access the gold bridge and the gate electrode. It is important to deposit wires that are much thicker than the metallic structures they contact in order to ensure a good step coverage and a continuous electrical connection. The fabrication of the gated MCBJs is completed by dry etching in a reactive ion plasma of CF₄ and O₂ (flow rate ratio 6:50 sccm, pressure 0.2 mbar, RF power 30 W). This leads to the suspended structure that is depicted in Figure 8.1a.

8.3 MECHANICAL AND ELECTRICAL CHARACTERIZATION OF THE DEVICES

To test the performance of the gated MCBJ architecture, we have studied a clean device at both room temperature and at 7 K. We found that the gold bridge can be stretched and broken without destroying the gate electrode. Parts a and c of Figure 8.2 present the breaking and fusing characteristics of the same device at room and cryogenic temperatures, respectively. As in two-terminal MCBJs, the conductance of the source-drain electrode pair decreases upon bending the substrate. The electrodes exhibit a jump out of contact after the last conductance plateau at 1 G_0 and an exponential conductance decay in the tunneling regime. The steady series resistance of the gate electrode and a 100 M Ω protective resistor confirms that the gate is not broken during the tuning of the source-drain distance. During the fusing of the junction at room temperature, a rather large backlash and a deviation from the exponential tunneling dependence can be observed. These must be attributed to the experimental conditions: The mobility of the gold at room temperature may lead to a retraction of the electrodes after breaking and an apparent mechanical backlash that is absent at cryogenic temperatures (see Figure 8.2c). The smaller conductance slope and the slight plateau formation in the fusing characteristics at room temperature

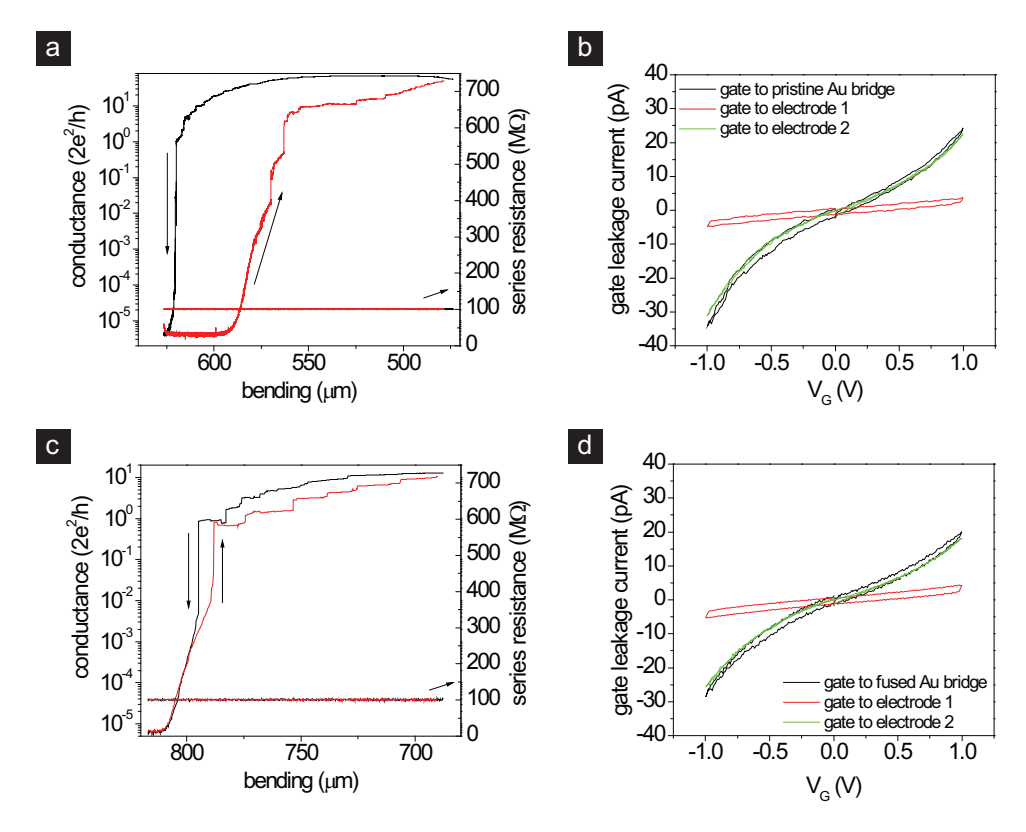


FIGURE 8.2: (a) Breaking and fusing characteristics of a clean gated MCBJ at room temperature and at a bias voltage of 50 mV. The large arrows indicate the direction of the junction actuation. The conductance of the gold bridge was monitored simultaneously with the series resistance of the gate and a $100~\mathrm{M}\Omega$ resistor while bending the substrate at a speed of 2 μ m/s. (b) Leakage characteristics from the gate electrode to the as-fabricated gold bridge and each of the electrodes after breaking. The measurement was again carried out with a protective $100~\mathrm{M}\Omega$ series resistor. (c) and (d) Breaking and fusing characteristics and gate leakage at a temperature of 7 K.

could be due to the adsorption of gaseous impurities from the vacuum environment [21]. This observation may have implications for single-molecule measurements. To reliably form single-molecule junctions the cleanliness of the molecule-electrode interface needs to be guaranteed, either through a strong physico-chemical bond or through breaking in cryogenic vacuum.

At cryogenic temperatures the conductance typically increases exponentially during the fusing of the junction, confirming the cleanliness of the electrode surfaces. We have determined the displacement ratio from the tunneling slope of 20 fusing characteristics of the clean device in the conductance regime from 10^{-4} to 10^{-3} G_0 . The analysis yields a ratio of $r = \partial d/\partial w \approx 1.5 \cdot 10^{-5}$, which is smaller than, but on the same order as, the value in 2-terminal devices (see Chapter 3). Most likely, the actuation of the source-drain electrode pair independent of the underlying gate electrode is enabled by both the geometry

and the combination of materials in the gated MCBJs. The larger thickness prevents the gate electrode from breaking as the substrate is bent. The gold bridge, in contrast, has been designed for a larger strain concentration and breaks at its smallest cross section (see Figure 8.1b). Besides, the absence of an adhesion layer may facilitate a sliding motion on top of the aluminium oxide, either very locally or along the entire bridge.

It is important to note that the initial cross section of the source-drain bridge determines the performance of the gated MCBJs. In the device presented in Figure 8.2, the bridge was first broken at room temperature, leading to a slight retraction of the electrodes. During the cooling to 6 K the device was then held at a conductance of $10\,G_0$. Breaking the corresponding thin gold bridge requires only a small bending range and protects the gate. For another device that was cooled down in the as-fabricated state, a much larger substrate bending was required to break the source-drain electrode pair, resulting in a rupture of the gate electrode. However, even a ruptured gate may still be used for electrical gating if the source-drain gap is located above the same part of the gate electrode. Experimentally, a tunneling current from one part of the gate to both the source and the drain electrodes can confirm such a geometrical overlap.

The quality of the plasma-grown aluminium oxide in the gated MCBJs was found to be sufficient for three-terminal measurements. In contrast to gated MCBJs with suspended source-drain electrodes (see Chapter 6), the sandwich-type devices did not show any gate effect on the junction conductance in the tunneling regime. In a total of six devices we measured a room-temperature leakage current of 40 ± 17 pA at a gate voltage of 1 V. Figure 8.2b presents a plot of the room-temperature leakage current from the gate to the asfabricated gold bridge as well as to each electrode after breaking. The currents to electrode 1 and 2 differ significantly, indicating a large influence of the local insulator characteristics on the leakage. The barrier heights and thicknesses that can be obtained from a fit of the Simmons model of tunneling (see Chapter 2) to the characteristics in Figure 8.2b differ from the typical values for plasma-enhanced aluminium oxide films (2.6 eV [17] and 4 nm [20]). Furthermore, the leakage current at cryogenic temperatures is slightly reduced (see Figure 8.2d). These observations suggest that electron emission from rough regions of the gate electrode and transport along thermally activated defect paths in the oxide contribute to the leakage current. Despite these shortcomings, the oxide was found to be stable enough for three-terminal measurements on molecular junctions at gate voltages of up to 1.8 V.

8.4 BENDING-CONTROLLED COULOMB BLOCKADE

To establish the mechanical and electrical control of transport in the gated MCBJs we studied two devices exposed to C_{60} and a OPV3 derivative [22], respectively. Three-terminal measurements of these molecules have previously revealed Coulomb blockade characteristics [14, 22, 23]. In the gated MCBJs, the source-drain electrodes were exposed to dilute solutions (0.01-0.1 mM) of the molecules in toluene, broken by bending the flexible substrates at room temperature, and then cooled to 7 K.

Since we did not observe Coulomb blockade in either of the devices, we fused the gold bridges to conductances of more than 10 G_0 to ensure a clean contact area and applied a

voltage ramp to deliberately perform electromigration at cryogenic temperatures. When carried out rapidly and without a feedback on the junction conductance, the electromigration process can lead to extensive Joule heating and the spontaneous formation of gold clusters in the electrode gap [24]. Depending on the local junction geometry, these gold clusters can exhibit Coulomb blockade features similar to those of single molecules. In three-terminal measurements with electromigrated source-drain electrodes it is hence necessary to unambiguously relate the detected spectroscopic features to the molecule under investigation [25]. In our case, however, the particles may serve as a useful test case for Coulomb blockade transport.

Since not every voltage ramp forms islands that contribute to transport, we repeatedly electromigrated and fused the junctions until we observed gate-dependent transport characteristics. In contrast to regular electromigration devices our gated MCBJs allow us to reestablish the contact by relaxing the bending of the substrate. A new electromigration run can then be used to break the contact again.

In both gated MCBJs that were subjected to electromigration, we have observed mechanically tunable Coulomb blockade characteristics. Most likely, these can be attributed to gold clusters in the gap. However, we cannot exclude that we in fact probed a single molecule. In the following, we will hence refer to the object in the electrode gap as an island. The electrode distance in one of the gated MCBJs (the one previously exposed to C_{60}) could be tuned such that it exhibited a degeneracy point in the accessible gate voltage window. In the remainder of this chapter, this device will be discussed in more detail.

Figure 8.3a presents the three subsequent IV characteristics of the source-drain electrode pair during the electromigration process. As the bias voltage is increased, the current increases superlinearly. The underlying increase in bridge conductance may be due to an annealing of the metal bridge by Joule heating. Above a certain voltage, the current drops spontaneously below the detection limit, sometimes via intermediate steps. This conductance drop indicates the successful formation of an electrode gap. The removal of gold atoms at high currents has led to a steady reduction of the cross section, a decrease in conductance, and, eventually, the breaking of the gold bridge.

After the third electromigration run, mechanically tunable and gate-dependent transport characteristics could be observed. Figure 8.3b presents plots of the source-drain current (black) and differential conductance (red) as a function of the gate voltage. Within the framework of Coulomb blockade the peaks at $V_G = 1.7 \, \mathrm{V}$ can be ascribed to a nanoscale island between the source-drain electrodes. They correspond to a degeneracy point, where Coulomb blockade is lifted and sequential tunneling through the island is allowed.

Parts c-f of Figure 8.3 present the differential conductance maps of the gateable island for a series of different source-drain distances. A detailed discussion of the characteristics will follow below. All of the stability diagrams exhibit black regions around zero bias where the current is suppressed; the island is in Coulomb blockade. These regions are framed by upward and downward sloped lines that mark the transition to sequential tunneling transport through the island.

In all stability diagrams, at least one additional, diagonal line with a large positive slope can be observed. Comparable features have recently been attributed to the presence of a

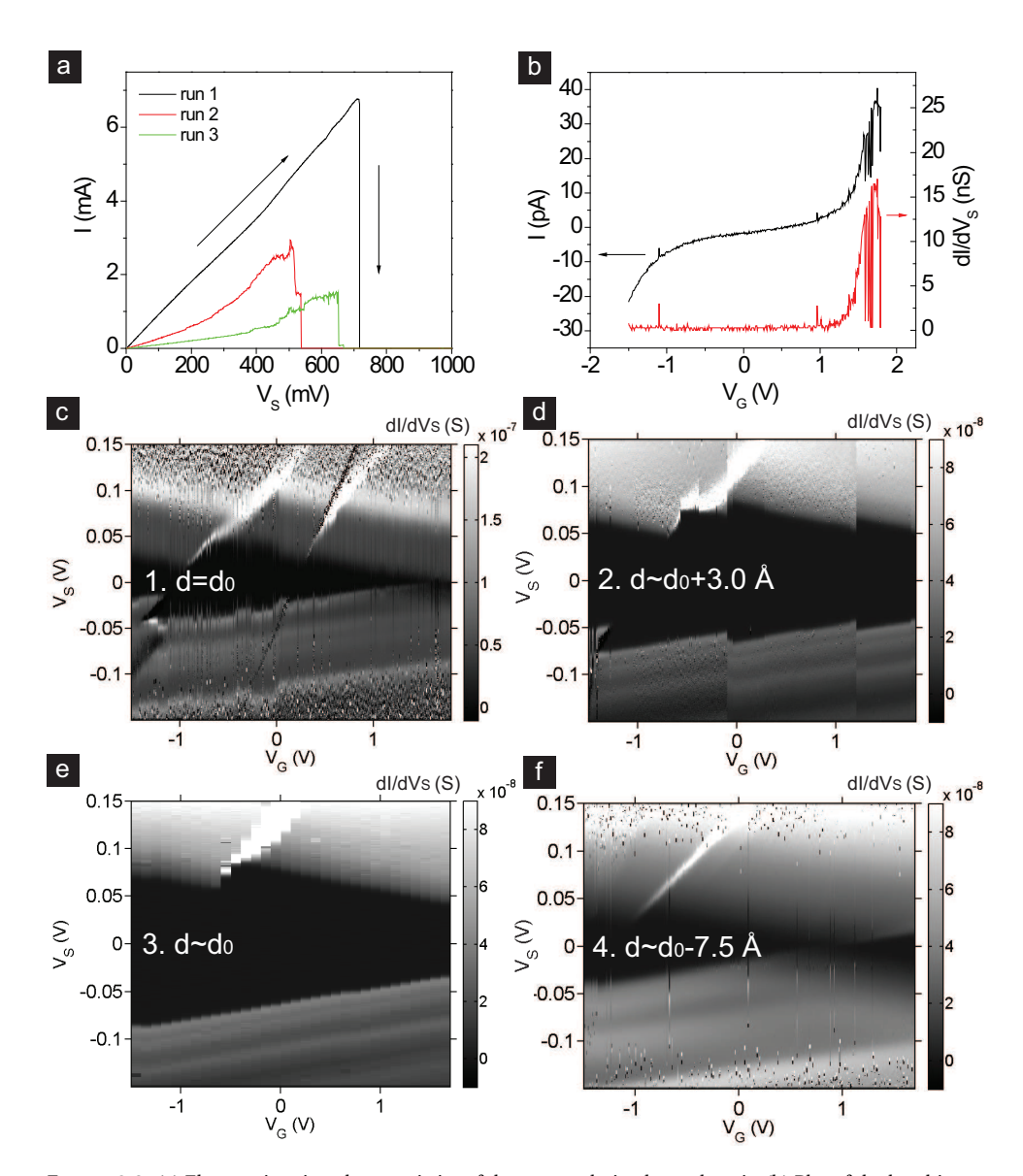


FIGURE 8.3: (a) Electromigration characteristics of the source-drain electrode pair. (b) Plot of the low-bias current and the numerical differential conductance at $V_S \approx 1$ mV as a function of gate voltage V_G . (c)-(f) Evolution of the differential conductance dI/dV_S during the mechanical stretching (c-d) and the subsequent fusing (d-f) of the source-drain electrode pair. The electrode distances have been derived from the substrate bending using a displacement ratio of $1.5 \cdot 10^{-5}$ (see previous section). The numerical derivatives were determined from a pointwise linear fit of IV measurements over a bias interval of 4.2 mV.

second, parallel island between the source-drain electrodes [26]. If the two islands in the gap are capacitively coupled, the charging of one island may influence the local potential on the other and lead to various features in the stability diagram of the junction. The shift in the local potential is particularly apparent in Figure 8.3c, where the size of the Coulomb gap around $V_G = -1$ V changes abruptly at the diagonal line. In the following, we will ignore these features and restrict our discussion to large and positive gate voltages where the state of the main island is unaffected.

As the distance between the electrodes is modified, the stability diagrams change significantly. In the first diagram in Figure 8.3c, a degeneracy point at a gate voltage of about 1.7 V can be observed. When the electrode distance is increased by approximately 3 Å, the degeneracy point shifts to more positive gate voltages, leaving only a small part of the charging diamond in the accessible measurement window. The stability diagram in Figure 8.3d shows two abrupt changes at $V_G = -0.1 \text{ V}$ and 1.2 V. At these switching events, the Coulomb gap changes, but the slopes β and $-\gamma$ of the diamond edges remain similar. The switching must be due to rearrangements in the electrostatic environment, consistent with the earlier interpretation of all characteristics in terms of parallel islands. As the source-drain distance is decreased to its initial value (see Figure 8.3e), the original stability diagram is not recovered. Apparently, the electrode motion has led to a permanent rearrangement of the charged impurities. However, the observed shift of the degeneracy point is recovered qualitatively as the electrode distance is decreased by another 7.5 Å (see Figure 8.3f). In between these measurements the electrode distance was decreased in steps on the order of 1.5 Å. With the exception of two switching events (with a smaller extent than the ones in Figure 8.3d), the stability diagrams evolved smoothly between parts e and f of Figure 8.3.

Mechanically induced changes of the conductance gap in Coulomb-blockade transport have been observed in gated MCBJs bridged by a C_{60} molecule [14] and in two-terminal measurements on metal clusters in STMs [27, 28]. In those earlier studies, the shift of the degeneracy point ΔV_{deg} has been attributed to an offset in the chemical potential of the level on the island,

$$\Delta V_{deg} = \epsilon \frac{\Delta C_S + \Delta C_D}{C_G},\tag{8.1}$$

where ϵ is the position of the level relative to the chemical potentials on the leads, and C_{α} with $\alpha = S, D, G$ are the capacitances from the island to the source, the drain, and the gate, respectively. Changes of ΔC_{α} in the capacitances with distance may then shift the degeneracy point.

In our measurements, the slopes β and $-\gamma$ of the positive and negative diamond edges in the stability diagrams allow us to extract the ratios of the device capacitances, but not their

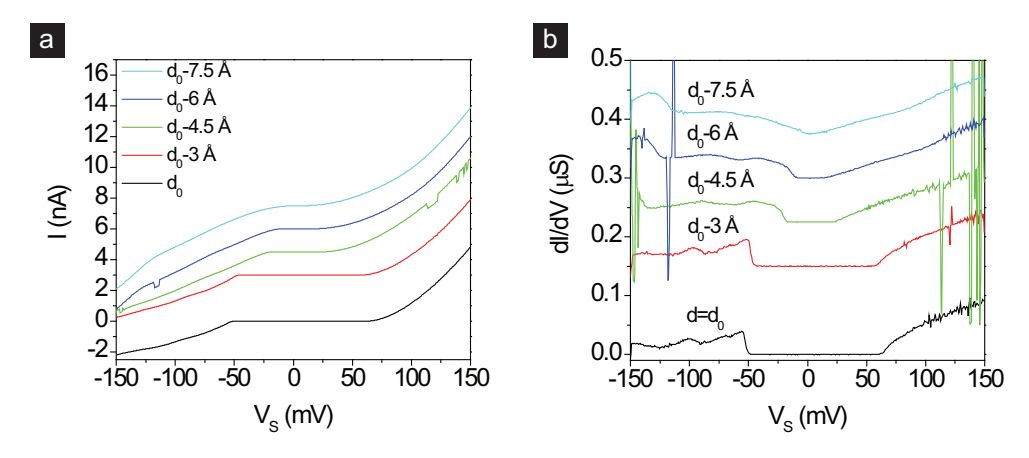


FIGURE 8.4: (a) Current-voltage characteristics of the junction at a gate voltage of $V_G = 0.5$ V and for different electrode distances. (b) Numerical differential conductance of the data in part a. The derivative was calculated over a bias interval of about 1.2 mV. All data have been offset as a function of electrode fusing (by 1 nA/Å and 50 nS/Å, respectively).

absolute values. For parts c-f of Figure 8.3 we find that

$$\frac{C_S}{C_G} \approx [53.5, 40.8, 48.8, 44.2],$$
 (8.2)

$$\frac{C_D}{C_C} \approx [64.5, 56.8, 54.3, 54.3], \text{ and}$$
 (8.3)

$$\frac{C_S}{C_G} \approx [53.5, 40.8, 48.8, 44.2],$$

$$\frac{C_D}{C_G} \approx [64.5, 56.8, 54.3, 54.3], \text{ and}$$

$$\frac{C_G}{C_S + C_D + C_G} \approx [0.0084, 0.0101, 0.0096, 0.0101].$$
(8.4)

Within the experimental error, there is no clear trend in the evolution of the capacitance ratios with distance.

In the remainder of this section, we will discuss the evolution of the junction characteristics between the situations depicted in parts e and f of Figure 8.3. The degeneracy points in these two stability diagrams can be determined directly from the data or from an extrapolation of the diamond edges, respectively. We obtain $\Delta V_{deg} \approx 0.8 \ V - 3.4 \ V =$ -2.6~V and, using the gate couplings given above, a modulation of the level position ϵ from 32.6 to 8.1 meV. Using Equation 8.1, this translates into a change in capacitances $(\Delta C_S + \Delta C_D)/C_G \approx -0.25$. This value is much smaller than the observed variation between the different stability diagrams; furthermore, the shift of the degeneracy point follows a systematic trend that is not seen in the capacitance ratios. Hence, the origin of the shift must differ from the capacitance-controlled offset potential that was discussed in earlier studies [14, 27, 28].

A possible alternative explanation for the observed characteristics could lie in a mechanically induced change of the electronic coupling of the island. In the remainder of this section, we will analyze the device characteristics in this respect.

As noted before, the similar slopes of the charging diamonds in parts e and f of Figure 8.3

8.5. CONCLUSIONS 123

allow us to deduce a stretching-independent and rather symmetric capacitive coupling in the device. Information on the electronic coupling to the source and the drain electrode, in turn, can be obtained from the areas of the stability diagrams where the Coulomb blockade is lifted.

The sequential tunneling regime below the positive edge of the charging diamond in Figure 8.3e shows two parallel lines. These may be attributed to electronic or vibrational excitations that increase the device current by opening up an additional transport channel (see Chapter 2). The fact that the lines are only resolved at negative bias voltages indicates a significantly stronger electronic coupling of the island to the drain electrode [29].

Studies of the Kondo effect in C_{60} have suggested that the mechanical tuning of junctions with asymmetric electronic coupling mainly affects the weakly coupled metal-molecule interface [30]. Accordingly, we can assume that the decrease in electrode distance increases the coupling to the source, whereas the coupling to the drain remains similar.

Following these lines, it is useful to investigate the details of the junction evolution between parts e and f of Figure 8.3. Figure 8.4a presents the current-voltage characteristics of the junction at a gate voltage of 0.5 V for decreasing electrode distances. All measurements indicate a suppression of the current at low bias voltages, indicative of Coulomb blockade. Furthermore, the differential conductance plots in Figure 8.4b reveal details of the resonances in the sequential tunneling regime: The characteristics for $d=d_0$ exhibit a peak at -56 mV, a shoulder at -69 mV and a broad peak at -100 mV, whereas the differential conductance increases smoothly for positive bias voltages. As the electrode distance decreases, a reduction of the conductance gap and a significant broadening of the three resonances at negative bias can be observed.

These observations suggest an increasing hybridization of the electronic level on the island with the states on the electrodes, which is consistent with a modification of the electronic coupling to the source by the mechanical actuation. As the distance between the electrodes is reduced, the coupling to the source increases, leading to level broadening, fractional charging, and a shift of the level towards the Fermi energy of the electrodes.

However, it is unclear why the capacitive coupling remains roughly constant over a tuning distance of several angstroms. Theoretically, the increasing hybridization with the source can be expected to lead to a rearrangement of the electron distribution on the island and a change in the capacitances of the device. Possibly, the strongly coupled contact to the drain dominates the electrostatics of the island so that the effect of the motion on its capacitive couplings is limited.

8.5 CONCLUSIONS

In this chapter, we have established a fabrication scheme for mechanically stable gated MCBJs. The combination of a plasma-oxidized aluminium gate with a thin gold bridge allows for the independent tuning of the distance between the source-drain electrodes at room temperature and at liquid helium temperatures, provided that the cross section of the electrodes is small. We have demonstrated the electrostatic and mechanical tuning of the Coulomb blockade characteristics of an island that was formed during electromigration. Thus far, the aluminium oxide insulator allows for the application of gate voltages up

to 1.8 V; the oxidation of the as-evaporated gate in pure oxygen [19] or the deposition of a self-assembled monolayer of aliphatic phosphonic acids [20] may lead to a further improvement in the leakage characteristics. Finally, a reduction of the cross section of the gold bridge may decrease the bending range required for breaking and ensure the continuity of the gate in all measurements at cryogenic temperatures. While we have not yet been able to demonstrate the simultaneous mechanical and electrical control of a single-molecule junction, the devices discussed here will enable thorough studies of molecular transport in the near future.

REFERENCES

- [1] B. Xu and N. J. Tao, *Measurement of Single-Molecule Resistance by Repeated Formation of Molecular Junctions*, Science **301**, 1221 (2003).
- [2] C. A. Martin, D. Ding, J. K. Sørensen, T. Bjørnholm, J. M. van Ruitenbeek, and H. S. J. van der Zant, *Fullerene-based anchoring groups for molecular electronics*, J. Am. Chem. Soc. **130**, 13198 (2008).
- [3] M. Kamenetska, M. Koentopp, A. C. Whalley, Y. S. Park, M. L. Steigerwald, C. Nuckolls, M. S. Hybertsen, and L. Venkataraman, *Formation and Evolution of Single-Molecule Junctions*, Phys. Rev. Lett. 102, 126803 (2009).
- [4] E. Lörtscher, H. B. Weber, and H. Riel, *Statistical Approach to Investigating Transport through Single Molecules*, Phys. Rev. Lett. **98**, 176807 (2007).
- [5] C. A. Martin, D. Ding, H. S. J. van der Zant, and J. M. van Ruitenbeek, *Lithographic mechanical break junctions for single-molecule measurements in vacuum: possibilities and limitations*, New J. Phys. **10**, 065008 (2008).
- [6] R. H. M. Smit, Y. Noat, C. Untiedt, N. D. Lang, M. C. van Hemert, and J. M. van Ruitenbeek, *Measurement of the conductance of a hydrogen molecule*, Nature **419**, 906 (2002).
- [7] J. Hihath, C. R. Arroyo, G. Rubio-Bollinger, N. Tao, and N. Agraït, *Study of Electron-Phonon Interactions in a Single Molecule Covalently Connected to Two Electrodes*, Nano Lett. **8**, 1673 (2008).
- [8] H. Park, A. K. L. Lim, A. P. Alivisatos, J. Park, and P. L. McEuen, *Fabrication of metallic electrodes with nanometer separation by electromigration*, Appl. Phys. Lett. **75**, 301 (1999).
- [9] K. O'Neill, E. A. Osorio, and H. S. J. van der Zant, *Self-breaking in planar few-atom Au constrictions for nanometer-spaced electrodes*, Appl. Phys. Lett. **90**, 133109 (2007).
- [10] F. Prins, T. Hayashi, B. J. A. de Vos van Steenwijk, B. Gao, E. A. Osorio, K. Muraki, and H. S. J. van der Zant, *Room-temperature stability of Pt nanogaps formed by self-breaking*, Appl. Phys. Lett. **94**, 123108 (2009).

References 125

[11] H. S. J. van der Zant, Y.-V. Kervennic, M. Poot, K. O'Neill, Z. de Groot, J. M. Thijssen, H. B. Heersche, N. Stuhr-Hansen, T. Bjørnholm, D. Vanmaekelbergh, et al., *Molecular three-terminal devices: fabrication and measurements*, Faraday Discuss. 131, 347 (2006).

- [12] E. Osorio, K. O'Neill, N. Stuhr-Hansen, O. F. Nielsen, T. Bjørnholm, and H. S. J. van der Zant., *Addition Energies and Vibrational Fine Structure Measured in Electromigrated Single-Molecule Junctions Based on an Oligophenylenevinylene Derivative*, Adv. Mater. **19**, 281 (2007).
- [13] E. S. Soldatov, V. V. Khanin, A. S. Trifonov, D. E. Presnov, S. A. Yakovenko, G. B. Khomutov, C. P. Gubin, and V. V. Kolesov, *Single-electron transistor based on a single cluster molecule at room temperature*, JETP Letters **64**, 556 (1996).
- [14] A. R. Champagne, A. N. Pasupathy, and D. C. Ralph, *Mechanically Adjustable and Electrically Gated Single-Molecule Transistors*, Nano Lett. **5**, 305 (2005).
- [15] Y. V. Kervennic, D. Vanmaekelbergh, L. P. Kouwenhoven, and H. S. J. van der Zant, *Planar nanocontacts with atomically controlled separation*, Appl. Phys. Lett. **83**, 3782 (2003).
- [16] J. M. van Ruitenbeek, A. Alvarez, I. Piñeyro, C. Grahmann, P. Joyez, M. H. Devoret, D. Esteve, and C. Urbina, *Adjustable nanofabricated atomic size contacts*, Rev. Sci. Instrum. 67, 108 (1996).
- [17] S. R. Pollack and C. E. Morris, *Electron Tunneling through Asymmetric Films of Thermally Grown Al*₂O₃, J. Appl. Phys. **35**, 1503 (1964).
- [18] C. Chen, S. J. Splinter, T. Do, and N. S. McIntyre, *Measurement of oxide film growth on Mg and Al surfaces over extended periods using XPS*, Surf. Sci. **382**, L652 (1997).
- [19] C. P. Heij, P. Hadley, and J. E. Mooij, *Single-electron inverter*, Appl. Phys. Lett. **78**, 1140 (2001).
- [20] H. Klauk, U. Zschieschang, J. Pflaum, and M. Halik, *Ultralow-power organic comple-mentary circuits*, Nature **445**, 745 (2007).
- [21] K. Hansen, S. K. Nielsen, M. Brandbyge, E. Laegsgaard, I. Stensgaard, and F. Besenbacher, Current-voltage curves of gold quantum point contacts revisited, Appl. Phys. Lett. 77, 708 (2000).
- [22] A. Danilov, S. Kubatkin, S. Kafanov, P. Hedegård, N. Stuhr-Hansen, K. Moth-Poulsen, and T. Bjørnholm, Electronic Transport in Single Molecule Junctions: Control of the Molecule-Electrode Coupling through Intramolecular Tunneling Barriers, Nano Lett. 8, 1 (2008).
- [23] H. Park, J. Park, A. K. Lim, E. H. Anderson, P. A. Alivisatos, and P. L. McEuen, *Nanome-chanical oscillations in a single-C*₆₀ *transistor*, Nature **407**, 57 (2000).

- [24] M. L. Trouwborst, S. J. van der Molen, and B. J. van Wees, *The role of Joule heating in the formation of nanogaps by electromigration*, J. Appl. Phys. **99**, 114316 (2006).
- [25] E. A. Osorio, T. Bjørnholm, J.-M. Lehn, M. Ruben, and H. S. J. van der Zant, Single-molecule transport in three-terminal devices, J. Phys.: Condens. Matter 20, 374121 (2008).
- [26] E. A. Osorio, Ph.D. thesis, TU Delft (2009), URL http://resolver.tudelft.nl/ uuid:3050e349-460d-43db-97d8-b82dad811ef2.
- [27] A. E. Hanna and M. Tinkham, *Variation of the Coulomb staircase in a two-junction system by fractional electron charge*, Phys. Rev. B **44**, 5919 (1991).
- [28] Z. Y. Rong, A. Chang, L. F. Cohen, and E. Wolf, *STM control of non-integer charge on a metal particle inferred from Coulomb staircase*, Ultramicroscopy **42-44**, 333 (1992).
- [29] J. M. Thijssen and H. S. J. van der Zant, *Charge transport and single-electron effects in nanoscale systems*, phys. stat. sol. b **245**, 1455 (2008).
- [30] J. J. Parks, A. R. Champagne, G. R. Hutchison, S. Flores-Torres, H. D. Abruña, and D. C. Ralph, *Tuning the Kondo Effect with a Mechanically Controllable Break Junction*, Phys. Rev. Lett. **99**, 026601 (2007).

FABRICATION RECIPES

Preparation of wafers

- 1. Have phosphor bronze wafers (50 mm x 50 mm x 0.3 mm) polished by external company (van Geenen B.V., Rijssen)
- 2. Remove all visible contamination by wiping with acetone
- 3. Ultrasonicate wafers in acetone and isopropanol (IPA) for 5 min each
- 4. Prepare 0.1 vol-% solution of VM651 (HD Microsystems) in IPA (0.2 ml in 200 ml, use only polypropylene and Teflon (PTFE) equipment, shelf life is 24 h)
- 5. Bake clean wafer for 60 s @ 110°C on hot plate
- 6. Cover wafer with the VM651 solution through a 0.2 μ m PTFE filter (1 ml lasts for one 50 mm x 50 mm wafer) and soak for 30 s
- 7. Spin dry for 5 s @ 500 rpm, ramp 100 rpm/s, and 55 s @ 3000 rpm, ramp 200 rpm/s (use dry spinner with vacuum chuck, blow with N₂ if drops remain)
- 8. Bake for 60 s @ 110°C on hot plate (shelf life of primered substrates is 24 h)
- 9. Transfer small bottle (50 ml) of PI2610 (HD Microsystems) from freezer to RT, wait for temperature to equilibrate
- 10. Place wafer on vacuum chuck, blow with N₂
- 11. Apply PI2610 by dispensing it directly from the bottle over 1/2 of the substrate, spin coat for 10 s @ 500 rpm, ramp 100 rpm/s, and for 45 s @ 2000 rpm, ramp 100 rpm/s
- 12. Insert wafer on aluminum plate in Heraeus vacuum oven
- 13. Heat to 300°C @ 4°C/min, hold for 30 min, cool down
- 14. Place wafer on chuck, blow with N₂
- 15. Cover wafer with MMA(17.5)MAA copolymer resist solution (8% in ethyl-L-lactate, Microchem) through a 0.45 μ m PTFE filter and spin-coat (5 s at 500 rpm, 55 s at 2000 rpm)
- 16. Bake for 15 min @ 175°C on hot plate
- 17. Place wafer on chuck, blow with N₂

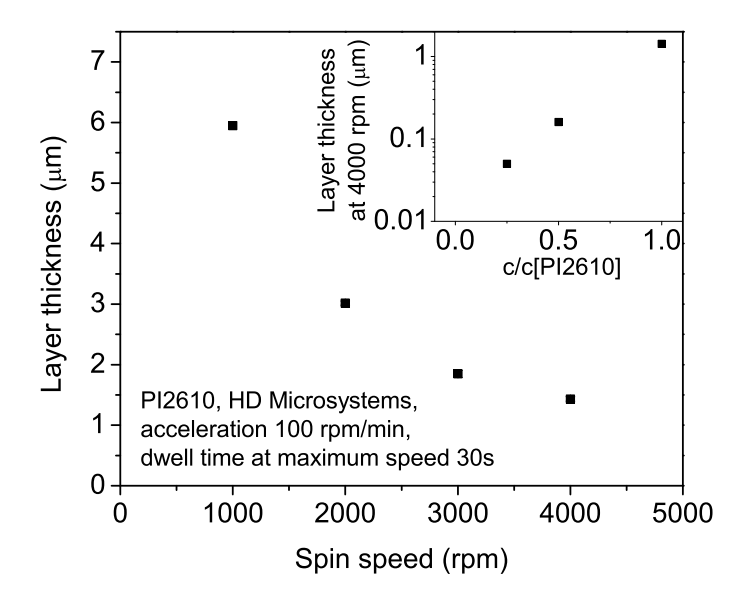


FIGURE 5: Spin curves of the polyimide precursor that was used in the preparation of the lithographic MCBJs (PI 2610, HD Microsystems). Layer thicknesses have been measured after following the standard bake-out procedure given in the recipes. The inset presents results for the precursor diluted in T 9039 (HD Microsystems).

- 18. Cover wafer with PMMA 950k resist solution (4% in anisole, Microchem) through a $0.45 \mu m$ PTFE filter and spin-coat (5s @ 500 rpm, 55 s @ 6000 rpm)
- 19. Bake for 15 min @ 175°C on hot plate

Two-terminal MCBIs

- 1. Write MCBJ structures (j2bw5-c with 73 nm @ 700 μ C/cm², j2bw5-f with 3 nm @ 900 μ C/cm²)
- 2. Develop for 90 s in MIBK:IPA (1:3) with slight movement, transfer wet to IPA and slightly move for 20 s to stop development
- 3. Evaporate 1 nm Cr @ 1.0 Å/s, 80 nm Au @ 1.0 Å/s
- 4. Immerse in hot acetone at 55°C for lift-off, transfer wet to IPA for rinsing
- 5. Protection layer: Cover wafer with PMMA 350k resist solution (7% in anisole) through a 0.45 μ m PTFE filter and spin-coat with program E (5 s @ 500 rpm, 55 s @ 2000 rpm)
- 6. Bake for 1 min @ 175°C on hot plate

Gated MCBJs with suspended S/D electrodes

- 1. Write markers (j3dw5-5) with 73 nm at 700 μ C/cm²
- 2. Develop pattern as above
- 3. Evaporate 5 nm Ti @ 1.0 Å/s, 130 nm Au @ 1.0 Å/s
- 4. Lift-off as above
- 5. Apply double layer of resist as above
- 6. Write common gate (j3csb-234) with 73 nm @ 700 μ C/cm²
- 7. Develop pattern as above
- 8. Evaporate 2 nm Cr @ 0.5 Å/s, 60 nm Au @ 1.0 Å/s
- 9. Immerse in hot acetone @ 55°C for first lift-off, transfer to fresh hot acetone @ 55°C for continued lift-off, transfer to hot IPA @ 55°C for rinsing
- 10. Bake on hot plate for 1 min @ 85°C
- 11. Spin coat with PI2610/T9039 dilution (HD Microsystems), ratio 1:3 v/v, for 10 s @ 500 rpm, ramp 100 rpm/s, and 70 s @ 4000 rpm, ramp 100 rpm/s
- 12. Bake film in vacuum oven for 30 min @ 250°C, ramp 4°C/min
- 13. Apply double layer of resist as above
- 14. Write source-drain electrodes and pads (j3csb-67 with 73 nm @ 650 μ C/cm² and j3csb-89 with 4 nm @ 880 μ C/cm²)
- 15. Develop pattern as above
- 16. Evaporate 1 nm Cr @ 0.5 Å/s, 80 nm Au @ 1.0 Å/s
- 17. Lift-off as above
- 18. Apply protection layer as above

Gated MCBIs with sandwiched electrodes

- 1. Write markers (j3dw5-5) with 73 nm @ 700 μ C/cm²
- 2. Develop pattern as above
- 3. Evaporate 2 nm Ti @ 1.0 Å/s, 130 nm Au @ 1.0 Å/s
- 4. Lift-off as above
- 5. Apply double layer of resist as above
- 6. Write connection pads to gate (j3dsb-2) with 73 nm @ 700 μ C/cm²

- 7. Develop pattern as above
- 8. Evaporate 3 nm Cr @ 0.5 Å/s, 37 nm Au @ 1.0 Å/s
- 9. Lift-off as above
- 10. Apply double layer of resist as above
- 11. Write gates (j2fsb-f) with 4 nm @ 900 μ C/cm²
- 12. Evaporate 1 nm Ti @ 1.0 Å/s, 60 nm Al @ 1.0 Å/s
- 13. Lift-off as above
- 14. RIE plasma etching, p=0.1 mbar, ${\rm O}_2$ @ 20 sccm, 150 W (Z-match 12.55/6.25), -630 V, 10 s
- 15. Apply double layer of resist as above
- 16. Write source-drain electrodes (j3fsb-9) with 4 nm @ 920 μ C/cm²
- 17. Develop pattern as above
- 18. RIE plasma descum at 0.003 mbar, O $_2$ @ 20 sccm, 50 W (Z-match 11.9/6.45), -180 V, $15~\mathrm{s}$
- 19. Evaporate 25 nm Au @ 1.0 Å/s
- 20. Lift-off as above
- 21. Apply double layer of resist as above
- 22. Write pads (j3fsb-678) with 69 nm @ 700 μ C/cm²
- 23. Develop pattern as above
- 24. Evaporate 2 nm Cr @ 0.5 Å/s, 170 nm Au @ 1.0 Å/s
- 25. Lift-off as above
- 26. Apply protection layer as above

SUMMARY

Charge Transport Through Single Molecules in Two- and Three-Terminal Mechanical Break Junctions

The ability to store, process, and transfer digital data constitutes one of the enabling technologies for the way we work and live today. On the scale of the microprocessors that handle these data, information is represented by small electrical signals and guided through millions of microfabricated electronic devices. Today's microprocessors are already based on transistors - voltage-controlled switches - that are only 30 nm long, less than a 1000th of the diameter of a human hair. Over the next years, these transistors are to shrink even further, and they may eventually approach the size of a few atoms. To understand and design such devices, fundamental studies of nanoscale charge transport are required; to fabricate them, new technologies will have to be developed.

The fabrication and characterization of electronic devices based on single molecules - *molecular electronics* - aims for reaching both of these goals. Single-molecule junctions offer fundamental insights into charge transport on the nanoscale, as well as the intriguing prospect of chemical tunability and bottom-up fabrication by self-assembly.

However, contacting a single molecule and controlling its electronic properties remains an experimental challenge. Transport in single-molecule junctions is dominated by quantum mechanics. Not only the chemical structure of a molecule, but also the anchoring to the electrodes influences its electrical characteristics. Two properties determine charge transport across molecular junctions: The positions of the molecular orbitals with respect to the energy of the conduction electrons in the leads (the *level alignment*), and the ease of transferring electrons from the electrodes to the molecule (the *electronic coupling*). To understand and tune transport in single-molecule junctions, we need to control both of these properties.

This Thesis describes the results of a PhD research project directed towards this degree of control. First, we study the influence of established chemical anchoring groups on the electronic properties of single-molecule junctions in vacuum. We then present a new end group that allows for the formation of stable molecular junctions with robust electronic coupling. In the second part of the Thesis, we establish and test two device architectures which offer simultaneous control over the electrode spacing and the level alignment in single-molecule junctions.

The experiments that are reported in this Thesis are based on lithographically fabricated mechanically controllable break junctions (MCBJs). In these devices, a gold wire is partially suspended on top of an insulating and flexible substrate. As the MCBJ substrate is bent, the suspended wire is stretched at the location of a roughly 80 nm-wide constriction.

132 Summary

During the bending of the substrate, the diameter of this constriction is reduced steadily until a single atom bridges the gap between the two ends of the wire. The electronic properties of this monatomic contact are well-defined and easily discernible in measurements of the junction conductance as a function of substrate bending. As soon as the last gold contact breaks, two atomically sharp electrodes are formed, which are of the right size to contact a single molecule. The power of the MCBJ architecture lies in the control over these electrodes. First, the rupture of the gold bridge leads to two clean tips for the formation of a single-molecule junction; subsequently, the tip distance can be tuned with subatomic precision by controlling the bending of the substrate on the scale of a micrometer.

The MCBJ devices and the experimental setups that were developed for this Thesis are presented in Chapter 3. Our experiments are carried out in vacuum inserts that allow us to control the bending of MCBJs with sub-micrometer precision. Using these inserts, the electronic properties of single-molecule junctions can be characterized at room temperature and at the temperatures of liquid nitrogen ($T=77~\rm K$) or liquid helium ($T=4.2~\rm K$). Before turning towards molecular transport, however, the mechanical properties of the setups and the MCBJ devices need to be characterized. We apply and present two different calibration methods to obtain an estimate of the mechanical attenuation of our MCBJs.

In the first part of this Thesis, we then address the goal of stable anchoring in single-molecule junctions. In Chapter 4, an experimental protocol for the trapping of single molecules in our MCBJs is established. In contrast to some earlier experiments which are based on the drying of a drop of molecular solution on the broken electrodes, we let the molecules self-assemble on the as-fabricated gold bridge. This reduces the danger of contamination from the solvent and prevents the crystallization of molecules in the junction area. After the self-assembly the bridge is broken in vacuum to form clean electrodes and trap a single molecule. The method guarantees a clean interface, but its success depends on the surface density and diffusion of molecules near the contact. If the gold electrodes are fused to far, the molecules can be pushed out of the junction area and the probability of trapping a molecule can decrease dramatically.

Using this protocol, the suitability of different chemical end groups for stable anchoring in vacuum is investigated (see Chapter 4). A number of previous studies in solutions of molecules have used amino (NH $_2$) and thiol (SH) groups to attach single molecules to gold electrodes. We study electrical transport through the conjugated molecules benzenedithiol and benzenediamine, and through the aliphatic model systems hexanedithiol and hexanediamine. While the measured conductances of hexanedithiol and hexanediamine are consistent with literature data, we do not observe a well-defined low-bias conductance in the case of the benzenes. We attribute this variability to the vacuum environment, which may allow for multiple adsorption geometries and reduce the lifetime of single-molecule junctions. The anchoring can be improved significantly by using a new C_{60} -based end group that was designed in the Bjørnholm group at the University of Copenhagen (see Chapter 5). The conductance of the C_{60} -anchored benzene is better defined than that of the corresponding dithiol, and its signature is stronger than that of benzenediamine.

Summary 133

The second part of this Thesis covers the integration of two-terminal MCBJs with a third electrode (a gate), the potential of which can shift the electronic levels on the molecule. Two types of electrically and mechanically tunable devices are presented and characterized in detail. Chapter 6 introduces a gated MCBJ architecture in which a gold bridge is suspended above a lithographically fabricated gold gate. After the bridge has been broken mechanically to form two electrodes (the *source* and the *drain*), the electrode gap is fully tunable by the bending of the substrate. However, the devices intrinsically act as nanoelectromechanical systems. Similar to a macroscopic relay, the application of a gate voltage causes the source-drain electrodes to bend towards the gate. This bending is usually associated with a reproducible change in the electrode distance, which may affect the geometry of single-molecule junctions. We develop a model to explain the effect and relate the conductance tuning in clean devices to the nanostructure of the electrode tips. The intrinsic electromechanical response in these gated MCBJs can be exploited to form a nanoscale switch. We demonstrate that the gate voltage can be used to switch the junctions reversibly between a monatomic contact with a conductance around $2e^2/h$ and the tunneling regime.

Low-temperature experiments on pure C_{60} confirm the electromechanical tuning in the gated MCBJs with suspended source-drain electrodes (see Chapter 7). Single-molecule junctions of C_{60} can display a zero-bias peak in the differential conductance that can be tuned by both the gate voltage and the substrate bending. The peak is reminiscent of the Kondo-effect and might be attributed to the presence of a single spin on the C_{60} , combined with an intermediate electronic coupling to the gold electrodes. The evolution of the peak with electrode distance can be modeled in the framework of Kondo physics and is in good agreement with previous measurements on junctions of C_{60} .

Chapter 8 concludes this Thesis with the presentation of modified gated MCBJ devices that do not show an electromechanical response. The direct deposition of the source-drain electrodes on the gate allows for an efficient tuning of the level alignment by the gate voltage, combined with mechanical control over the electrode gap. A nanoscale island in the Coulomb blockade regime serves as a first experimental test system, in which the mechanical and electrical tuning of charge transport is demonstrated. While we have not yet been able to use these gated MCBJs for the characterization of single molecules, the devices will enable thorough studies of molecular transport in the near future.

Christian Martin Delft and Leiden, November 2009

SAMENVATTING

Ladingstransport door enkele moleculen in mechanische breekjuncties met twee en drie elektrodes

Het opslaan, verwerken, en versturen van digitale data maakt deel uit van één van de meest centrale technologieën in onze samenleving: de informatietechnologie. Binnen de microprocessoren die deze data verwerken wordt informatie weergegeven door kleine elektrische signalen en verwerkt door miljoenen microgefabriceerde halfgeleiderelementen. De transistoren - spanningsgestuurde schakelaars - in commerciële microprocessoren zijn op dit moment 30 nm lang, minder dan een duizendste van de diameter van een haar. In de komende jaren zullen deze transistoren nog kleiner worden, en mogelijk gaan hun afmetingen uiteindelijk zelfs de schaal van enkele atomen bereiken. Om de eigenschappen van deze halfgeleiderelementen te begrijpen en te beheersen is fundamenteel onderzoek aan landingstransport op de nanoschaal vereist; om ze te fabriceren, is het nodig nieuwe technologieën te ontwikkelen.

Onderzoek aan elektronica-elementen die gebaseerd zijn op enkele moleculen - moleculaire elektronica - streeft allebei deze doelen na. Moleculaire juncties bieden inzicht in ladingstransport op de nanoschaal, en hun eigenschappen kunnen in principe door chemische synthese aangepast worden.

Echter het contacteren van een enkel molecuul en de controle over zijn geleiding zijn nog steeds experimentele uitdagingen. Transport door moleculaire juncties wordt bepaald door de kwantummechanica. Niet alleen de chemische structuur van een molecuul, maar ook het contact met de elektrodes heeft invloed op de elektrische eigenschappen. Twee aspecten kenmerken de geleiding door een moleculaire junctie: de positie van de energieniveaus op het molecuul ten opzichte van de Fermi-energie in de elektrodes (de *level alignment*), en de tunnelbarrières voor elektronentransport in en uit het molecuul (de *electronic coupling*). Wij kunnen transport in moleculaire juncties pas beheersen als wij beide eigenschappen goed begrijpen.

Dit proefschrift beschrijft twee belangrijke stappen in de richting van beter gedefiniëerde moleculaire juncties. In het eerste gedeelte bestuderen wij ladingstransport door enkele moleculen met verschillende chemische ankergroepen in een vacuümomgeving. Wij tonen aan hoe een nieuwe chemische eindgroep gebruikt kan worden om stabiele moleculaire juncties met een robuuste elektronische koppeling te vormen. In het tweede gedeelte van dit proefschrift presenteren en karakteriseren wij twee nieuwe *device*-types, waarin de elektrodenafstand en de *level alignment* in moleculaire juncties gelijktijdig ingesteld kunnen worden.

De experimenten in dit proefschrift zijn gebaseerd op lithografisch gefabriceerde mecha-

136 Samenvatting

nische breekjuncties (MCBJs). Deze *devices* bestaan uit een vrij hangend en elektrisch geïsoleerd gouddraadje op een flexibel substraat. Bij het doorbuigen van het MBCJ substraat wordt het draadje opgerekt; de oprekking is vooral geconcentreerd rond een inkeping met een breedte van 80 nm. Naarmate de doorbuiging toeneemt, slinkt de diameter van deze inkeping. Uiteindelijk zal een enkel atoom het contact vormen tussen de twee uiteinden van het draadje. De elektrische geleiding van een dergelijk éénatoom-contact is door de kwantummechanica vastgelegd en duidelijk te herkennen in metingen van de geleiding als functie van de doorbuiging. Als dit laatste contact breekt, worden twee scherpe en schone goudelektrodes gevormd, waartussen een enkel molecuul ingevangen kan worden. De intrinsieke mechanische vertraging van het MCBJ mechanisme maakt het mogelijk om de afstand van deze elektrodes met subatomaire precisie in te stellen door de doorbuiging van het substraat op de schaal van micrometers te variëren.

In hoofdstuk 3 worden de MCBJs en de experimentele opstellingen geïntroduceerd die voor dit proefschrift ontwikkeld zijn. Onze experimenten worden uitgevoerd in een vacuümkamer, waarin de doorbuiging van de MCBJs met submicrometer-precisie gecontroleerd kan worden. Deze vacuümkamer is gemonteerd aan een domplerstok waarmee het mogelijk is moleculaire juncties bij kamertemperatuur (300 K), maar ook bij de lagere temperaturen van vloeibaar stikstof (77 K) of helium (4.2 K) te bestuderen.

Het eerste gedeelte van dit proefschrift gaat over onderzoek naar een stabiele ankergroep voor moleculaire juncties. Voor we verschillende groepen bestuderen, ontwikkelen en introduceren we eerst een experimenteel protocol voor het invangen van een enkel moleculaire onze MCBJs (zie hoofdstuk 4). Anders dan in eerdere experimenten, waar men een druppeltje moleculaire oplossing op de gebroken elektrodes liet opdrogen, is onze methode gebaseerd op zelfassemblage van de moleculen op de onbeschadigde brug. Dit vermindert het risico dat de junctie door ongewenste bestanddelen van het oplosmiddel vervuild wordt, en het voorkomt de kristallisatie van moleculen. Na de zelfassemblage wordt de brug onder vacuüm gebroken, dit om schone elektrodes te vormen en hiermee een enkel molecuul te vangen. Deze aanpak garandeert een schoon contact, maar is erg afhankelijk van de oppervlakteconcentratie van moleculen rond het contact. Als de elektrodes te ver in elkaar geduwd worden, kunnen moleculen uit het contact geperst worden en de waarschijnlijkheid een enkel molecuul te vangen neemt dan drastisch af.

Dit depositieprotocol wordt vervolgens gebruikt voor het testen van verschillende chemische ankergroepen in vacuüm. Enkele eerdere experimenten aan moleculaire geleiding in oplossingen hebben gebruik gemaakt van amino en thiol groepen om moleculen aan goudelektrodes te hechten. Wij bestuderen ladingstransport door de geconjugeerde moleculen benzeendithiol en benzeendiamine, en door de alifatische modelsystemen hexaandithiol en hexaandiamine. Terwijl de hexanen een geleiding vertonen die consistent is met data uit de literatuur, laten de benzeenmoleculen geen goed gedefiniëerde lage-spanningsgeleiding zien. Wij schrijven dit toe aan de vacuümomgeving, waarin een veeltal van adsorptie-geometrieen denkbaar is en waarin de levensduur van moleculaire juncties mogelijk verkort is. De stabiliteit van onze moleculaire juncties kan duidelijk verbeterd worden door een nieuwe C_{60} -gebaseerde ankergroep te gebruiken, die de Bjørnholm groep aan de Universiteit Kopenhagen ontwikkeld heeft (zie hoofdstuk 5). Wanneer benzeen via C_{60} aan goud elektrodes gebonden wordt, vertoont de geleiding minder spreiding dan in

Samenvatting 137

het geval van benzeendithiol, en is zijn signatuur in statistische metingen duidelijker dan die van benzeendiamine.

Het tweede gedeelte van dit proefschrift gaat over de integratie van tweepunts-MCBJs met een derde elektrode (een gate), waarmee de elektronenniveaus op het molecuul verschoven kunnen worden. Wij presenteren en karakteriseren twee verschillende architecturen, waarin zowel mechanische als elektrische beïnvloeding van moleculaire juncties mogelijk is. Hoofdstuk 6 introduceert een gated MCBJ, waarin een goud brug vrij boven een nanogefabriceerde gate hangt. Na het mechanische breken van de brug, waarbij twee elektrodes (de source en de drain) gevormd worden, kan men de elektrodenafstand volledig instellen door het substraat te buigen. Deze MCBJs functioneren als nanoelektromechanische systemen. In analogie met een macroscopisch relais veroorzaakt een gate-spanning een beweging van de source-drain elektrodes in de richting van de gate. Deze beweging, ofwel doorbuiging, leidt tot een verandering in de elektrodenafstand, hetgeen de geometrie van moleculaire juncties beinvloedt. Wij ontwikkelen een model om dit effect te verklaren en laten zien hoe de verandering in de tunnelstroom in schone juncties afhangt van de nanogeometrie van de elektrodes. De intrinsieke elektromechanische werking in deze gated MCBJs kan gebruikt worden om een schakelaar op de nanoschaal te vormen. Wij laten zien dat de gate in staat is om de juncties omkeerbaar tussen een éénatoom-contact met een geleiding rond de $2e^2/h$ en een tunnelcontact te laten schakelen.

Lage-temperatuur metingen aan puur C_{60} bevestigen de elektromechanische eigenschappen van de *gated* MCBJs met vrijhangende *source-drain* elektrodes (zie hoofdstuk 7). Moleculaire juncties van C_{60} kunnen bij een spanning van 0 V een piek in de differentiële geleiding vertonen, die door de *gate*-spanning ofwel de doorbuiging van het substraat beïnvloed kan worden. Die piek lijkt te wijzen op een Kondo resonantie, die veroorzaakt zou kunnen worden door een enkele *spin* op de C_{60} en een matig sterke elektronische koppeling aan de goud elektrodes. De afhankelijkheid van de piek met de elektrodenafstand kan binnen het kader van het Kondo effect gemodelleerd worden en stemt overeen met eerdere metingen aan C_{60} juncties.

In hoofdstuk 8 ronden wij dit proefschrift af met *gated* MCBJs waarin geen elektromechanische effecten optreden. Door de *source-drain* elektrodes direct op het *gate* te fabriceren, kunnen wij een efficiënte controle over de elektronenniveaus van het molecuul combineren met een mechanische controle over de elektrodenafstand. Wij laten zien hoe ladingstransport in een nanometergroot eiland Coulomb blokkade vertoont, en dat dit effect mechanisch en elektrisch beïnvloed kan worden. Hoewel wij in deze *gated* MCBJs nog geen moleculaire juncties gekarakteriseerd hebben, zetten wij hiermee een belangrijke stap in de richting van nader fundamenteel onderzoek aan moleculaire geleiding.

Christian Martin Delft en Leiden, november 2009

CURRICULUM VITAE

Christian Alexander MARTIN

03/08/1978	Born in Hamburg, Germany.
1989-1998	Grammar school, Wolfgang-Borchert-Gymnasium, Halstenbek, Germany.
1999-2003	BSc in General Engineering Science, Hamburg University of Technology, Hamburg, Germany.
2002-2003	BSc research project at the University of Cambridge, Cambridge, United Kingdom, under supervision of prof. dr. Alan Windle.
2003-2005	DiplIng. (with distinction) in Electrical Engineering, Hamburg University of Technology, Hamburg, Germany.
2004-2005	Graduation research project at Philips Research, Eindhoven, The Netherlands, under supervision of prof. dr. Dago de Leeuw.
2005-2009	PhD research at Delft University of Technology and Leiden University under supervision of prof. dr. ir. H. S. J. van der Zant and prof. dr. J. M. van Ruitenbeek.

LIST OF PUBLICATIONS

- A nano-electromechanical single-atom switch
 C. A. Martin, R. H. M. Smit, H. S. J. van der Zant, J. M. van Ruitenbeek, Nano Lett. 9, 2940 (2009).
- Fullerene-based anchoring groups for molecular electronics
 C. A. Martin, D. Ding, J. K. Sørensen, T. Bjørnholm, J. M. van Ruitenbeek, H. S. J. van der Zant, J. Am. Chem. Soc. 130, 13198 (2008).
- Lithographic mechanical break junctions for single-molecule measurements in vacuum: possibilities and limitations
 C. A. Martin, D. Ding, H. S. J. van der Zant, J. M. van Ruitenbeek, New J. Phys. 10, 065008 (2008).
- Large area liquid crystal monodomain field-effect transistors
 A. J. J. M. van Breemen, P. T. Herwig, C. H. T. Chlon, J. Sweelssen, H. F. M. Schoo, S. Setayesh, W. M. Hardeman, C. A. Martin, D. M. de Leeuw, J. J. P. Valeton, C. W. M. Bastiaansen, D. J. Broer, A. R. Popa-Merticaru, S. C. J. Meskers, J. Am. Chem. Soc. 128, 2336 (2006).
- 3. Electric field-induced aligned multi-wall carbon nanotube networks in epoxy composites C. A. Martin, J. K. W. Sandler, A. Windle, M.-K. Schwarz, W. Bauhofer, K. Schulte, M. S. P. Shaffer, Polymer **46**, 877 (2005).
- Formation of percolating networks in multi-wall carbon-nanotube-epoxy composites
 C. A. Martin, J. K. W. Sandler, M. S. P. Shaffer, M.-K. Schwarz, W. Bauhofer, K. Schulte, A. Windle, Comp. Sci. Tech. 64, 2309 (2004).
- Percolation in Multi-Wall Carbon-Nanotube-Epoxy composites
 J. K. W. Sandler, A. H. Windle, C. A. Martin, M.-K. Schwarz, W. Bauhofer, K. Schulte, M. S. P. Shaffer, MRS Symp. Proc. 788 (2004).

ACKNOWLEDGEMENTS

Completing a PhD is a strenuous enterprise, and doing so in two research groups with two different cultures and two different hosting universities is a logistical tour de force. And yet, somehow this PhD Thesis emerged as a true product of two worlds, the Atomic and Molecular Conductors group at Leiden University and the Molecular Electronics and Devices group at Delft University of Technology. The four years that it took to complete it have been tough, exciting, and tiring at times. Yet, they have always been enriching: working on a PhD with two advisors who also served as institute directors has been an exceptional experience. Herre, your ability to motivate and manage independent research is impressive. You not only preach working in parallel, you also practice it. Jan, your broad overview of physics and your advocacy of open communication set an example. Even in conflictual times, you uphold your values - I admire this.

I am happy to have met many other researchers who share this openness, and I would like to point out some of them. Their advice has contributed a great deal to the completion of this Thesis. First, I would like to thank Dago de Leeuw for scientific and, whenever necessary, moral support. Your quote 'It takes as long as it takes' has been one of the most comforting notions of the first year of my PhD. Latha Venkataraman has been a similarly inspiring person. Sharing and discussing your experimental results on molecules in solution has greatly enhanced my overview of molecular electronics. Ferdinand Evers with his talent for explaining the principles of non-equilibrium charge transport to experimentalists has always helped me to put our measurements in perspective. It is great to have all of you on my defense committee. I am also glad that Teun Klapwijk, Ernst Sudhölter, and Gerrit Bauer could take the time to read through this Thesis and be part of my defense.

There are a number of other people who were of great help at various points of this project. At the beginning of this project, Cristián Urbina and Daniel Estève from Saclay and Ralf-Rainer Rohloff from Heidelberg gave us good advice on the design of the mechanical break junction devices and the cryogenic measurement setups. Once there was a plan, the measurement equipment was built with some material support from Giorgio Frossati and Leiden Cryogenics. Ruud van Egmond, who contributed significantly to the design of the vacuum inserts and who also built them, Raymond Schouten with his back-of-the-envelope designs of analog electronics, and Bert Crama with his actuator driver units have all been significant for the MCBJ setups. At various instances, Christiaan Pen, Fred Kraneburg, Jaap Beekman, Piet Mulder, and Ruud van Ooijik have also provided valuable technical support.

Once there was the first setup, we also needed MCBJ devices. The process development in the Delft Nanofacility would not have been possible without the clean room staff. Roel Mattern and Patrick Lew, Arnold van Run and Anja van Langen, Marco van der Krogt and Marc Zuiddam provided excellent advice and support on all instances of nanofabrication.

144 ACKNOWLEDGEMENTS

Special thanks go to Emile van der Drift for buying extra equipment for the MCBJs.

Once the experiments on bare gold junctions had shown conductance quantization, Paul van Hal and Sepas Setayesh shared valuable knowledge on the self-assembly of thiols. Masamichi Fujihira and Shintaro Fujii also provided useful advice, and a few milligrams of benzendithiol to start with. The first molecular model systems could be tested. Soon, there were new and more exciting molecules ahead. Jakob Kryger Sørensen and Thomas Bjørnholm designed and synthesized the fullerene-anchored molecules presented in this Thesis, which were characterized optically and electrochemically by Jeppe Fock.

During the development of the fabrication process for gated mechanical break junctions, advice by Paul Smith and Natalie Stutzmann on the spin coating of thin polymer films was of great help. The behavior of these devices was first puzzling, but discussions with the gMCBJ pioneers Alex Champagne and Dan Ralph quickly improved our understanding. After applying molecules to these devices, we got more good advice from Cornell. Josh Parks was very supportive when it came to judging low-temperature data on C_{60} , as was Elke Scheer from Konstanz. Besides, informal discussions with the break junction team in Groningen (Marius Trouwborst, Eek Huisman, and Sense Jan van der Molen) have been extremely useful on various occasions. I am very happy that two of you have eventually joined the group in Leiden.

Other group members have actively been involved in the work that is described in this Thesis. First, I would like to point out Dapeng Ding, who worked on the fullerene-anchored molecules. Your enthusiasm for science, your quick grasp of new concepts, and your working attitude have been inspiring, and I am still impressed by your MSc thesis. Edgar Osorio, one of the MED pioneers, helped me on the way with the measurement equipment and the clean room in Delft. Thanks for all our discussions and for keeping me motivated at the beginning of this project. Besides, Ferry Prins turned out to be a chemistry-wiki for the Delft group - thanks for all advice, Ferry! Towards the end of this project, Roel Smit joined me for some measurements and the design of the second-generation MCBJ insert. Our collaboration has probably resulted in the fastest lithographic-MCBJ measurement setup to date and makes me quite proud. I hope Jeppe Fock, Diana Dulic, Mickael Perrin, and we will still carry out a lot of exciting experiments. I also enjoyed working with Constant Guédon during a short internship in Delft. I am glad you got fascinated enough to join the Leiden group for a PhD in molecular electronics and I am looking forward to having you as a 'paranimf'.

Of course, there have been many more nice interactions. Among the many in Leiden, I remember Robert Thijssen and our short project on ferromagnetic MCBJs, Youri de Boer and the liquid-cell MCBJs, eliminating ground loops with Michael Krieger, long discussion breaks with Reyes Calvo and Ancuta Mares, occasional processing talk with Alex Yanson, a spring school in Anacapri with Oren Tal, admistrative help from Daniëlle Duijn and Barry Cats, Marcel Hesselberth's mastery of the 7th-floor equipment, and nice discussions with Darko Djukic, Sander Otte, Bas Leerink, Manohar Kumar, Monica Morales, and Sebastian Schramm. In Delft, I had the pleasure to share an office with Alexander Zyazin and Samir Etaki. While Samir was more with his SQUIDs than in the office, Alex was almost always around and thinking about spins. Both of you have already achieved amazing results, and I wish you all the best for the rest of your PhDs. I also happily remember some parylene de-

position experiments with Anna Molinari, conference visits with Anne Bernand-Mantel, Edgar Osorio, and Menno Poot, enlightening theory tutorials by Jos Thijssen and Chris Verzijl, elaborate DFT calculations and a great Thesis template from Jos Seldenthuis, chats with the organic electronics team (Hanxing Xie, Helena Alves, and Iulian Hulea), NEMS simulation help from Warner Venstra, Gijs Babaei Gavan and Menno Poot, tidying up with Benoit Witkamp;), late shifts with fellow German Andreas Hüttel and Bo Gao, good advice from Kevin O'Neill on the logarithmic amplifier, regular visits from Rami Barends and Gabri Lansbergen, transport rides with Mascha van Oossanen, administrative support from Monique Vernhout, Maria Roodenburg, and Irma Peterse, and clean room chats with the QT crew Katja, Pol, Georg, Lan, and Floor. All those that have not been mentioned here have not been forgot, to be sure. Having all of you around has made the last four years more enjoyable.

However, the PhD still was a tour de force. I might not have completed this tour without the necessary motivation and support from outside the track. It is my friends that deserve much of the credit. Eit, Joost, Barbara, Sasja, Alistair, Anna, Edsger, Bianca, Simon, Monica, Ivan, Susu, Catharina, Tim, Julia, Mathias, and Helen: thanks for the good times in The Hague, Leiden, Eindhoven, London, Nottingham, Hamburg, and Zurich! Außerdem danke ich meinen Eltern, die nach jahrelangem Warten hoffentlich bald mit Stolz auf das Ende meiner 'Ausbildung' zurückschauen können. Das letzte Wort jedoch gebührt Kathrin: dafür, dass sie geduldig war, wann immer möglich, ungeduldig, wann immer nötig, und da. Einfach immer.

Christian Martin Delft and Leiden, November 2009